Impulse Control of Harmonic Drive Motors for High Precision Positioning Applications

Yu Kun Yang

A Thesis

in

The Department

of

Mechanical and Industrial Engineering

Presented in Partial Fulfillment of the Requirements

For the Degree of Master of Applied Science at

Concordia University

Montreal, Quebec, Canada

March 2004

Your file Votre référence
ISBN: 0-612-91146-2
Our file Notre référence
ISBN: 0-612-91146-2

ABSTRACT

Impulse Control of Harmonic Drive Motors for High Precision Positioning Applications

Yu Kun Yang

Harmonic drive motors are widely used in precision control systems due to several advantages such as zero backlash, high gear ratio, compact size and light weight. However, the combination of friction and flexibility in harmonic drives often limits the performance in positioning applications when using conventional control methods. One problem that often occurs is that the system sticks before the desired position is reached. An alternative and effective solution is to apply a large impulse input for a very short period of time to achieve small motion increments.

In this thesis, a new control approach using impulse inputs is developed to improve the resolution of harmonic drive motors. The main objective is to achieve maximum resolution in the presence of high friction levels. A model capable of predicting the impulse response of harmonic drive motors is developed and used to guide the development of an optimal impulse waveform that is robust to parameter variations. The optimal input is then used in the development of an adaptive impulse control method. The performance of the approach is verified with extensive simulations and experiments. Use of the impulse control method demonstrates that the resolution of harmonic drive motors can be increased by more than an order of magnitude. Together, these results provide an effective new approach for control of harmonic drive motors in high precision positioning applications.

ACKNOWLEGEMENTS

This thesis was carried out in the Control and Information System Laboratory (CIS) at Concordia University, Montreal, Canada. It was an excellent opportunity for me to experience my field in a variety of special areas. I am grateful to all those who have contributed to this thesis.

First, I would like to express great thanks to my supervisor, Dr. Brandon W. Gordon, for his effective support and guidance throughout the work of this thesis. His knowledge deeply impressed me. His broad knowledge of control and mechanical systems also encourages me to study more in an effort to reach the level of knowledge that he has.

I am also very grateful to my classmates, Baktash, John Lu, and Joy Zhou for their help in my experimental establishment, and for their advice in the programming and experimentation parts of this thesis.

Finally, I would also like to thank Bai Yun, Gangjun Li, and Zili Li, for their encouragement, support and help both in searching for material, and in writing the thesis itself.

Yu Kun Yang

Montreal, Canada

Table of Contents

List of Figures

List of Tables

List of Symbols and Variables

a : parabolic curve coefficient defined in equation (5-27)

$a_0 - -a_{10}$: Fourier series coefficients

b : parabolic curve coefficient in equation (4-23)

$b_1 - -b_{10}$: Fourier series coefficients

b_l : load side viscous coefficient

b_m : motor side viscous coefficient

B: constant in equation (2-15)

C_0, C_1 : integral constant

CS: tooth number of circular spline

d: arm displacement (delta)

E_k : kinetic energy

E_p : potential energy

F : adaptive control constant

f_l : load side Coulomb or static friction

f_m : motor side Coulomb or static friction

f_{cl} : load side Coulomb friction

f_{sl} : load side static friction

f_{cm} : motor side Coulomb friction

f_{sm} : motor side static friction

f_{aver} : average Coulomb friction

f_{coul} : simulated Coulomb friction

f_{peri} : simulated periodical friction

f_{visc} : viscous friction

f_l^* : non-dimensional friction level

F_l : load side friction

F_m : motor side friction

FS: teeth number of flexspline

$g_1 - - g_7$: online adapted parameters

h : square pulse amplitude

h_1 : first harmonic pulse amplitude

h_2 : second harmonic pulse amplitude

h_3 : third harmonic pulse amplitude

h_4 : fourth harmonic pulse amplitude

i_a : motor armature current

J_l : load side inertia

J_m : motor side inertia

J_l^* : non-dimensional load side inertia

K : adaptive control constant

K_b : motor voltage constant

K_c : adaptive control constant

K_m : motor torque constant

K_s : harmonic drive spring constant

K^* : non-dimensional spring constant

L : armature inductance

m : momentum of the pulse

p : motor torque amplitude

q_{ex} : experimental data of motor or load position

q_l : load side (arm) position

q_m : motor position

q_{mw} : motor position at t=W

q_{simu} : simulation data of motor or load position

r : harmonic drive gear ratio

r^* : non-dimensional gear ratio

R: armature resistance

$s_1 - - s_3$: second order polynomial coefficients in equation (2-12)

t : time

t^* : non-dimensional time

T_c : system characteristic time

T_m : motor torque

T_s : harmonic drive spring torque

u: motor input voltage

V: voltage

Vc: velocity of Coulomb friction

V_{ls} : cost function of optimal parameter tuning

Vs: voltage required to overcome static friction

V_{mw} : motor velocity at t=W

W: pulse width

x : discrete arm position in impulse control

x_d : desired arm position in impulse control

$x_1 - - x_4$: state variables

ω_c : system characteristic frequency

ω_l : load side angular velocity

ω_m : motor side angular velocity

ε : adaptive control variable

ε_1 : resolution defined constant

ε_2 : resolution defined constant

ψ_l : torque acted on load inertia when load inertia velocity is zero

ψ_m : torque acted on motor inertia when motor velocity is zero

$\Delta\theta$: presliding displacement

τ^* : non-dimensional motor torque

σ : standard deviation

η_s : The distance from point where the simulation line is across x-axis to origin.

η_e : The distance from point where the experimental line is across x-axis to origin.

Chapter 1 Introduction

1.1 Motivation

Precise position control using harmonic drive motors is very important for many industrial applications. For example, in the optoelectronic automation industry, the process of attaching optical fibres to optoelectronic devices (pigtailing) requires submicron alignment accuracy in positioning. A robotic manipulator was previously developed to automate such precise optical alignments [1]. The key parts of this manipulator are two arms driven by harmonic drive motors and one linear stage actuated by a timing belt driven lead screw. Figure 1-1 illustrates the manipulator.

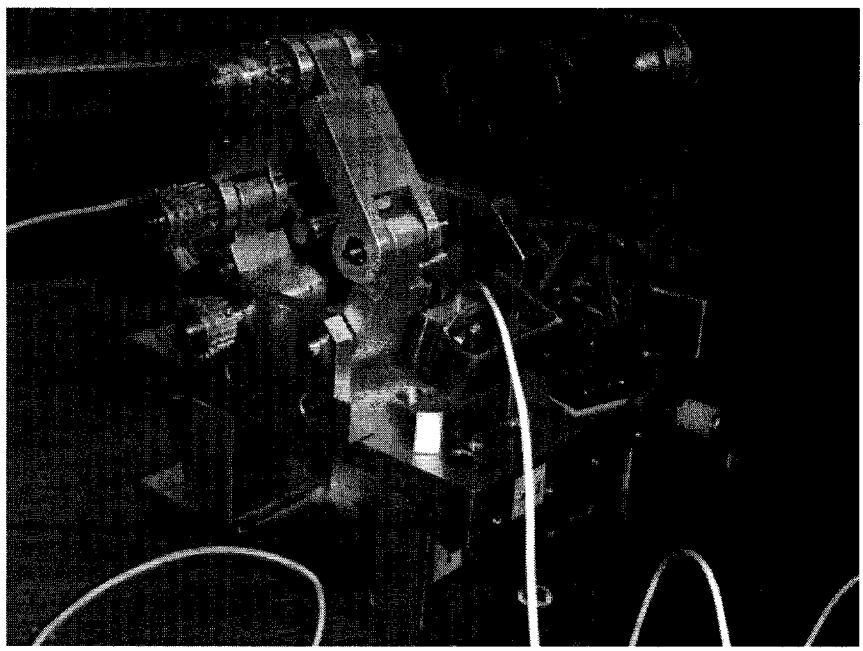

Figure 1-1 The robotic manipulator

1.2 Research objectives

The main objective of this thesis is to develop a new control approach using impulse inputs to improve the positioning precision of harmonic drive motors. A model capable of predicting the impulse response of harmonic drive motors is developed and used to guide the development of an optimal impulse waveform that is robust to parameter variations. The optimal input is then used in the development of an adaptive impulse control method. The performance of the approach is verified with extensive simulations and experiments on the manipulator introduced in the previous section.

1.3 Literature review

This thesis mainly deals with following areas: friction measurement and modelling, harmonic drive, and impulse control. In the following literature overview, the above three areas are presented respectively.

1.3.1 Friction modelling

Friction force is proportional to load, opposes the motion, and is independent of the contact area—this was all known to Leonardo Da Vinci in 1519. Da Vinci's friction model was rediscovered by Amontons (1699) and developed by Coulomb (1785), among others in the field. Amontons' claim that friction is independent of the contact area (the second of Da Vinci's laws) originally attracted scepticism, but was soon verified. Morin (1833) introduced the idea of static friction and Reynolds (1866) introduced the

equation of viscous fluid flow, completing the friction model that is most commonly used in engineering: the static + Coulomb + viscous friction model.

The science of tribology, Greek for the study of rubbing, was pioneered in England in the 1930s. Basic questions of wear mechanisms, true contact area, relationships between friction, material properties, and lubricating processes were addressed and answered. Dowson (1979) wrote an engaging work that illuminates the 3000 year history of humankind's attempts to understand and modify friction. Hamrock's work (1986) is a brief handbook survey of the relevant methods of tribology and Halling (1975) provides a survey that is rigorous, not overly detailed but sufficiently sweeping to address such issues as friction induced instability and solid lubrication. Ludema's work (1988) is an interesting critique of tribology and the cultural barriers of interdisciplinary pursuits, and Rabinowicz (1978) presents a discussion of the priorities of tribology.

So far, about thirty friction models have been presented. Dahl (1968) concluded that for small motions, a junction in static friction behaves like a spring; he then considered the implications for control. There is a displacement (presliding displacement) that is an approximately linear function of the applied force, up to a critical force, at which breakaway occurs. In 1985, Karnopp proposed an improved friction model. In 1991, D.A. Haessig et al. presented two new models [19]. One is the "bristle model" which is an approximation designed to capture the physical phenomenon of sticking. However, numerically, it is relatively inefficient. The second model is called the "reset integrator model" and it is numerically efficient and exhibits behaviour similar to Karnopp's model, but it does not capture the details of the sticking phenomenon. All above four models poorly represent friction force at zero velocity.

A dynamic friction model was proposed by C. Canudas de Wit et al. in 1995 [21]. The model, called the LuGre model, captures most of the friction behaviour that has been observed experimentally. This includes the Stribeck effect, hysteresis, spring–like characteristics for stiction, and varying breakaway force. This model was compared with a standard simple kinetic friction model (KFM) by Friedhelm Altpeter et *al.* through a singular perturbation analysis [23]. They concluded that in a unidirectional motion and Fs=Fc, KFM is sufficient to model friction. However, if Fs ≠Fc, the LuGre model captures more dynamic properties. The LuGre model was also tested experimentally by Rafael Kelly[24] . C. Canudas de Wit's experimental results validated the LuGre friction model in an adaptive control scheme with friction compensation [27]. In his Ph.D. thesis, Prasanna S. Gandhi uses the LuGre model to identify the friction in harmonic drives [2][10].

The shortcomings of the LuGre model lie in [22] its inability to account for nonlocal memory and in that it cannot accommodate arbitrary displacement-force transition curves. Jan Swevers et al. [22] proposed a new dynamic friction model that overcomes the shortcomings mentioned above. This model allows accurate modelling both in the sliding and the presliding regimes. However, no literature was found to use this model in real applications.

In recent years, many other friction models have been proposed. Fitsum A. Tariku et al. [25] proposed two dynamic models for simulation of one-dimensional and two-dimensional stick-slip motion. Ruh-Hua Wu et al. [26] presented a modified Coulomb friction model integrating presliding displacement in the microsliding regime. Milos R. Popovic et al. [30] noticed that most friction models available describe friction

only as a function of velocity. This is not always true. In many cases, friction is dependent on position; for example, with harmonic drives. Milos proposed a new spectral-based modelling technique that ably describes nonlinear friction as a function of position and velocity.

1.3.2 Harmonic drive

Harmonic drive has captured more and more researchers' attention in the last decades. Because it has many advantages including near-zero backlash, high gear reduction ratio and compact design, it is more and more widely used in precision control systems. On the other hand, the nonlinear attributes are responsible for performance degradation. Therefore, accurate modelling of these nonlinear attributes is critical for the use of harmonic drives. Hamid D. Taghirad et al. [3] developed an overall friction model for harmonic drives and Timothy D. Tuttle et al. (1996) developed a nonlinear harmonic drive model [13]. This latter model captures most nonlinear behaviours, such as kinematic error, friction, and flexibility. Hamid D. Taghirad also modelled the harmonic drive including friction and compliance in his Ph.D. thesis [3][8]. However, the above two models do not consider the position dependent friction. Prasanna S. Gandhi (2001) proposed an overall model for harmonic drives [2]. He modelled all main nonlinear attributes in the harmonic drive such as kinematic error, hysteresis, and friction. He first observed the position dependent friction in harmonic drives, and used the Fourier series to model the position dependent friction. He also came up with a new hysteresis model for harmonic drives. In his friction model, he only considered one revolution friction on motor side, and did not observe that the friction in harmonic drives is also dependent on

load side position.

Han Su Jeon [36] studied the vibration in harmonic drives from a material point of view. He studied the different materials and found that they will result in different natural frequencies in harmonic drives. This is the first literature on the vibration of harmonic drive that so far has been found.

1.3.3 Impulse control

Several researchers have developed impulse controllers to position mechanical systems precisely. Hojjat and Higuchi [20] presented an apparatus designed especially to demonstrate impulse control; Sangsik Yang and M. Tomizuka [32] developed an adaptive impulse controller in 1988; M.R.Popovic, D.M.Gorinevsky and A.A.Goldenberg [18] tested the displacement for different pulse amplitudes and different durations, and designed an impulse controller based on the experimental results; Armstrong and Armstrong-Helouvry [20] demonstrated an impulse controller on a industrial PUMA robot; and Brandon W. Gordon [1] used impulse to position a fibre alignment manipulator in his master's thesis [1]. All of the above impulse controllers satisfy control precision. Their detailed work will be presented in section 4.1.

Input shaping is a new method to study flexible structure vibration. Some recent papers investigate the effect of how time-varying impulses shape sequence on the flexible structure [38][39].

1.4 Thesis outline and contribution

A new approach for high precision control of harmonic drive motors using impulse control inputs is presented in this thesis. Chapter 2 develops a dynamic model including the effects of friction and transmission flexibility. In Chapter 3 identifies the model experimentally. This model is shown to be capable of accurately predicting the impulse response of harmonic drive motors and demonstrates a usefulness for the development of impulse control systems in Chapter 4. Chapter 5 investigates the effect of parameter variations on impulse response. The determination of an optimal impulse waveform and pulse rate is also performed. Finally, an adaptive impulse feedback controller is developed to account for variations in load friction. A large amount of experimental testing is performed to verify the approach. The conclusions are stated in Chapter 6.

The results of this thesis represent the first known comprehensive study of applying impulse control to harmonic drive motors for high resolution positioning applications. This approach demonstrates that resolution can be increased by more than an order of magnitude over conventional control methods. This will allow harmonic drives to be economically used in many new applications where high precision positioning capability is needed.

Chapter 2 Modelling

In order to guide the development of an impulse controller specifically for harmonic drive motors, a good model for the system is required. This model should include the main attributes of the system. This chapter will present a mathematical model for the system.

2.1 Experimental apparatus

2.1.1 Overall scheme

In order to control the manipulator with a computer, an amplifier and an interface card are required. The interface card includes A/D, D/A and an encoder accessing device. Two capacitance sensors are mounted parallel to the arms of the manipulator and are used to measure the position of the arms.

The overall control scheme is illustrated in Figure 2-1

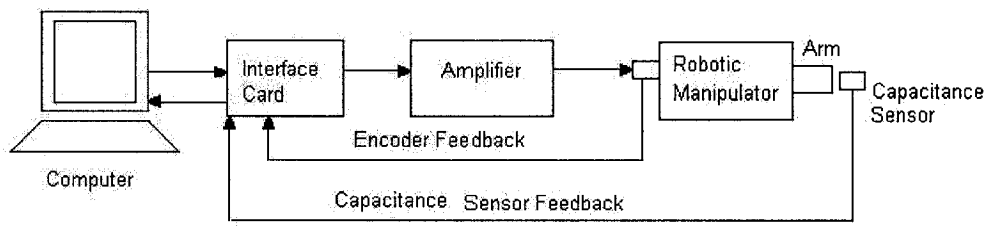

Figure 2-1 Overall control scheme

In the process of experimentation, some other apparatus are required. These apparatus are: multi-meter, oscilloscope, and DC power supply. The experimental apparatus are shown in Figure 2-2.

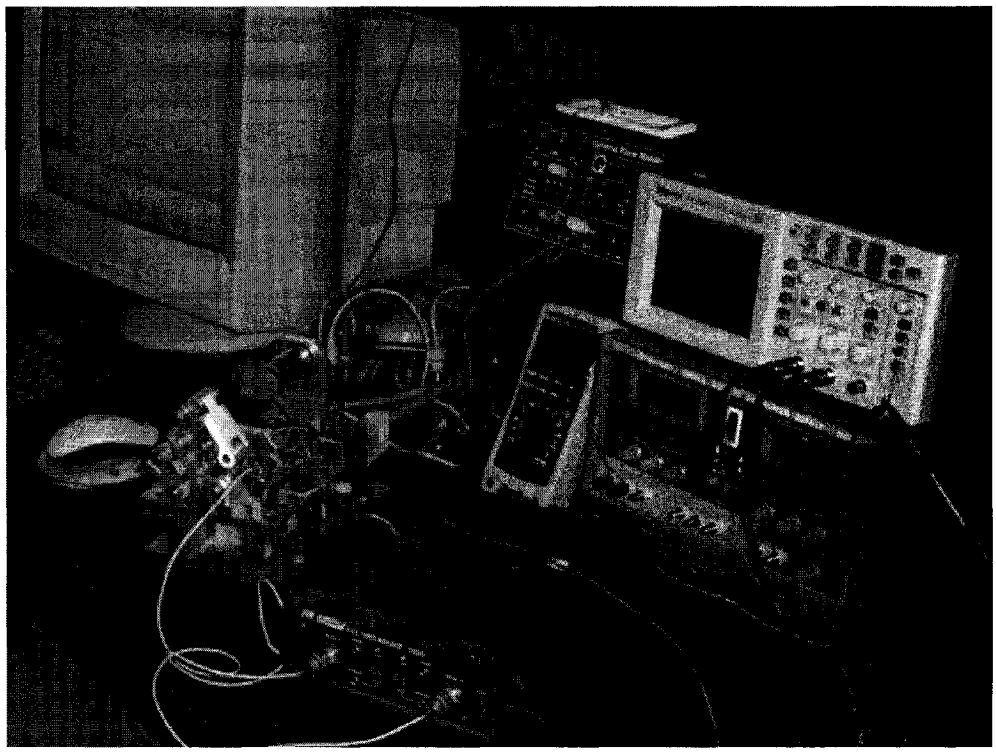

Figure 2-2 Experiment setup

2.1.2 Robotic manipulator

The manipulator shown in Figure 1-1 was built at MIT. It has three degrees of freedom: X, Y, Z direction respectively. The X and Y directions are driven by two harmonic drive motors. The harmonic drive motors are from HD systems INC., model number Hi-TDrive RH-5A-5502. The harmonic drive's gear ratio is 1:80. On both sides of the manipulator arms, two capacitance sensors are installed to measure the arm positions. Four sensors are fixed beside the arms. These sensors can be used to find

the same start point for the experiments.

The manipulator is carried by a linear stage (Z-direction) actuated by a DC motor through a lead screw. The model of the DC motor is the Pittman 8424. The 40 thread per inch lead screw is driven by a 5:1 timing belt connected to a DC motor.

The RH-5A-5502 harmonic drive motor consists of a DC motor and a harmonic drive transmission. The output of the harmonic drive is connected to the arm of the manipulator.

2.1.3 Interface card

The MultiQ-PCI interface card is from Quanser Consulting, Inc. It consists of a PCI card and an outside connection board. There are 6 encoder input ports, 16 A/D input ports, 4 D/A output ports and 6 banks of digital I/O on the board. Each bank of digital I/O has 8 channels, so there are a total 48 I/O channels on the board.

2.1.4 Amplifier

The amplifier is also from Quanser Consulting, Inc. The gain is adjusted to 3 in the experiments. The measured static input and output relationship is shown in Figure 2-3. The maximum output of the amplifier is 22.76 V.

Using a signal generator, a bode plot can be obtained as shown in Figure 2-4.

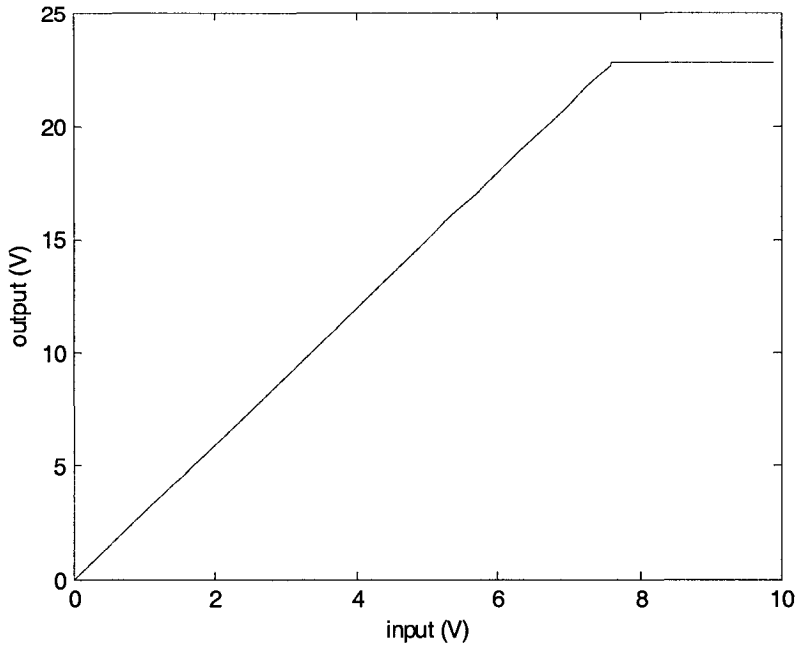

Figure 2-3 Static input and output relationship of amplifier

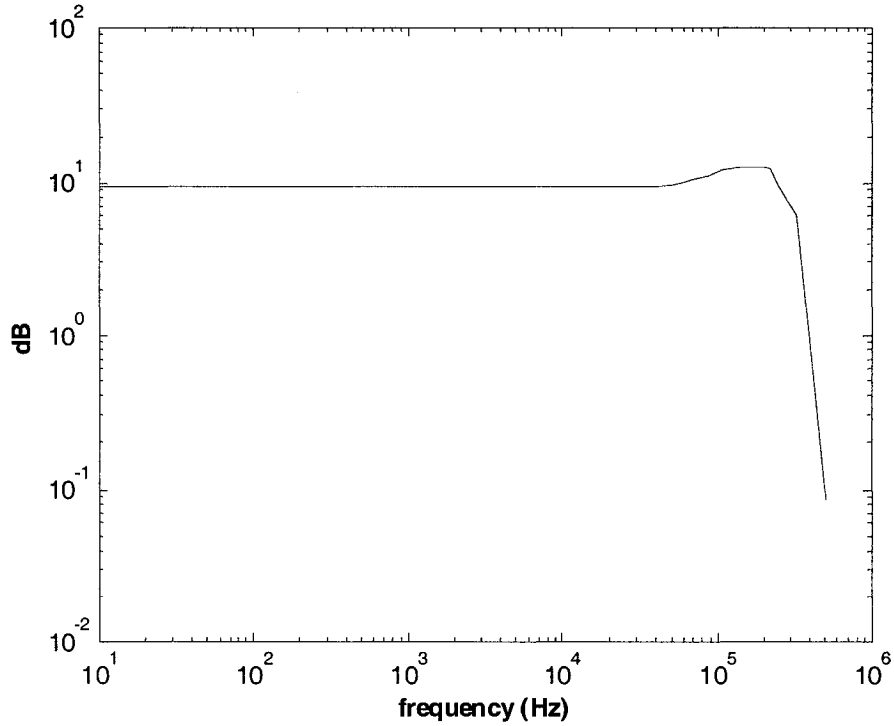

Figure 2-4 Measured bode plot of amplifier

2.1.5 Capacitance sensor

The accumeasure 5000 acquisition device is required to connect capacitance sensors. This acquisition device amplifies the sensor signal to a voltage signal that can be read by the computer and has dual channels. The measurement can reach nanometer accuracy. It is ideal for high-precision positioning and vibration applications.

The output signal for each channel is 0 to 10 V DC. The measurement range is 508 μm. In this range, the change of voltage corresponding to the change of displacement is quite linear. Every 1 V voltage change indicates a 50.8 μm displacement change in the arm.

The sensor measurement noise can be filtered by averaging the measured data, as shown in Figure 2-5. It is apparent that the noise can reach 0.002V (100 nm). If we take 100 measured data and average them, the accuracy can reach 10 nm. In Chapter 4 and Chapter 5, the data is filtered in this method.

The sensor is mounted parallel to the arm. A 1 um displacement in the sensor position is equal to the 3.8955e-5 radian.

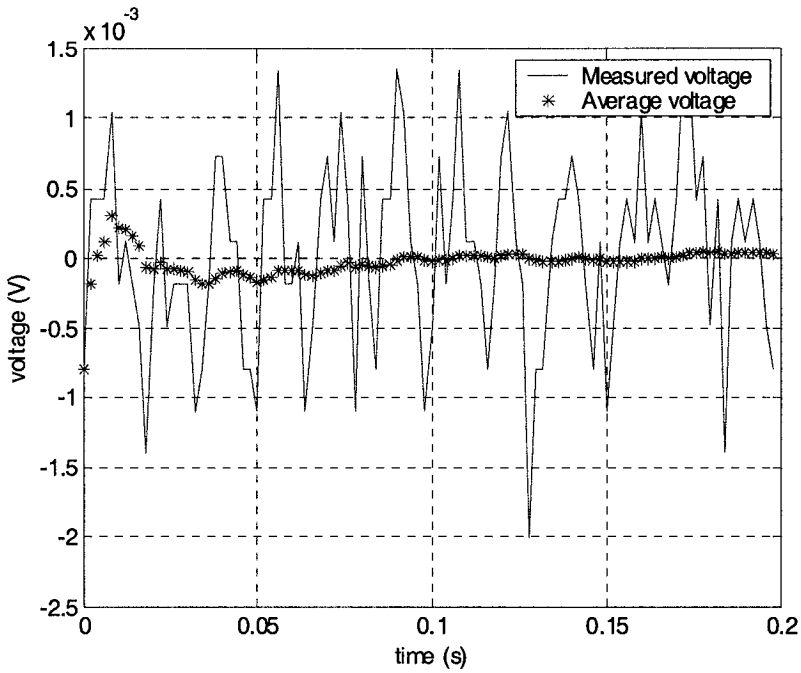

Figure 2-5 Capacitance sensor noise and filter

2.2 Harmonic drives

One of the key points of this research project is modelling the nonlinear attributes of the harmonic drives. Harmonic drives are special flexible gear transmission systems that have a non-conventional construction with teeth meshing at two diametrically opposite ends. The construction and operation of harmonic drives are in Appendix A and their advantages are listed in Appendix B. Because of their unique construction and operation, they have many useful properties. Hence, they are widely used in precision applications including wafer-handling machines in the semiconductor industry, space robots, lens grinding machines, and medical equipment. However, these drives possess nonlinear transmission attributes that are responsible for transmission performance degradation. The main nonlinear attributes are:

Kinematic error - what harmonic drive literature refers to as kinematic error is a difference between the ideal and the actual output position. In an ideal gear system, one may expect the gear transmission ratio to be constant and the output position to be proportional to the input position. However, in harmonic drives, a small amplitude of periodic kinematic error exists between the ideal and the actual output position, thereby making the gear ratio dependent on the input position. The error also has a dynamic component.

Flexibility and presliding - flexibility in a harmonic drive results from various compliant elements including the flexspline cup, elliptical ball bearing and gear teeth. Nonlinear interactions of the elliptical ball bearing, the flexspline, and the circular spline with friction at the contact surfaces along with flexibility effects produce a presliding signature. Presliding is the flexible displacement in harmonic drives. In mechanical systems, presliding makes a system's output have hysteresis attributes. A hysteresis curve can be obtained by locking its output port and controlling the input displacement to follow a periodical reference waveform. The displacement, when plotted against the output (generated due to the periodic motion), gives rise to a hysteresis signature similar to that shown in Figure 2-6. A similar hysteresis signature in the harmonic drive motors is measured in Figure 3-3 and is simulated in Figure 5-31 and Figure 5-32.

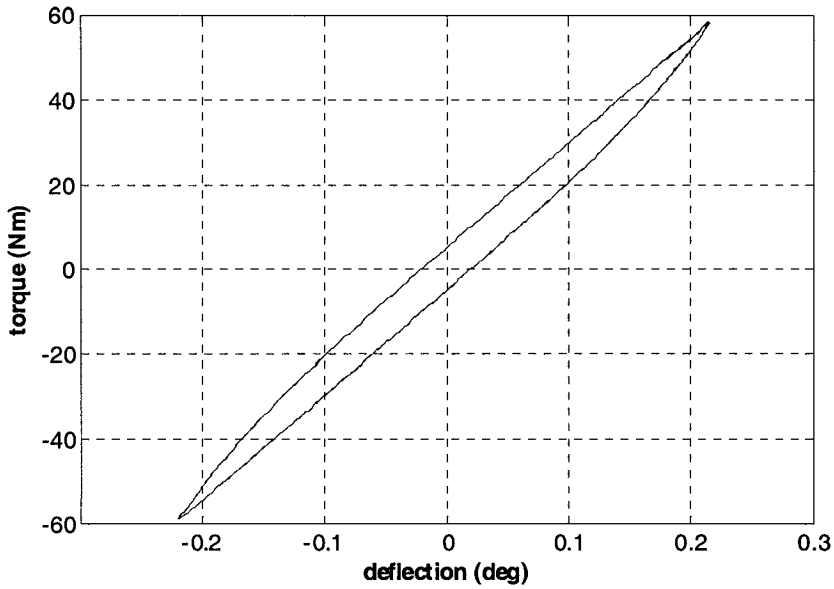

Figure 2-6 Typical hysteresis behaviour in the harmonic drives

Friction - friction is a critical problem for precision positioning. Friction in the harmonic drive, as in any other system, produces nonlinear dynamic effects, especially at slow velocities and when there is a reversal in the direction motion. The additional peculiarity of harmonic drive friction is its periodic dependence on the motor or wave generator position, and also on the load or circular spline position as illustrated in Chapter 3. The friction in a harmonic drive is very complicated and has significant influence on positioning.

2.3 Modelling approximations

2.3.1 Initial modelling approximations

The arms of the manipulator are driven by harmonic drive motors. Because the hysteresis effect in harmonic drives is relatively small, especially in precision impulse

control, it can be negligible. A harmonic drive can be modelled as two masses connected with a spring, as shown in Figure 2-7 [1] (see Appendix A for harmonic drive construction and operation). The control input acts on the motor and wave-generator inertia J_m, which is connected via a gear reduction r to the flexspline and arm inertia J_l. The flexibility of the harmonic drive motor plays a significant role in system dynamics and is modelled using a torsional spring that produces a torque T_s.

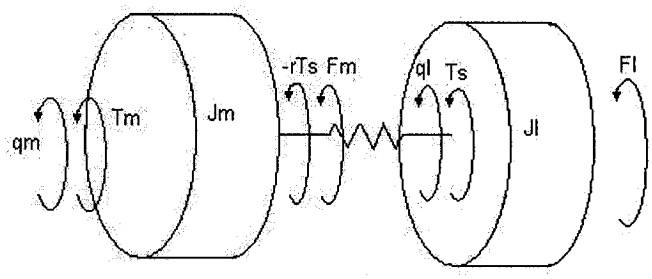

Figure 2-7 Harmonic drive model

F_m and F_l stand for frictions in motor side and load side respectively in Figure 2-7. Newton's second law is used for both motor and load side:

$$J_m \ddot{q}_m = T_m + F_m - rT_s \qquad (2\text{-}1)$$

$$J_l \ddot{q}_l = T_s + F_l \qquad (2\text{-}2)$$

q_m and q_l are the positions of motor and load inertia; T_m is the motor input torque; T_s is given by:

$$T_s = K_s(rq_m - q_l) \qquad (2\text{-}3)$$

K_s is a spring constant of the harmonic drive.

For the armature controlled motor, the circuit is shown in Figure 2-8.

Motor torque can be written as

$$T_m = K_m i_a \tag{2-4}$$

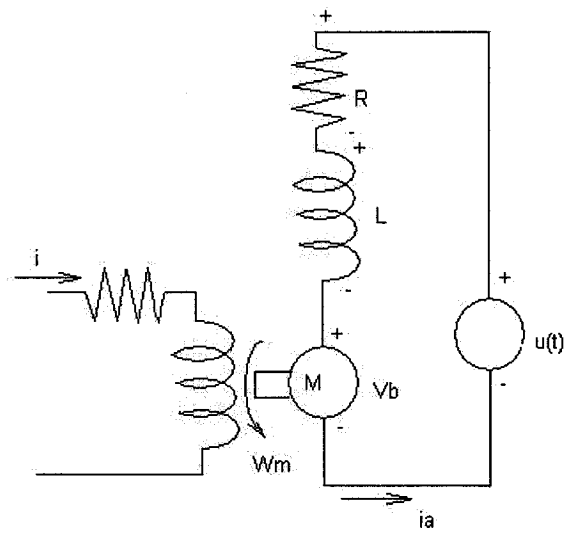

Figure 2-8 Motor circuit

K_m is the motor torque constant, i_a is the armature current. It is apparent that the input voltage is,

$$u(t) = i_a R + L\frac{di_a}{dt} + K_b \omega_m \tag{2-5}$$

where R is armature resistance, L is armature inductance, K_b is voltage constant (back emf), and ω_m is motor velocity.

From the manual, L = 2.7mH; it is very small and can be neglected. Then

$$i_a = \frac{-K_b \dot{q}_m + u(t)}{R} \tag{2-6}$$

The substitution of (2-6) into (2-4) yields

$$T_m = -\frac{K_m K_b}{R}\dot{q}_m + \frac{K_m}{R}u(t) \tag{2-7}$$

The substitution of (2-7) and (2-3) into (2-1) and (2-2) yields

$$J_m\ddot{q}_m = F_m - rK_s(rq_m - q_l) - \frac{K_m K_b}{R}\dot{q}_m + \frac{K_m}{R}u(t) \qquad (2\text{-}8)$$

$$J_l\ddot{q}_l = F_l + K_s(rq_m - q_l) \qquad (2\text{-}9)$$

2.3.2 Initial values of parameters

The initial parameter values are listed in Table 2-1.

2.3.3 Friction measurement

2.3.3.1 Friction profile

In order to measure the friction inside the harmonic drive motor, a 1.11 Ω resistor is connected in the motor circuit. The motor torque is equal to the torque constant K_m multiplied by the current across the resistor. When the velocity of the motor is constant, the motor torque is equal to friction.

As mentioned in Chapter 1, friction is dependent not only on motor side position, but also on load side position. In this manipulator, the arm can move in a range of about 2.6 radians. That is, the motor can move in a range of 2.6×80 = 208 radians. When the arm moves at a velocity of 0.11 rad/s, the friction in this range is measured as shown in Figure 2-9. This verifies that the friction in the harmonic drive is quite position dependent.

Table 2-1 Initial parameter values

item	unit	value	initial estimate	measurement method
motor side inertia J_m	Kgm^2	2.435e-7	Manual	
load side inertia J_l	Kgm^2	3.51e-5	Estimated	
spring constant K_s	Nm/rad	50.42		In Chapter 3
gear ratio r		1:80	Manual	
motor torque constant K_m	Nm/A	1.11	Manual	
voltage constant K_b	V/rpm	0.12	Manual	
armature resistance R	Ω	8.6	Manual	
viscous coefficient in motor side b_m	Nm/rad/s	0.0004		In Chapter 2
viscous coefficient in load side b_l	Nm/rad/s	5e-3	Estimated	
motor side static friction f_{sm}	Nm			measured in Chapter 2&3
motor side Coulomb friction f_{cm}	Nm			measured in Chapter 2&3
load side static friction f_{sl}	Nm	0.0011		In Chapter 3
load side Coulomb friction f_{cl}	Nm	0.0011		In Chapter 3

From the motor side, the kinematic error between the wave generator and flexspline causes the friction variation. The friction changes periodically with every motor revolution, as shown in Figure 2-10. From the load side, the kinematic error between circular spline and flexspline causes friction change. When the arm moves from 0 to 2.6 radians, the friction decreases. We can conclude that the friction also changes periodically with the arm position. The period is 2π of the arm position. The average friction is plotted in Figure 2-11.

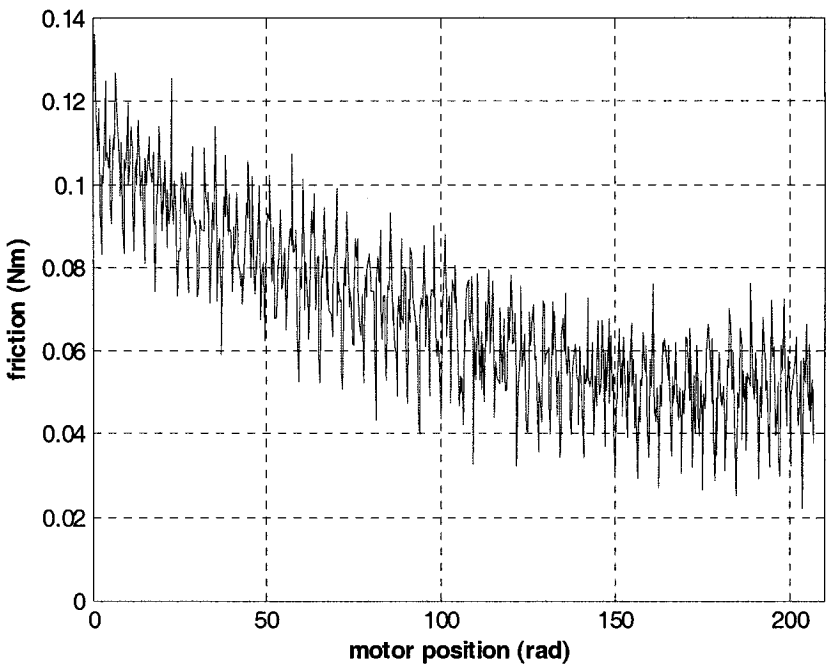

Figure 2-9 Friction profile in harmonic drive

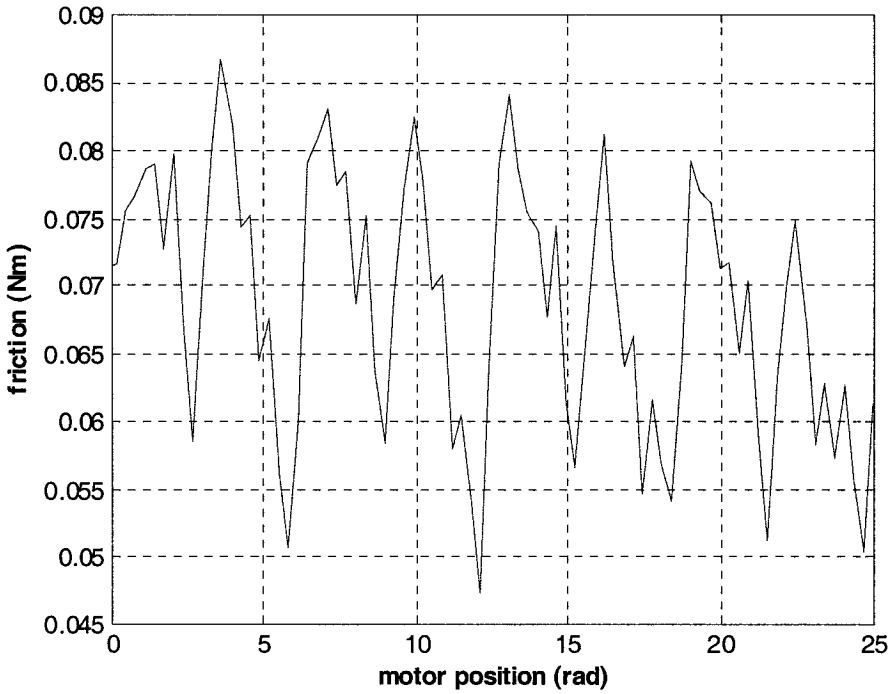

Figure 2-10 Friction variation with motor position

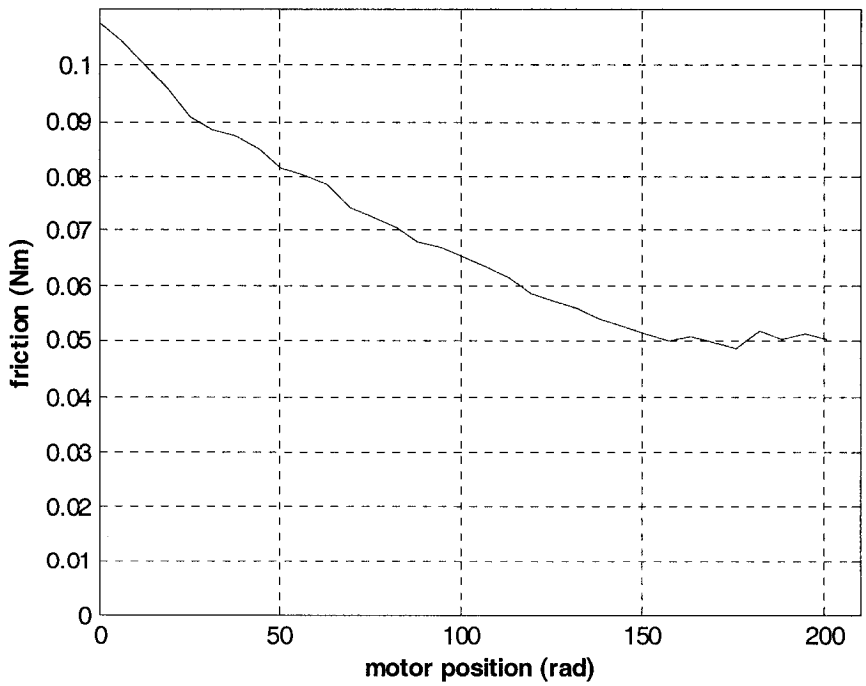

Figure 2-11 Average friction

2.3.3.2 Coulomb friction

In this thesis, a range of about 45 degrees is chosen as the "work-range". The friction in the work-range will be measured in detail. The start-point of the work-range is found by a fixed sensor and the motor encoder index pulse.

When the motor moves at a very low velocity, for example at 0.8 rad/s (the velocity of the output side of the harmonic drive is 0.01 rad/s), the measured friction can be considered Coulomb friction. The Coulomb friction profile in the work-range is shown in Figure 2-12.

The average of the friction in the work-range is shown in Figure 2-13. The shape of the curve is parabolic.

The average friction torque in the work-range is 0.0635 Nm.

2.3.3.3 Viscous friction

The measured friction in the work-range is quite consistent at different velocities. For example, the Coulomb friction and friction at a velocity of 2.18 rad/s are shown in Figure 2-14. The friction at a velocity of 2.18 rad/s is a little bigger than Coulomb friction. This is the effect of viscous friction.

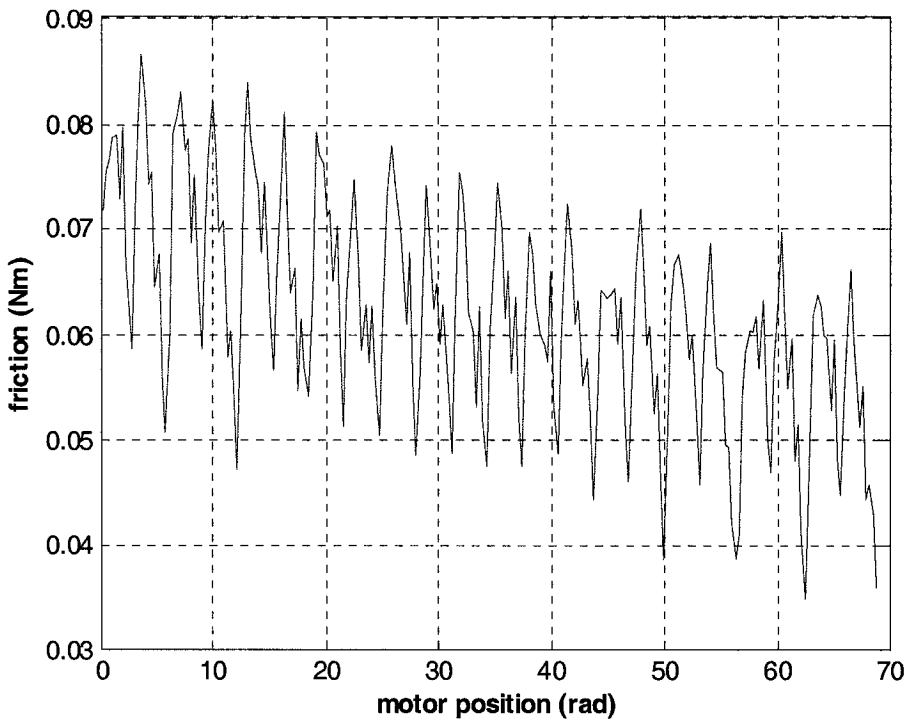

Figure 2-12 Coulomb friction in work-range

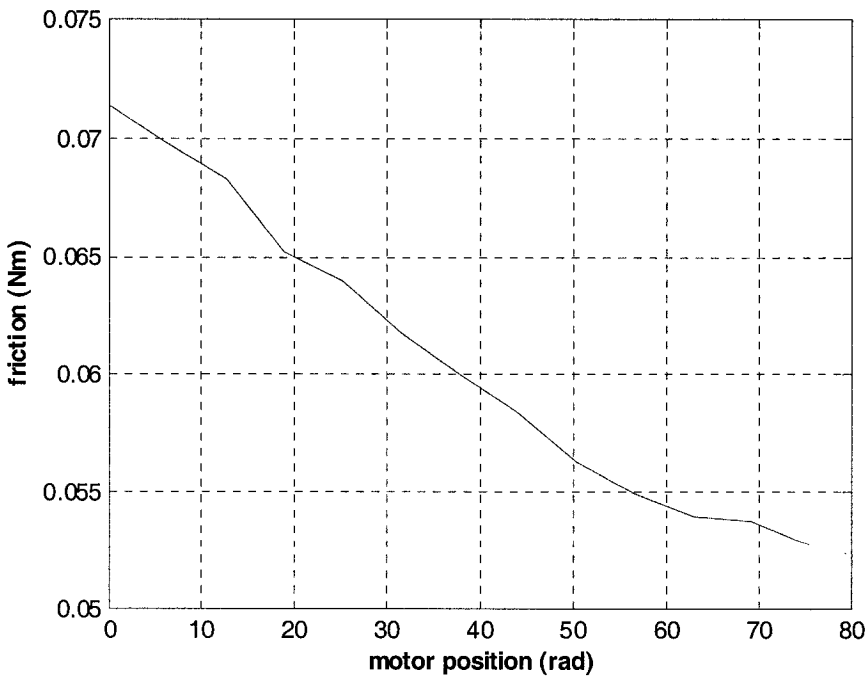

Figure 2-13 Average of Coulomb friction

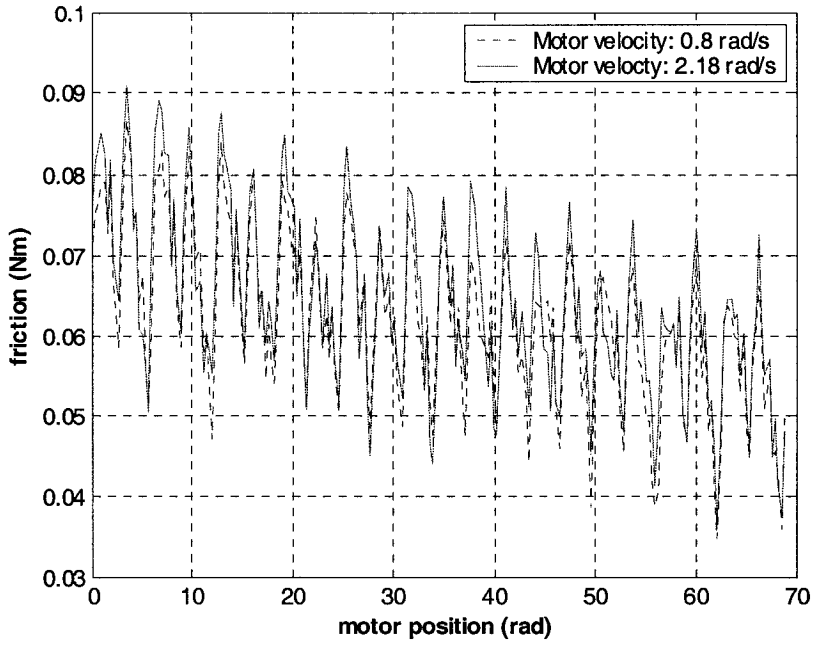

Figure 2-14 Friction at two different velocities

2.3.3.4 Friction modelling

Because the friction varies periodically and the period is 2π, the friction can be modelled as follows: the average of the friction can be modelled as a parabolic curve, periodical changes of friction can be modelled as a Fourier series, and the viscous effect can be modelled as a viscous coefficient multiplied by motor velocity.

The average Coulomb friction is simulated using a second order polynomial:

$$f_{aver} = s_1 q_m^{\ 2} + s_2 q_m + s_3 \qquad (2\text{-}10)$$

By using the 'fminunc' function in Matlab, it is possible to minimize the Euclidian norm of error between the simulation and experimental data. The coefficients obtained are:

s_1= 1.5738e-006 s_2 = -3.7901e-004 s_3 = 0.0720

The simulation and experimental data are plotted in Figure 2-15.

For the periodical term of friction, the first 2π is chosen for our simulation period. In the period of 0-2π, we remove the average of the friction from the experimental data. Using the 10^{th} order of Fourier series to simulate it, the friction can be expressed as:

$$f_{peri} = \frac{a_0}{2} + \sum_{k=1}^{10} [a_k \cos(kq_m) + b_k \sin(kq_m)] \qquad (2\text{-}11)$$

The Fourier coefficients (a_k, b_k) are obtained using numerical integration:

$$a_k = \frac{1}{\pi} \int_0^{2\pi} f_{peri}(q_m) \cos(kq_m) dq_m \qquad (2\text{-}12)$$

$$b_k = \frac{1}{\pi} \int_0^{2\pi} f_{peri}(q_m) \sin(kq_m) dq_m \qquad (2\text{-}13)$$

The coefficients are obtained in Table 2-2. The experiment and simulation for periodical friction in the first 2π are shown in Figure 2-16.

The Coulomb friction is the sum of the periodical term and average term:

$$f_{coul} = f_{aver} + f_{peri} = s_1 q_m^{\ 2} + s_2 q_m + s_3 + \frac{a_0}{2} + \sum_{k=1}^{10} [a_k \cos(\mathrm{k}\, q_m) + b_k \sin(\mathrm{k}\, q_m)] \qquad (2\text{-}14)$$

The final simulation result of Coulomb friction is shown in Figure 2-17. The experimental data is also plotted for comparison.

By measuring the friction in the work-range at different velocities as in section 2.3.3.3, and calculating the average value of friction, a viscous tendency can be found and it is illustrated in Figure 2-18. The minimization of the Euclidian norm of error between the simulation and experimental data points is shown in Figure 2-18:

$$f_{visc} = b_m \dot{q}_m + \mathrm{B} \qquad (2\text{-}15)$$

b_m = 0.0004 Nm/rad/s, B = 0.0642

The viscous coefficient b_m is 0.0004 Nm/rad/s.

Table 2-2 Coefficients of periodical friction

a_0	0		
a_1	-0.0039	b_1	0.0037
a_2	0.0013	b_2	0.0098
a_3	0.0003	b_3	-0.0011
a_4	0.0041	b_4	0.0034
a_5	0.0004	b_5	-0.000677
a_6	0.0031	b_6	-0.0011
a_7	0.0017	b_7	0.00031
a_8	-0.0017	b_8	-0.00041
a_9	0.0010	b_9	0.000381
a_{10}	0.0022	b_{10}	0.0000

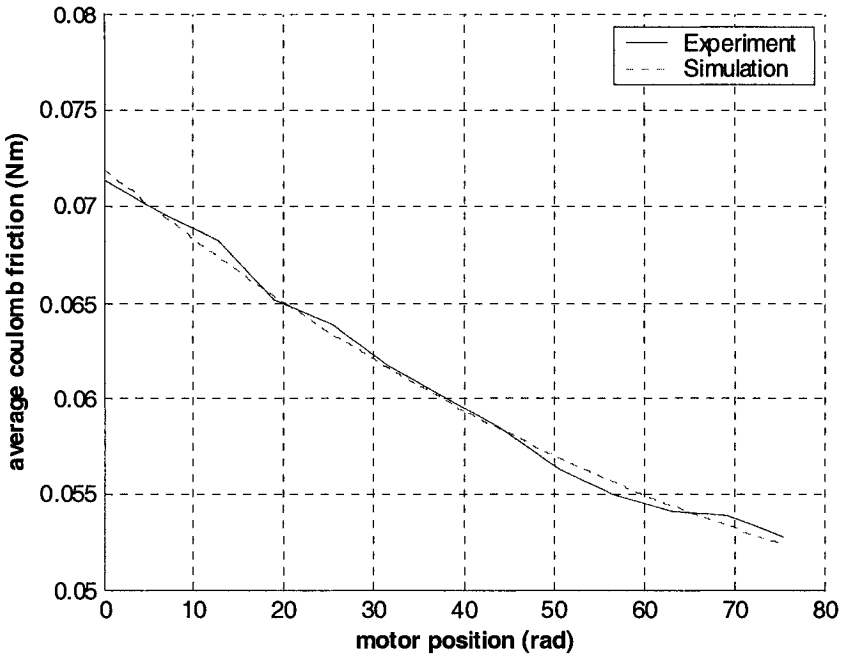

Figure 2-15 Average Coulomb friction: experiment and simulation

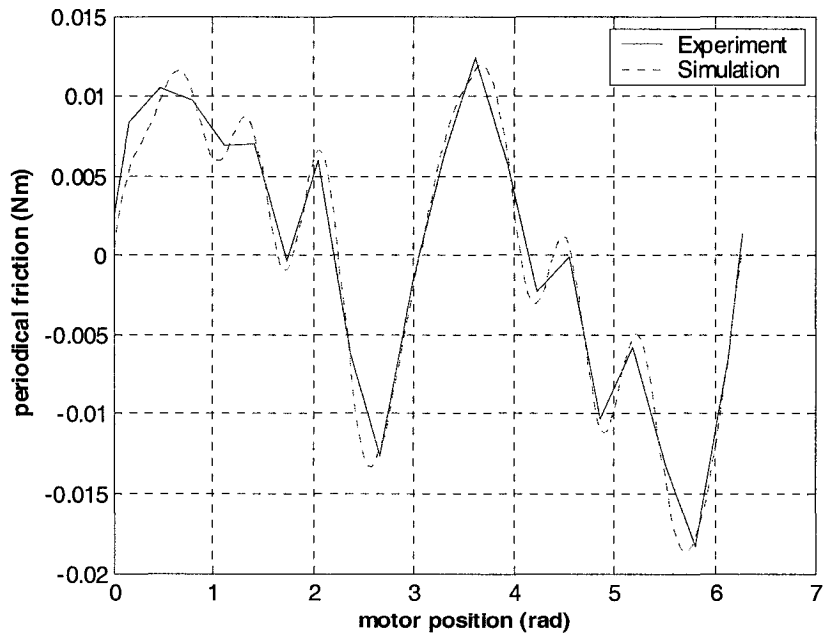

Figure 2-16 Periodical friction: experiment and simulation

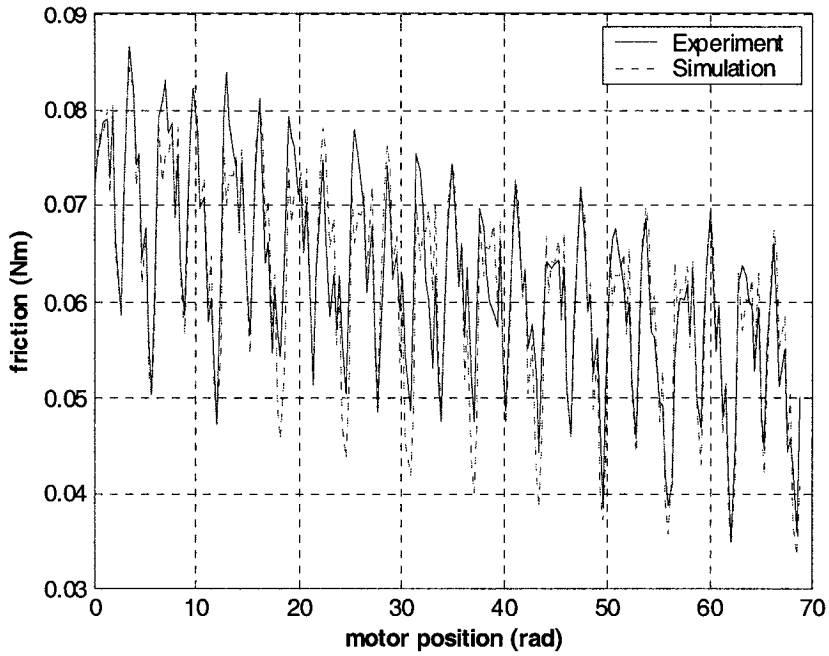

Figure 2-17 Coulomb friction: experiment and simulation

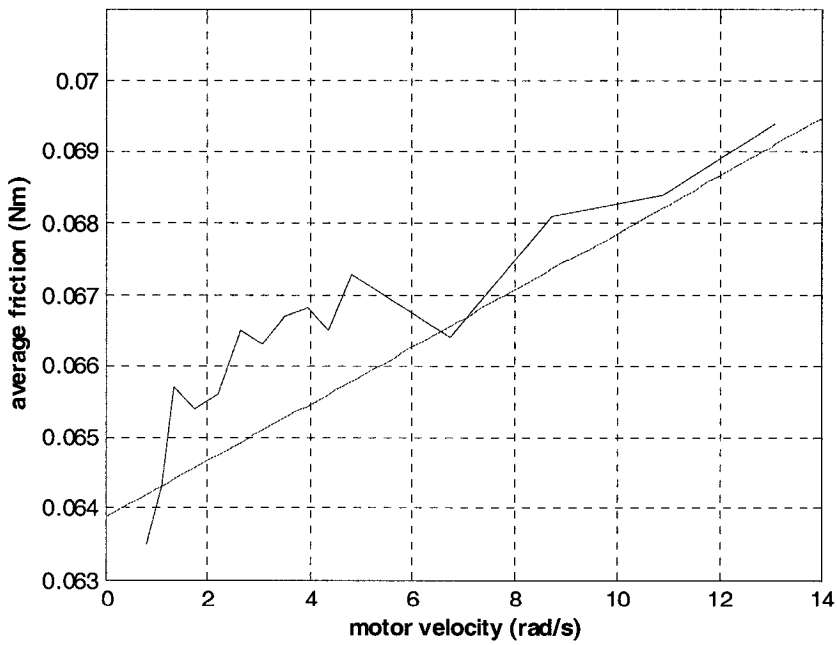

Figure 2-18 Viscous friction

2.3.3.5 Static friction

Static friction can only be measured while the motor is moving. Therefore, only a manual measurement method can be used. Because noise exists in the system, and the kinematic error changes irregularly for different positions, static friction cannot be averaged between sampling times. The voltage across the $1\,\Omega$ resistor can be measured as the input voltage increases. When the motor begins moving, the voltage across the resistor can be used to calculate the static friction torque. However, the voltage when the motor starts moving often changes dramatically, and so the measured value is not accurate. In this thesis, only the static friction in the first π radian range is measured. The result is shown in Figure 2-19. The graph illustrates that there is a consistency between static and Coulomb friction. The average static friction is larger than that of Coulomb by about 3.88%. We can simply assume that the static friction is 1.0388 times that of the Coulomb friction at any position. Static friction $f_{sm}(q_m)$ can therefore be expressed as:

$$f_{sm}(q_m) = (s_1 q_m^2 + s_2 q_m + s_3 + \frac{a_0}{2} + \sum_{k=1}^{10} [a_k \cos(\mathrm{k} q_m) + b_k \sin(\mathrm{k} q_m)])1.0388 \qquad (2\text{-}16)$$

The simulation result is shown in Figure 2-20.

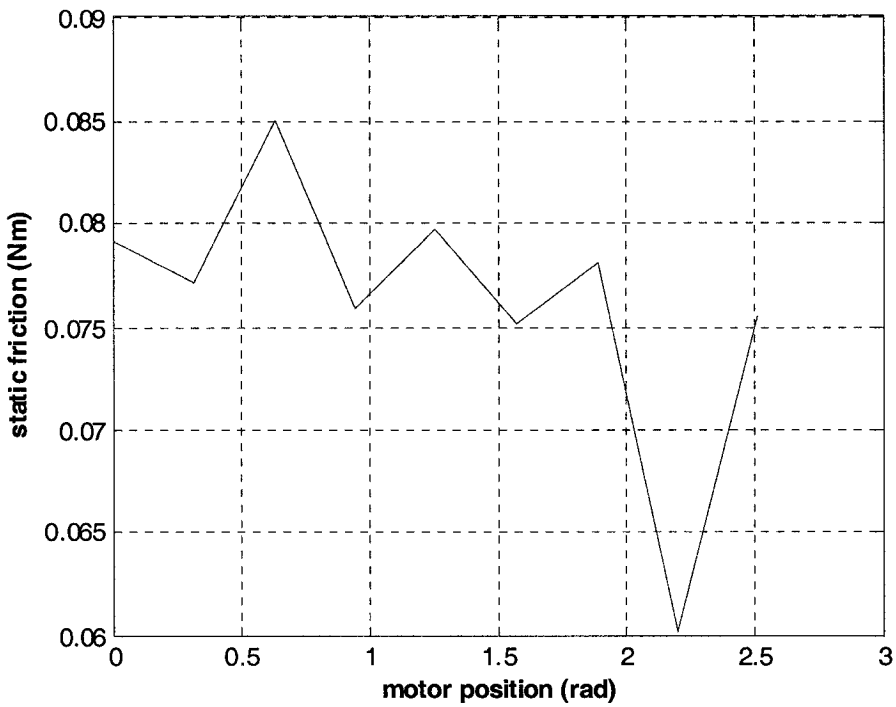

Figure 2-19 Static friction

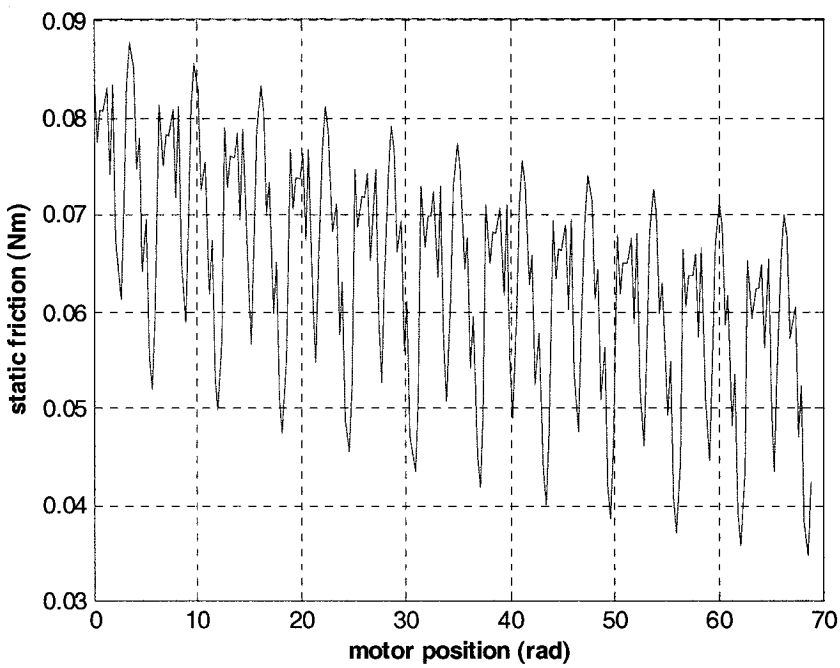

Figure 2-20 Simulation of static friction

2.3.3.6 Overall friction model

We can assume that the viscous coefficient is the same for different positions. This assumption is reasonable because the conditions affecting the viscous coefficient, such as lubrication, are the same for the different positions. We also assume that the periodical friction is not velocity dependent, just that the average friction varies with the velocity. So the overall friction $f_m(q_m, \dot{q}_m)$ can be expressed by:

$$F_m = -\psi_m \qquad \text{if} \quad \dot{q}_m = 0, \quad |\psi_m| \le f_{sm}$$

$$F_m = -\text{sgn}(\psi_m) f_{sm} \qquad \text{if} \quad \dot{q}_m = 0, \quad |\psi_m| > f_{sm} \qquad (2\text{-}17)$$

$$F_m = (s_1 q_m^2 + s_2 q_m + s_3) \times ((\dot{q}_m - \text{Vc}) \times 0.0004 + 1)$$

$$+ \frac{a_0}{2} + \sum_{k=1}^{10} [a_k \cos(\text{k} q_m) + b_k \sin(\text{k} q_m)]) \qquad \text{if} \quad |\dot{q}_m| > 0$$

where

$$\psi_m = -rK_s(rq_m - q_l) + \frac{K_m}{R} u(t)$$

ψ_m is input torque when $\dot{q}_m = 0$, f_{sm} is calculated in equation (2-16), and Vc=0.8 rad/s stands for the motor side velocity of Coulomb friction.

2.3.3.7 Average friction model

The measured friction is quite position dependent. In the following precision impulse control, the control range is about 500um. In this small range, static friction and Coulomb friction can be averaged and considered constants. The friction used in

equation (2-8) and (2-9) can be modelled as static + viscous + coulomb. This model is accurate enough for most engineering applications. The motor side and load side friction can be written as:

$$
\begin{aligned}
F_m &= -\psi_m && \text{if} \quad \dot{q}_m=0, \quad |\psi_m| \le f_{sm} \\
F_m &= -\mathrm{sgn}(\psi_m) f_{sm} && \text{if} \quad \dot{q}_m=0, \quad |\psi_m| > f_{sm} \\
F_m &= -\mathrm{sgn}(\dot{q}_m) f_{cm} - b_m \dot{q}_m && \text{if} \quad |\dot{q}_m| > 0 \qquad (2\text{-}18) \\
\psi_m &= -rK_s(rq_m - q_l) + \frac{K_m}{R} u(t)
\end{aligned}
$$

and

$$
\begin{aligned}
F_l &= -\psi_l && \text{if} \quad \dot{q}_l=0, \quad |\psi_l| \le f_{sl} \\
F_l &= -\mathrm{sgn}(\psi_l) f_{sl} && \text{if} \quad \dot{q}_l=0, \quad |\psi_l| > f_{sl} \\
F_l &= -\mathrm{sgn}(\dot{q}_l) f_{cl} - b_l \dot{q}_l && \text{if} \quad |\dot{q}_m| > 0 \qquad (2\text{-}19) \\
\psi_l &= K_s(rq_m - q_l)
\end{aligned}
$$

ψ_l is the spring torque when $\dot{q}_l$=0, f_{sm} and f_{cm} are motor side static friction torque and Coulomb friction torque. f_{sl} and f_{cl} are load side static friction torque and Coulomb friction torque.

2.4 State equations

We define the state variables as:

$$\begin{bmatrix} x_1 \\ x_2 \\ x_3 \\ x_4 \end{bmatrix} = \begin{bmatrix} q_m \\ \dot{q}_m \\ q_l \\ \dot{q}_l \end{bmatrix} \tag{2-20}$$

Then, the equations of (2-8) and (2-9) can be written in state variable format:

$$\begin{bmatrix} \dot{x}_1 \\ \dot{x}_2 \\ \dot{x}_3 \\ \dot{x}_4 \end{bmatrix} = \begin{bmatrix} x_2 \\ \frac{F_m}{J_m} - \frac{rK_s}{J_m}(rx_1 - x_3) - \frac{K_m K_b}{J_m R} x_2 + \frac{K_m}{J_m R} u(t) \\ x_4 \\ \frac{F_l}{J_l} + \frac{K_s}{J_l}(rx_1 - x_3) \end{bmatrix} \tag{2-21}$$

Chapter 3 Parameter Identification

The parameters used in the mathematic models should be accurate. In this chapter, the parameters are identified in order to make the simulation as close to the experiment as possible.

3.1 Initial parameter estimates

3.1.1 Armature resistance R

From the manual, the armature resistance of the RH-5A-5502 harmonic drive motor is R= 8.6Ω. The armature resistance of the harmonic drive motor can also be tested manually by moving the motor in one direction, and using a multi-meter to measure the armature resistance for every 2 degrees. The measured armature resistance is plotted in Figure 3-1. Since noise exists in the measurement, there are spikes in the graph. The measured resistance is not accurate. The average value of R will be tuned in the following sections.

3.1.2 Spring constant K_s

The harmonic drive has some flexibility. That is, when torque is applied between the input and output, there is elastic deformation between them. The spring torque can be expressed as:

$$T_s = K_s \ (rq_m - q_l)$$

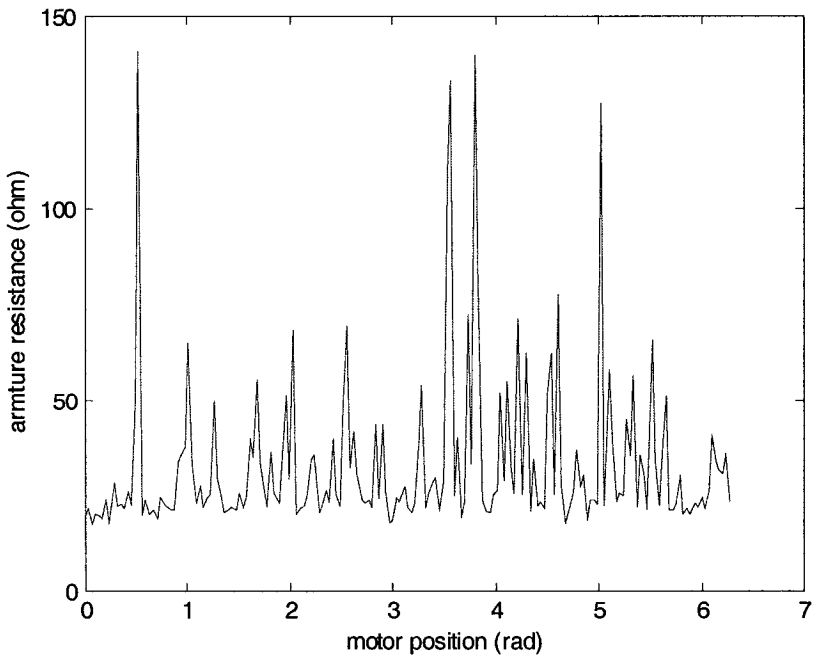

Figure 3-1 Armature resistance

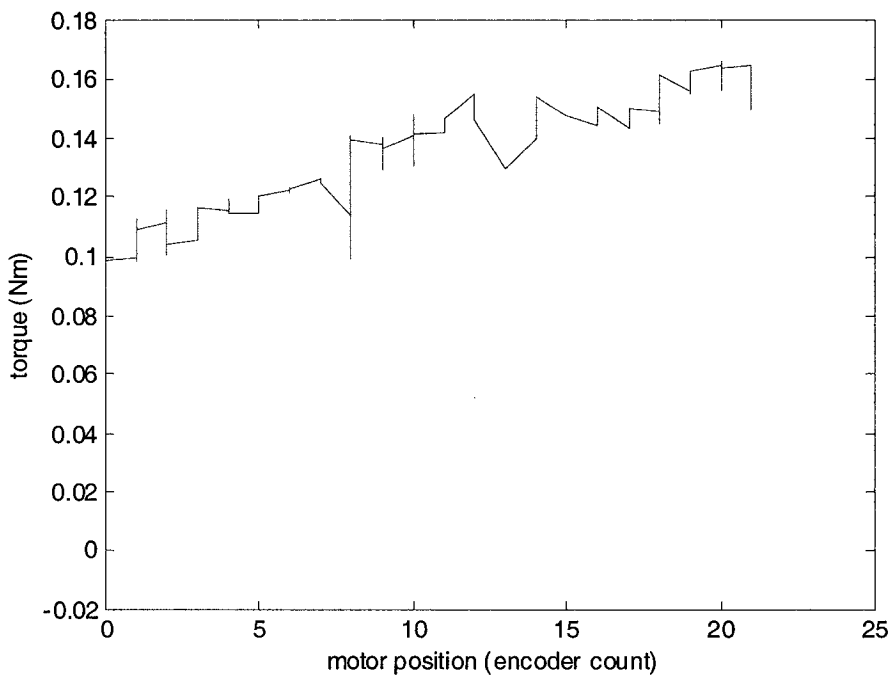

Figure 3-2 Flexibility in harmonic drive

In order to measure the spring constant K_s, the load side position q_l is fixed, and when torque is applied to the motor side, the motor position q_m is obtained. A series of q_m and their corresponding torque are obtained through an experiment, as shown in Figure 3-2.

From the above experimental data, K_s can be calculated. That is, K_s=0.00275 Nm/encoder count. If it is equivalent to the load side, the spring constant is 50.42 Nm/rad.

3.1.3 Presliding displacement

When the motor is driven forward and then backward, the motor position and arm position can be measured as demonstrated by Figure 3-3. The hysteresis signature can be clearly seen. From this figure, the average presliding displacement can also be obtained. The presliding displacement $2\Delta\theta$ is equal to the 0.7942 encoder count.

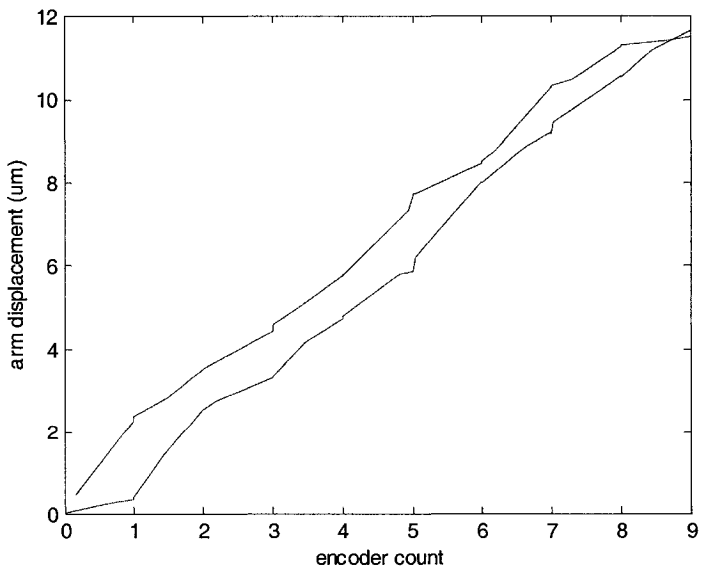

Figure 3-3 Hysteresis signature in harmonic drive

3.1.4 Parameters classification

All of the parameters listed in Table 2-1 are significant except the motor side and load side viscous coefficients. This is because the viscous coefficients are very small and have a very small effect on the simulation and experimental results. The other parameters are important because they have a much stronger effect on the system's output. The parameters can be classified as:

1) Significant parameters: J_m, J_l, K_m, K_b, R, K_s, f_{cm} (f_{sm}), f_{cl} (f_{sl})

2) Insignificant parameters: b_m, b_l

b_m and K_s have been already measured. K_m is believed to be accurate from the manual. So these parameters can also be classified in another way:

A) Parameters that are well known: K_s, K_m, b_m

B) Parameters that are not well known: J_m, J_l, K_b, R, b_l, f_{cm} (f_{sm}), f_{cl} (f_{sl})

In the precision position control, the control range is normally very small. Friction can be considered a constant average value in that small range. In the following tuning process, the static frictions both in motor side and load side are assumed to be equal to Coulomb friction. Where $f_{cm} = f_{sm}$, and $f_{cl} = f_{sl}$. The constant average frictions are not known now and are still classified as not well-known parameters.

Now we define those parameters that are important but not well known as 'tuneable parameters'. These parameters are: J_m, f_{cm}, K_b, R, J_l, and f_{cl}. The first four parameters have more effect on the motor side position, but they also have an effect on load side position. The last two parameters have less effect on the motor side position,

but they do have much effect on the load side position.

There are two steps in the following tuning process: first, J_m, f_{cm}, K_b and R are tuned to make motor side simulation results consistent with the experiment. Second, J_l and f_{cl} are tuned to make the load side simulation results consistent with the experiment. Because the capacitance sensor can only measure load side positions in a region of 508 μm, it is hard to keep the low-frequency open-loop experiment in that range. Instead, we use a close-loop experiment with small proportional gain Kp to tune the parameters.

3.1.5 Parameters tuning: J_m, f_{cm}, K_b and R

These parameters are tuned in two steps. In the first step, large ranges of values are taken since we do not know which range the optimal values will fall into. Ten values are used respectively for the simulation as shown in Table 3-1. The difference between the real J_m and the value from the manual should be small and is taken from 2.1e-7 to 2.55e-7 Kgm^2. R is taken from 8.6 Ω (data from manual) to 26 Ω; the measured f_{cm} is around 0.07 Nm, so we take f_{cm} to be from 0.04—0.09Nm; K_b is 0.12 in the manual, so K_b is taken to be from 0.07—0.25V/rpm. Seven frequency experiments (0.2Hz, 0.5Hz 1Hz, 2Hz, 5Hz, 10Hz, 20Hz) are used to minimize the least-square value between experiment and simulation. We take 85 points in every frequency in four periods. The cost function is:

$$V_{ls} = \sum_{1}^{7}\sum_{1}^{85}(q_{simu} - q_{ex})^2 \qquad (3\text{-}1)$$

where q_{simu} is the motor position simulation value, and q_{ex} is the motor position experimental data.

It is found that when J_m =2.25×e-7 Kgm^2, R=14 Ω, K_b =0.21 V/rpm, and f_{cm} =0.045 Nm is an optimal value. That is to say, the optimal value should be: J_m =(2.2—2.3)×e-7 Kgm^2, f_{cm} = (0.04--0.05) Nm, K_b =(0.19—0.23) (V/rpm), and R= (12—16)Ω.

Table 3-1 Tuning parameters

item	value									
J_m (×e-7 Kgm^2)	2.1	2.15	2.2	2.25	2.3	2.35	2.4	2.45	2.5	2.55
f_{cm} (Nm)	0.04	0.045	0.05	0.055	0.06	0.065	0.07	0.075	0.08	0.09
K_b (V/rpm)	0.07	0.09	0.11	0.13	0.15	0.17	0.19	0.21	0.23	0.25
R(Ω)	8.6	10	12	14	16	18	20	22	24	26

In the second step, we take ten values for each parameter in the above range, and repeat the above optimization process. The final optimal parameters can be obtained as: J_m =2.23×e-7 Kgm^2, f_{cm} =0.048 Nm, K_b = 0.21 (V/rpm), and R=14 Ω. The motor side position of experiment and simulation are plotted in Figure 3-4 through Figure 3-10.

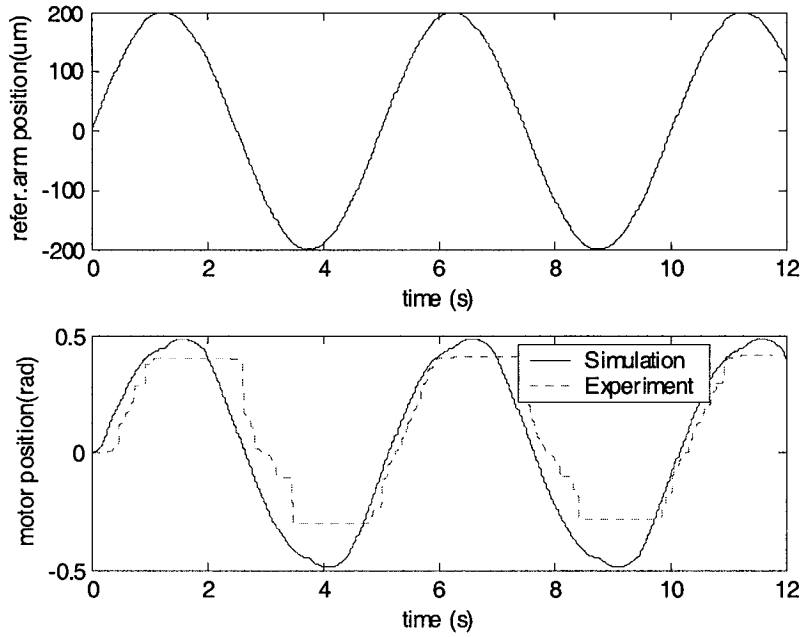

Figure 3-4 Frequency 0.2Hz

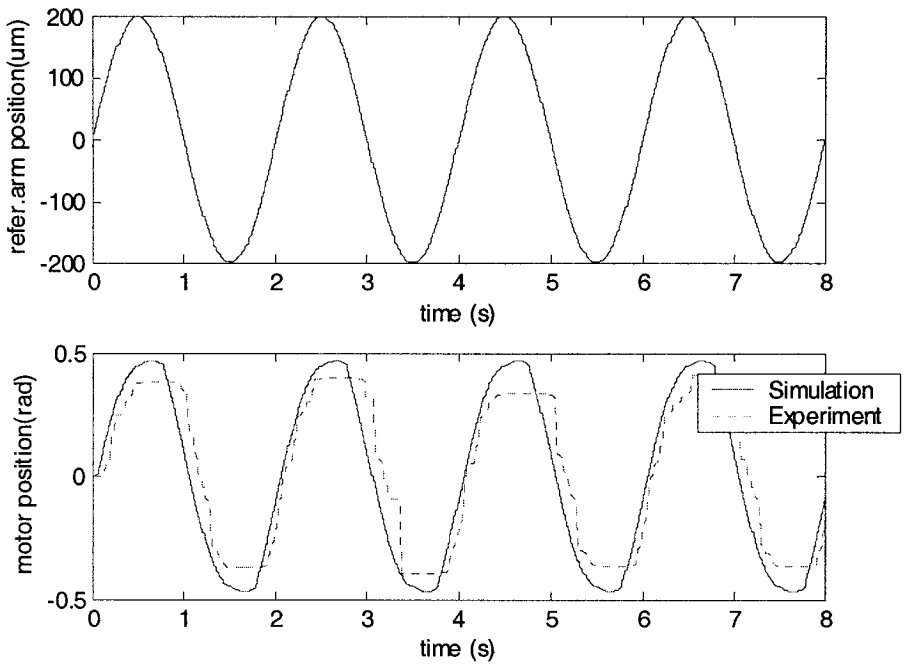

Figure 3-5 Frequency 0.5Hz

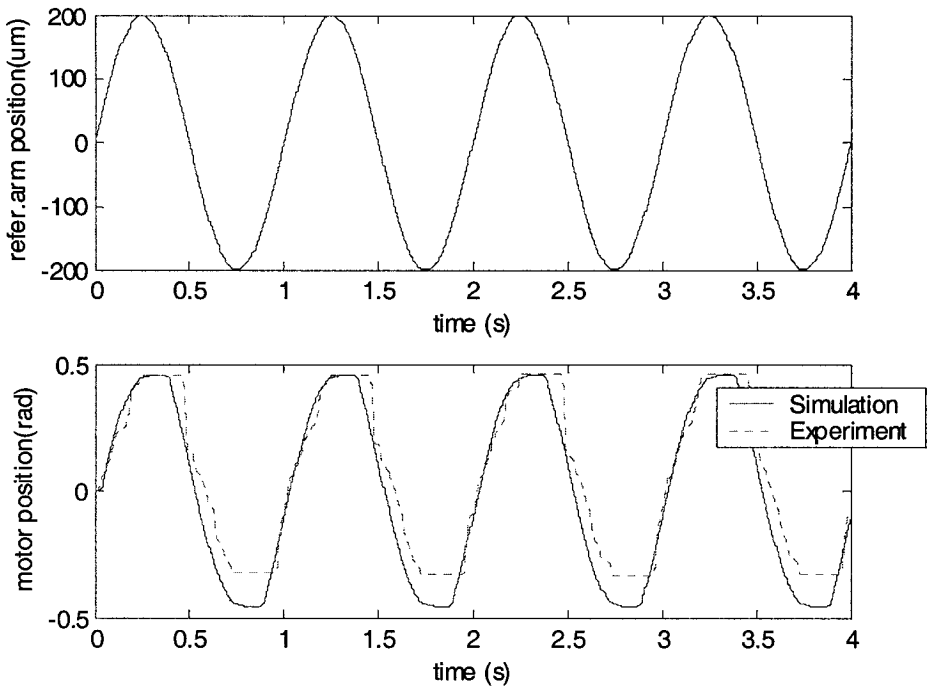

Figure 3-6 Frequency 1Hz

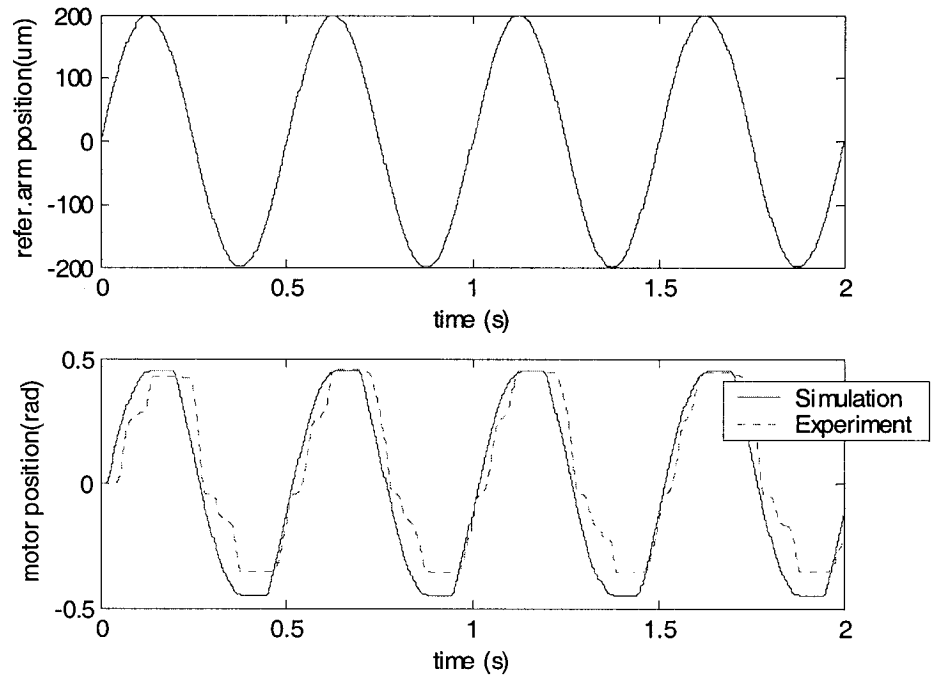

Figure 3-7 Frequency 2Hz

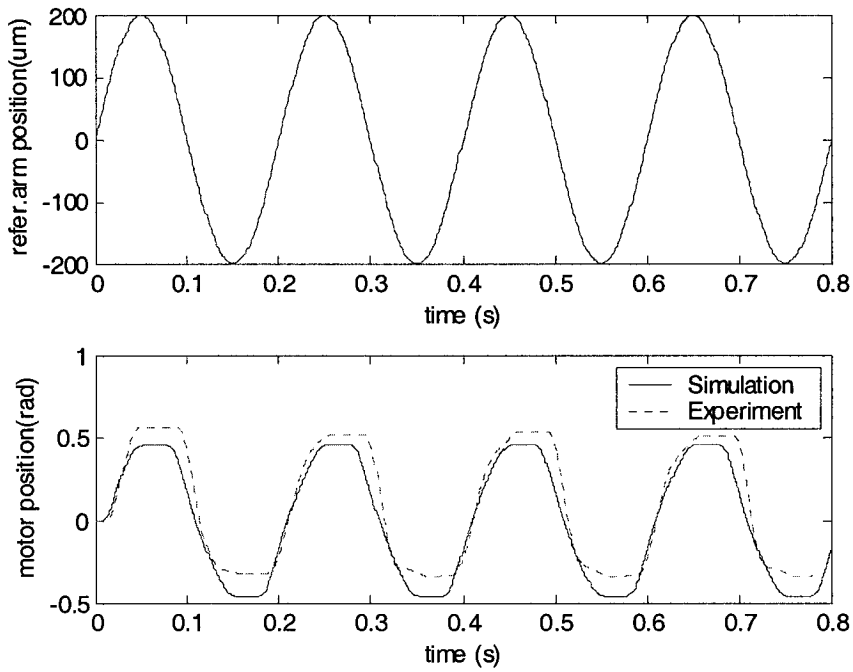

Figure 3-8 Frequency 5Hz

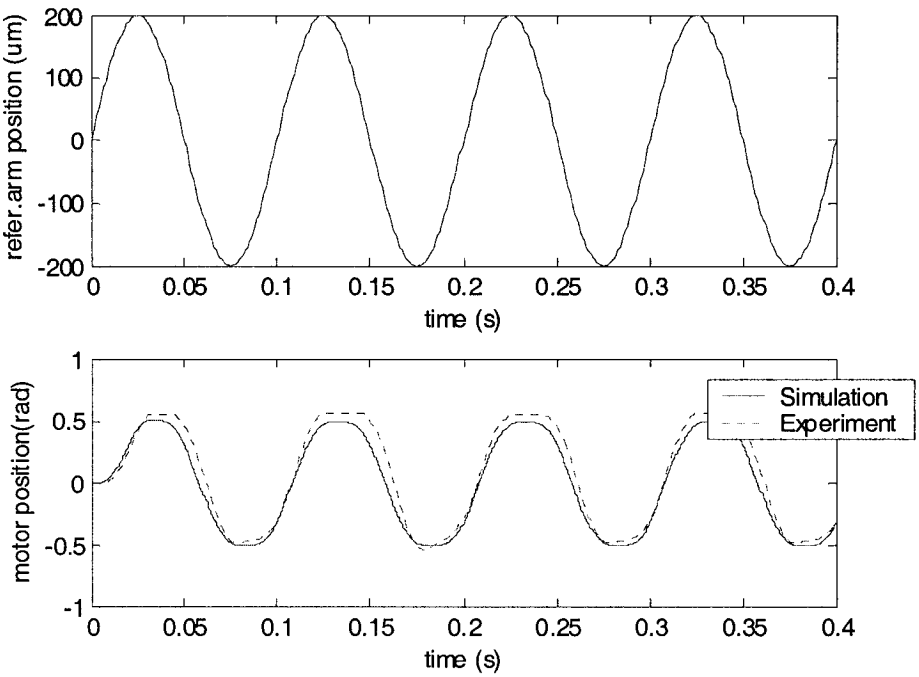

Figure 3-9 Frequency 10 Hz

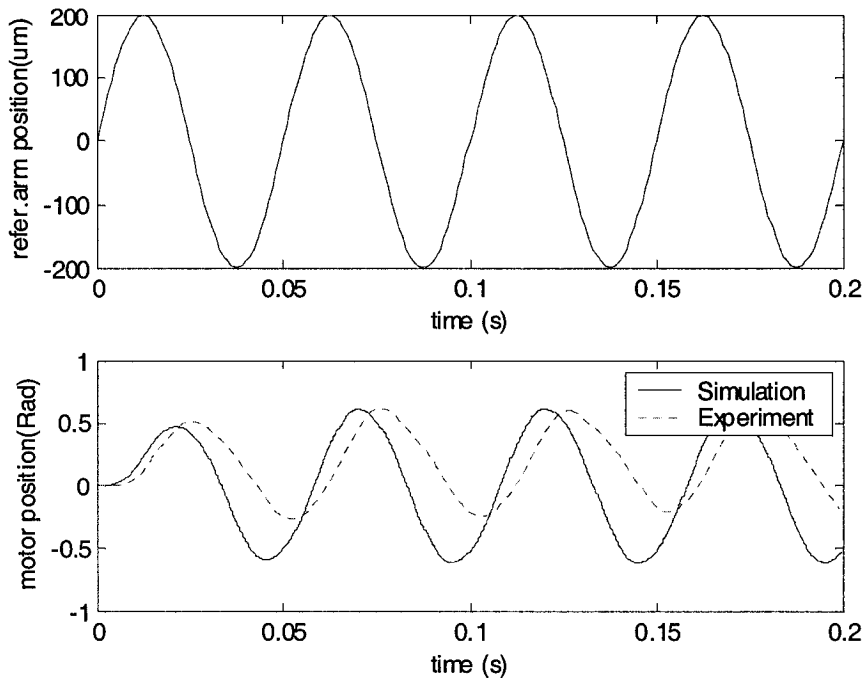

Figure 3-10 Frequency 20 Hz

3.1.6 Parameters tuning: J_l, and f_{cl}

Seven frequencies (0.2Hz, 0.5Hz, 1Hz, 2Hz, 5Hz, 10Hz, 20Hz) are used in this experiment to minimize to the least-square value between the simulations and experiments. The cost function is the same as with (3-1), but here q_{simu} is the load side position simulation value, and q_{ex} is the load side position experimental value. Since the parameters J_l and f_{cl} have no priori, they also have to be tuned by two steps. First, as shown in the previous section, we find a reasonable priori for J_l and f_{cl}. Then the parameters can be finely tuned.

First, J_l, and f_{cl} are estimated. A large range of values are taken as shown in Table 3-2.

Table 3-2 Initial value of J_l, and f_{cl}

parameter	value					
$J_l(Kgm^2)$	1e-6	5e-6	1e-5	5e-5	1e-4	5e-4
f_{cl} (Nm)	0.0001	0.0005	0.001	0.005	0.01	0.05

Using the least-square process, it is found that the optimal values lie in: J_l= 5e-5—5e-4 (Kgm^2), f_{cl} = 0.001-0.014 (Nm)

Now the values of J_l, and f_{cl} are taken as shown in Table 3-3.

Table 3-3 Fine value of J_l, and f_{cl}

parameter	value							
$J_l(Kgm^2)$	5e-5	7e-5	9e-5	1e-4	2e-4	3e-4	4e-4	5e-4
f_{cl} (Nm)	0.001	0.003	0.005	0.007	0.009	0.01	0.012	0.014

After repeating the process by searching the optimal range, the final optimal value can be found: J_l=9.4e-5(Kgm2), f_{cl}=0.0018(Nm).

Using the above optimal parameters, the motor side and load side position simulation results and comparisons with experiments are shown in Figure 3-11 through Figure 3-17.

The simulation and experiment have a good consistency at low frequencies. In high frequencies (20Hz), there is small difference between them. This may be caused by some un-modelled dynamics in the system.

The final values of the parameters are listed in Table 3-4.

Table 3-4 Final parameter values

item	unit	value
motor side inertia J_m	Kgm^2	2.23e-7
load side inertia J_l	Kgm^2	9.4e-5
spring constant K_s	Nm/rad	50.42
gear ratio r		1/80
motor torque constant K_m	Nm/A	1.11
voltage constant K_b	V/rpm	0.21
armature resistance R	Ω	14
viscous coefficient in motor side b_m	Nm/Rad/s	0.0004
viscous coefficient in load side b_l	Nm/Rad/s	5e-3
motor side static friction f_{sm}	Nm	0.048
motor side Coulomb friction f_{cm}	Nm	0.048
load side static friction f_{sl}	Nm	0.0018
load side Coulomb friction f_{cl}	Nm	0.0018

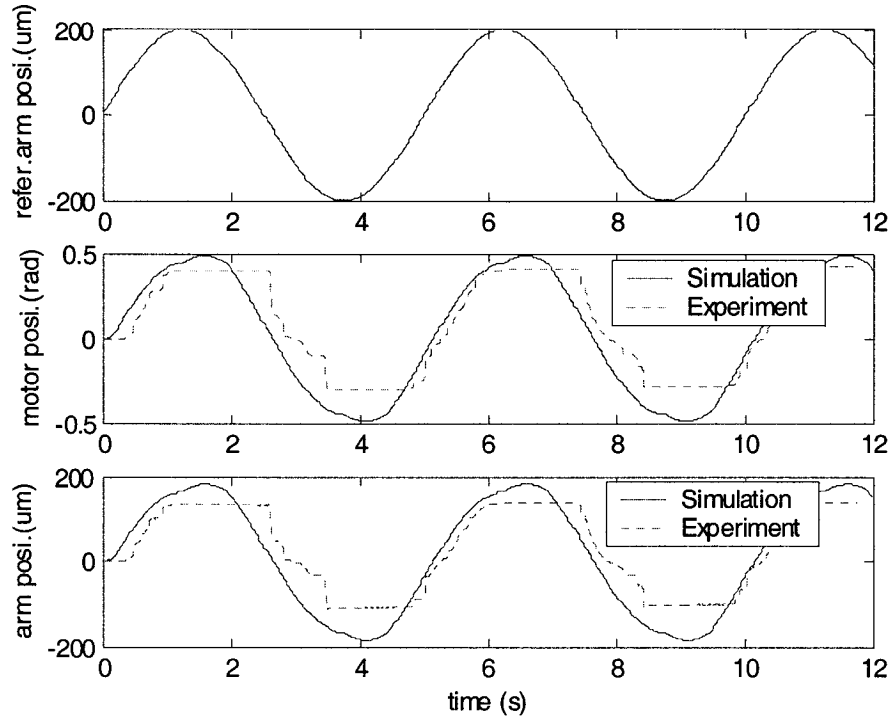

Figure 3-11 Frequency 0.2 Hz

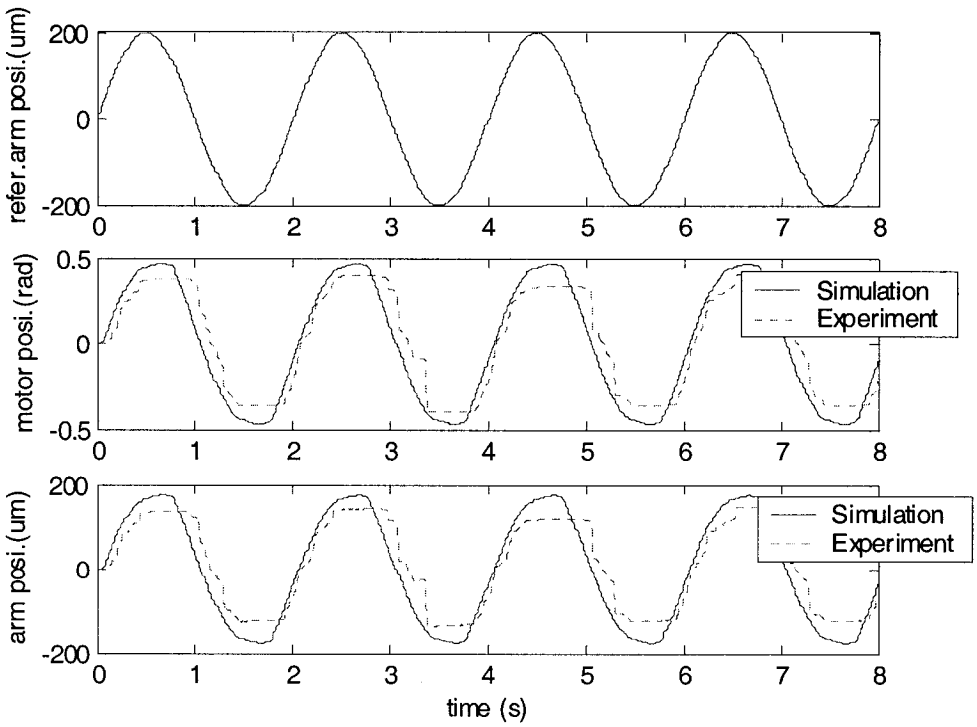

Figure 3-12 Frequency 0.5 Hz

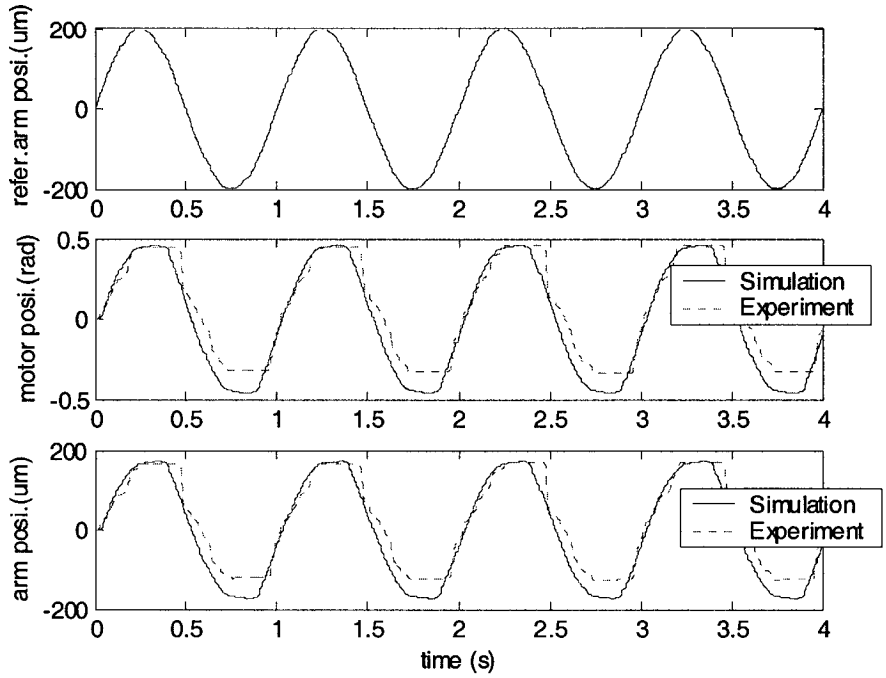

Figure 3-13 Frequency 1 Hz

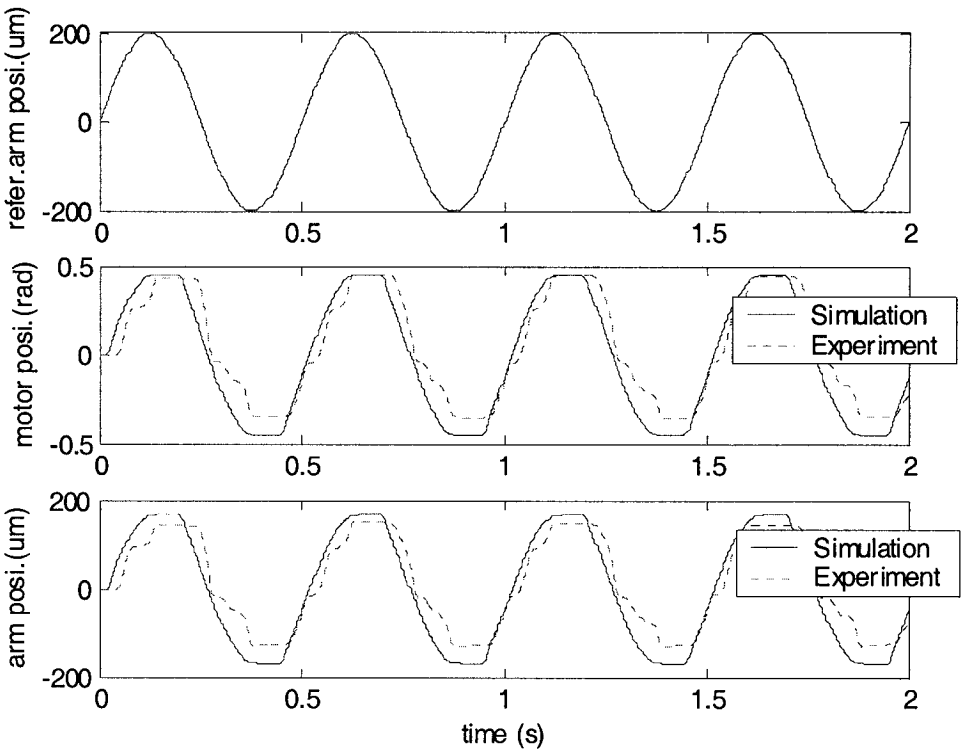

Figure 3-14 Frequency 2 Hz

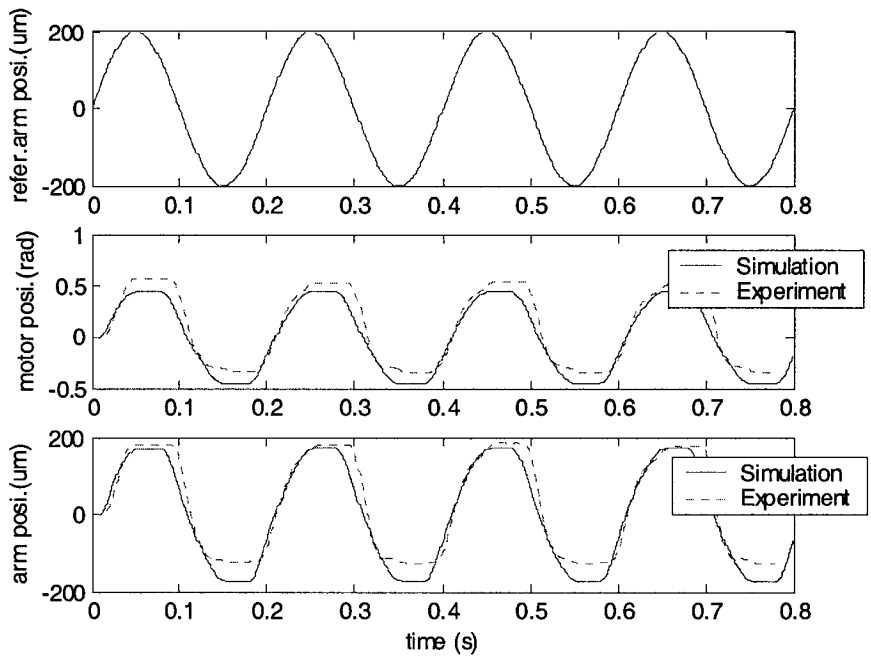

Figure 3-15 Frequency 5 Hz

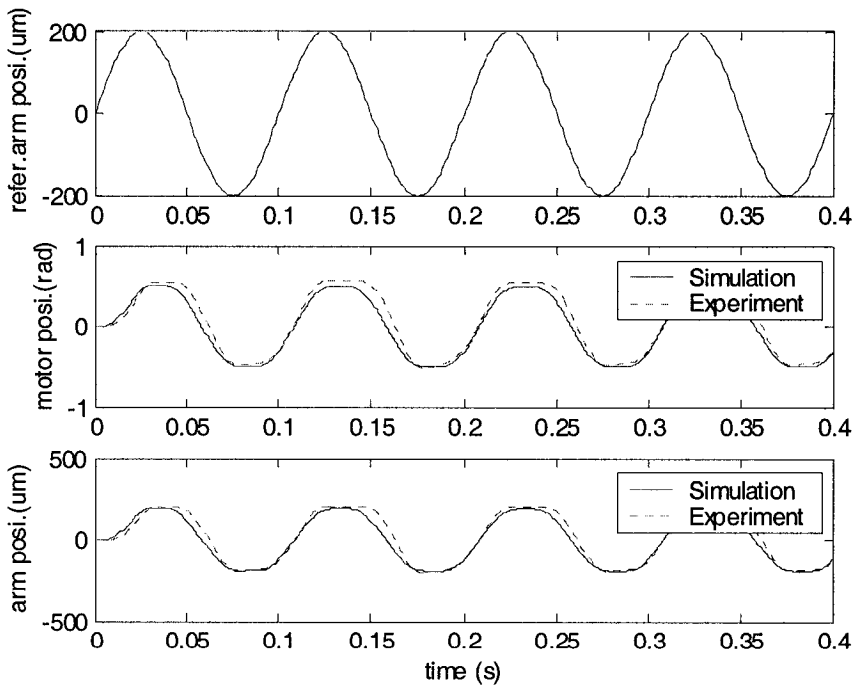

Figure 3-16 Frequency 10 Hz

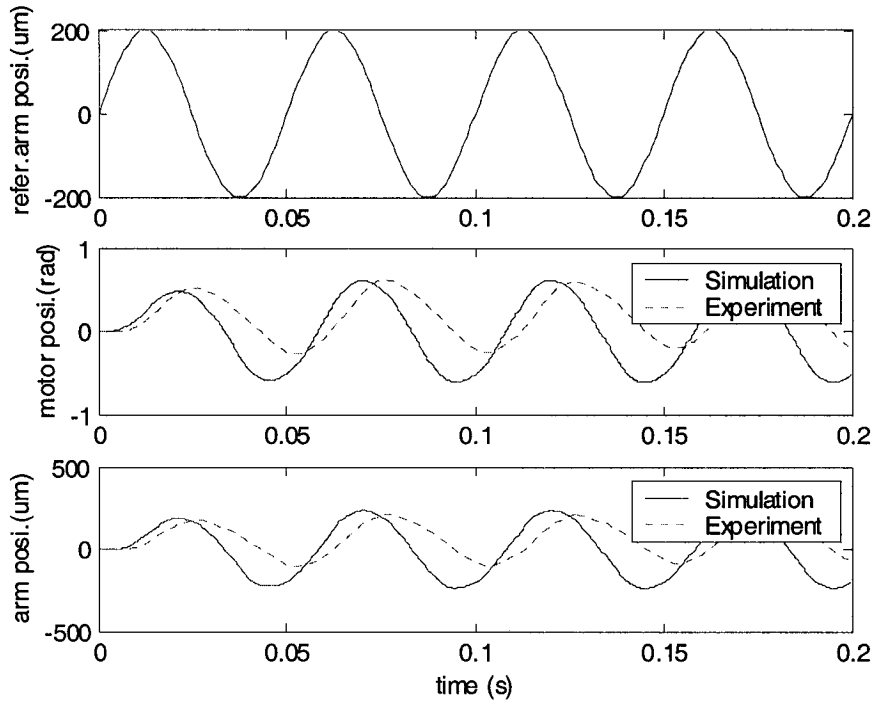

Figure 3-17 Frequency 20 Hz

3.2 Parameter variation and uncertainty

In section 2.3, the motor side friction is measured. Different from other mechanisms, the friction in the harmonic drive varies dramatically with the position. The instant friction at some sampling times may reach 0.14 Nm, while others go down to 0.02 Nm. This variation in friction makes the experimental results not always consistent for different times.

When the Coulomb friction is measured in Chapter 2, a fixed start point is needed. Because sensor noise and measurement error exist, the start point is not always exactly the same every time. The friction variation with position can be regarded as the

existence of asperities on relative moving surfaces in harmonic drives. Even 1 um error in a fixed start point may result in quite different experimental data. Although the friction has been measured in detail, it seems that the friction in the harmonic drive in some designated positions is still an uncertainty. Consequently, in this project, we try to keep the start point as accurate as possible and the experimental data is averaged from several measurements.

In a precision control system, the friction has significant effects on positioning. The quantity of friction must be modelled and identified as accurately as possible so that the friction compensation can be implemented. Since the discipline of friction is still active and the principles of friction are still not very clearly revealed, it is hard to compensate for friction accurately here. When conventional linear control techniques are applied to high friction systems, the system sticks before the desired position is reached resulting in a steady state error. Increasing control parameter gains often does not help beyond a certain point due to the instability that arises. An alternative solution is to apply a large control input for a very short period of time to achieve small motion increments (Figure 3-17). This is known as the impulse control approach. This approach has received more and more attention in recent literatures about precision control [1][18][20][32]. This approach will be used to control the manipulator in the following chapters.

3.3 Parameter validation

In order to position the arm using an impulse control approach for the next two chapters, parameters previously identified are validated using an open-loop pulse simulation and experimental response. Two pulse shapes are used here: square pulse

and first harmonic pulse. The stick-slip phenomenon is also simulated.

3.3.1 Square pulse

In order to overcome the static friction, a square pulse amplitude is fixed in four times of static friction; h=4Vs. Vs is the voltage required to overcome static friction. The pulse shape is shown in Figure 3-18. When the pulse width is W=1ms, the open loop simulation and experimental response to the square pulse are shown in Figure 3-19 and Figure 3-20. Though the arm shows some vibrations during the experiment, it is apparent that the simulation is consistent with the experiment.

3.3.2 First harmonic pulse

We use the first harmonic pulse and set the pulse width to W=1ms:

$$V = h_1 \sin(\pi t/W) \qquad (3\text{-}2)$$

where h_1 is the amplitude. Let h_1 be equal to four times the static friction: h_1=4Vs. The pulse shape is shown in Figure 3-21, the open loop simulation response is shown in Figure 3-22 and the open-loop experimental response is shown in Figure 3-23.

From the simulation and experimental response, it is clear that the model and parameters express the real system very well.

3.3.3 Stick-slip simulation

Since there exists flexibility and load side friction in harmonic drives, when the

motor side moves slowly, the load side will only move when the spring force has accumulated enough to overcome the load side friction. This will result in a stick-slip phenomenon in the arm motion.

We choose an input voltage that can just overcome the static friction. The simulated motor and arm position are shown in Figure 3-24. A stick-slip phenomenon can be observed in the arm's motion.

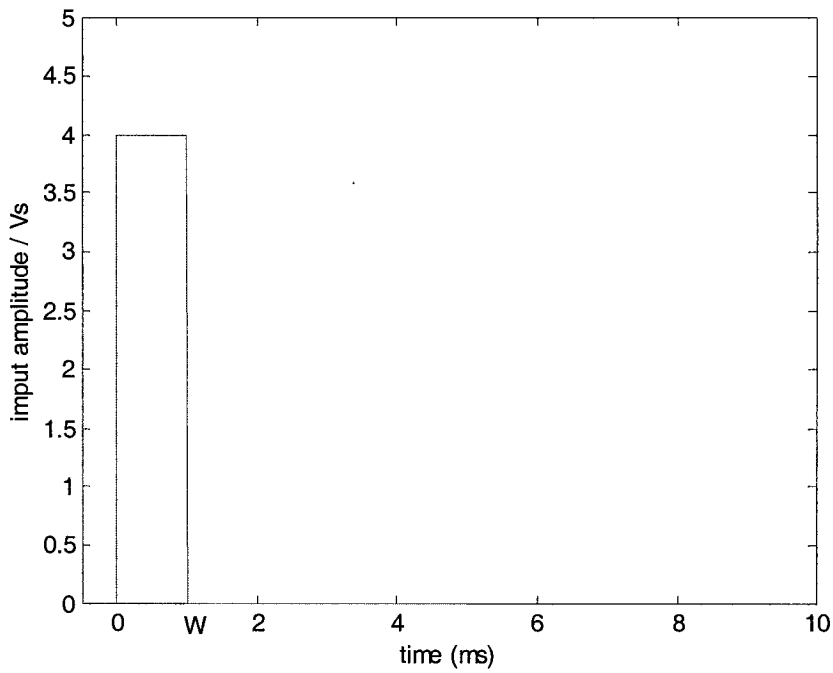

Figure 3-18 Square pulse shape

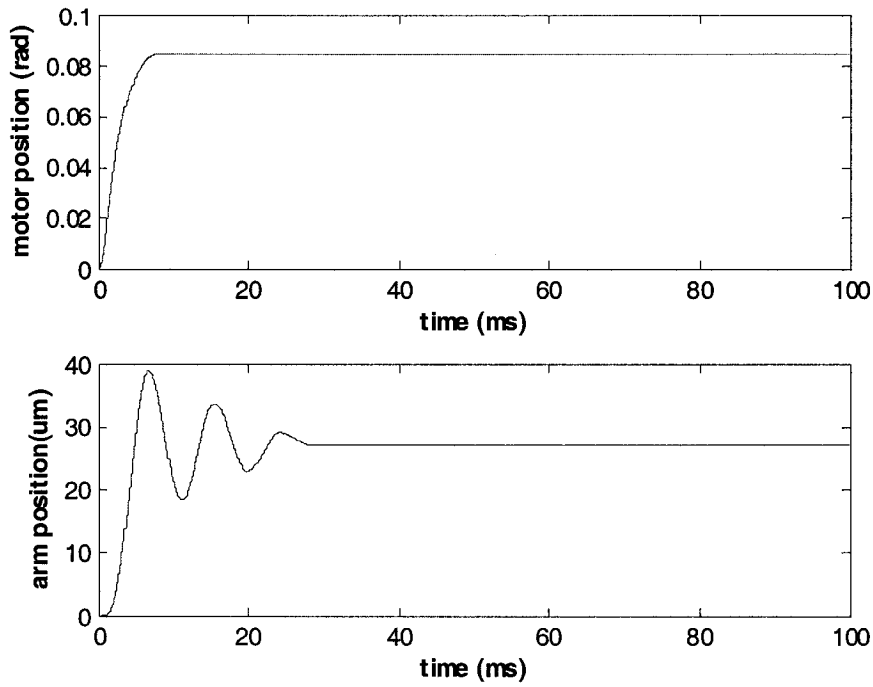

Figure 3-19 Square pulse simulation response

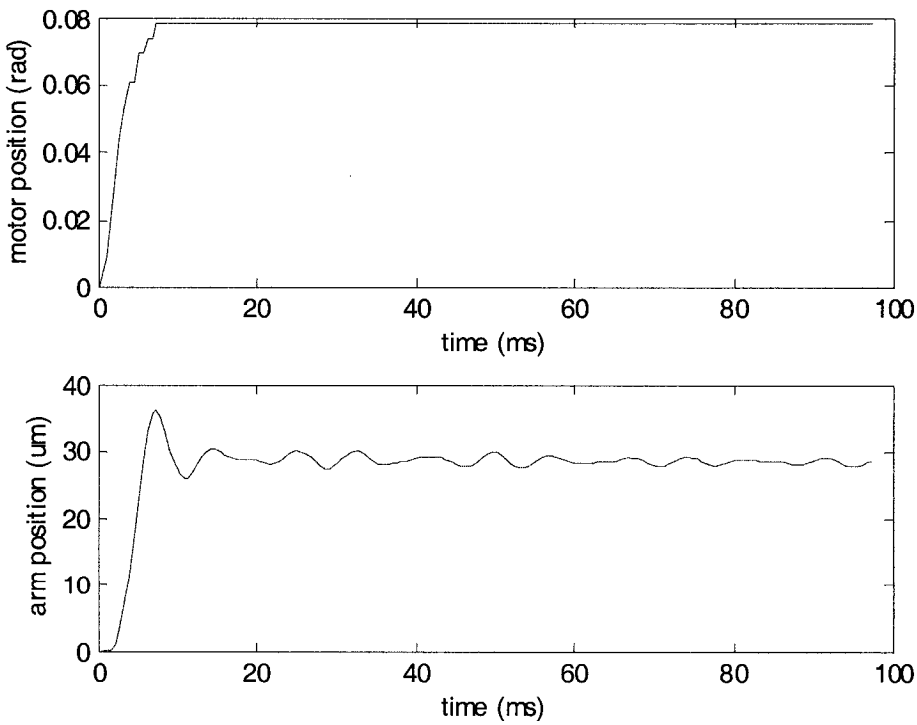

Figure 3-20 Square pulse experimental response

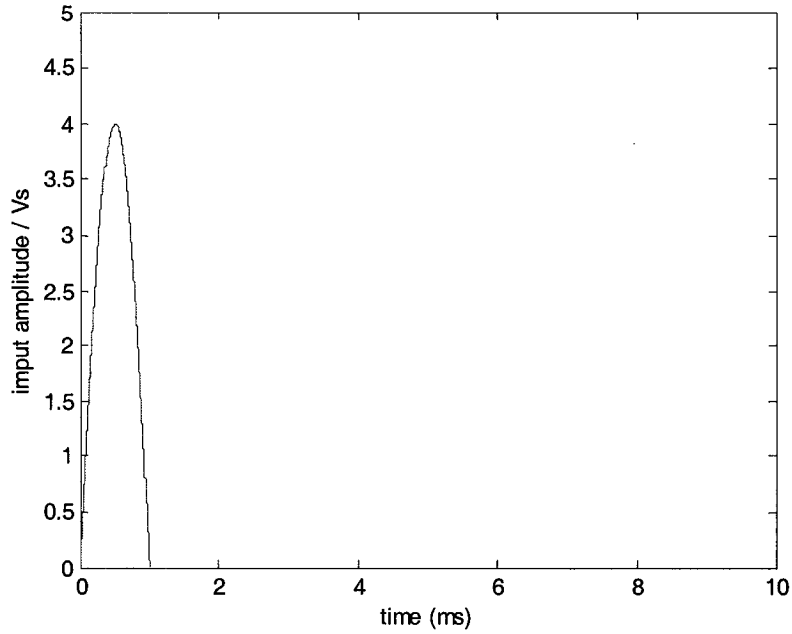

Figure 3-21 First harmonic pulse shape

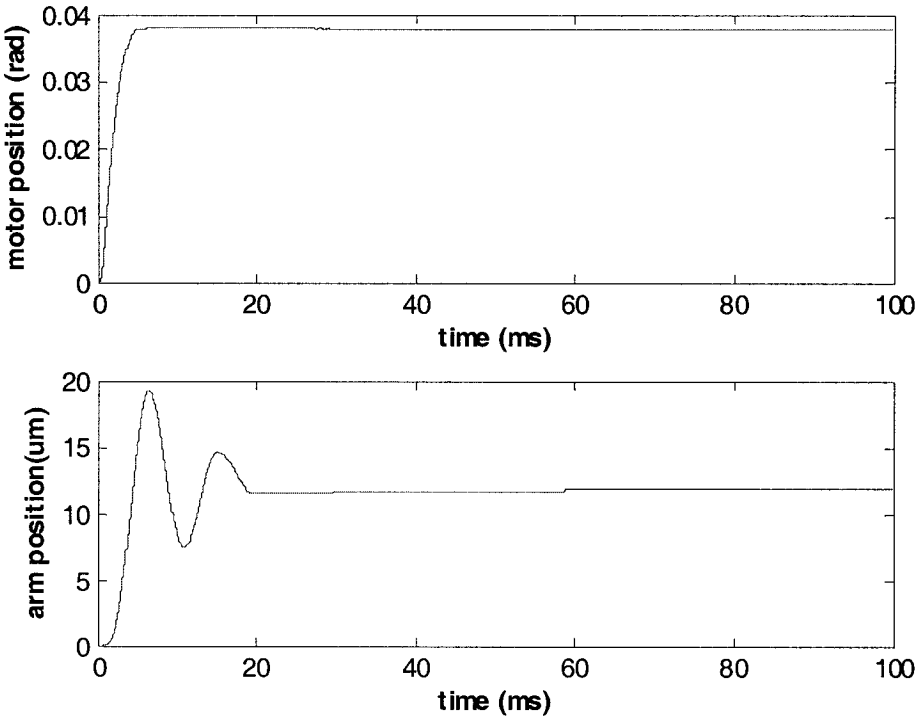

Figure 3-22 First harmonic pulse simulation response

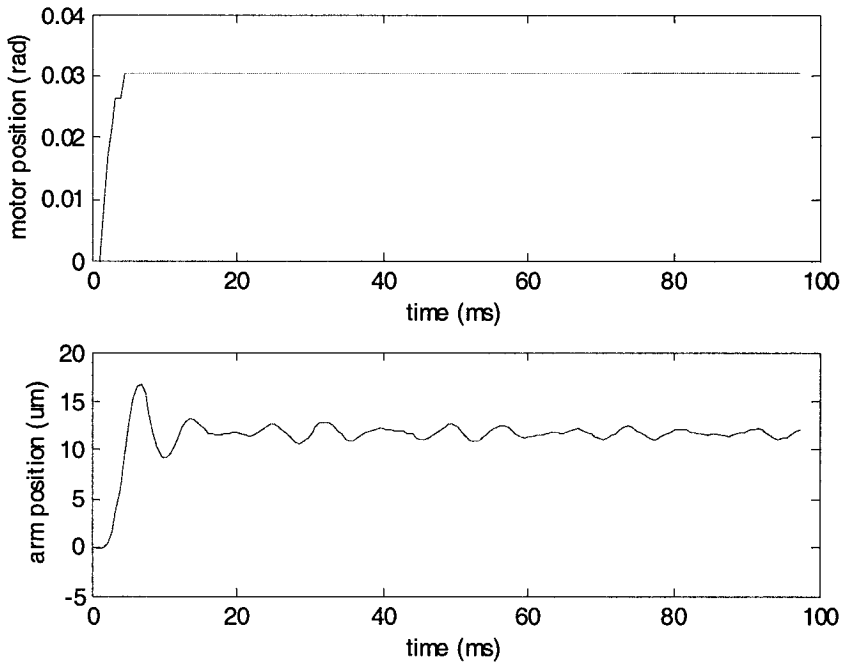

Figure 3-23 First harmonic pulse experimental response

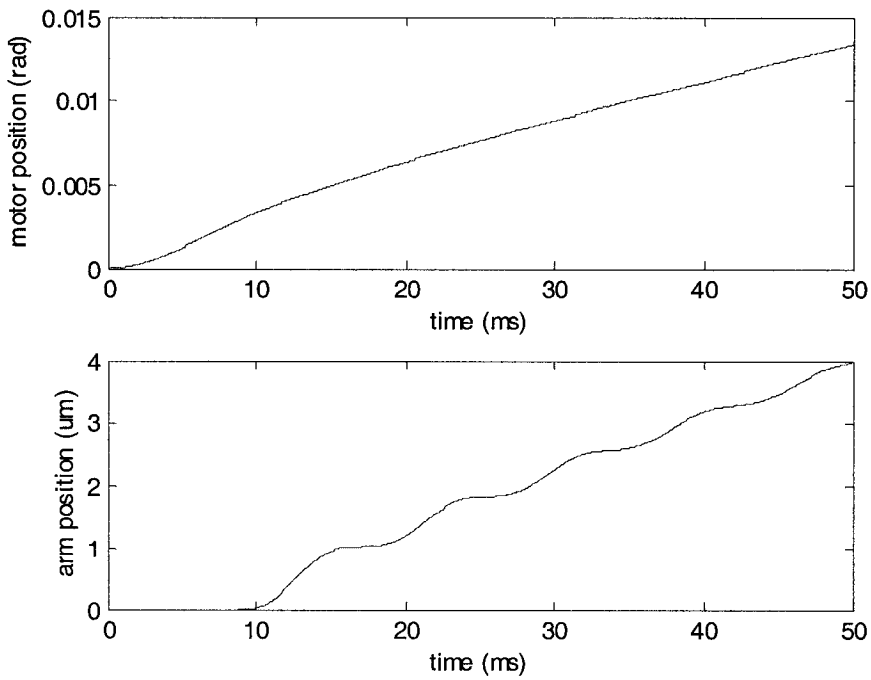

Figure 3-24 Stick-slip phenomenon simulation

Chapter 4 Impulse Control

In order to control the manipulator precisely in the presence of a high friction level, the impulse control method is applied in this chapter. First, the simulation and experimental impulse responses are determined. Then, an impulse feedback controller is developed. Finally, the resolution of the system for the conventional linear control and impulse control is investigated.

4.1 Previous work

A number of researchers have devised impulse controllers that achieve precise positioning in the presence of friction [1][18][20][32]. By making an impulse of a large magnitude but of a short duration, the static friction is overcome and sensitivity to the details of friction is reduced. Hojjat and Higuchi [20] presented an apparatus especially designed to demonstrate impulse control. They reliably achieved a remarkable 10nm per impulse motion and speculate that a repeatable 1nm per impulse motion may be possible. They controlled the amplitude of the impulses, typically applying a force of about 10 times the static friction for about 1ms, and show that displacement is given by the square of the amplitude times an empirical constant.

Armstrong and Armstrong-Helouvry [20] demonstrated an impulse controller on a PUMA robot. Their objective was to achieve a very high precision force control needed to manipulate an object with a crushing strength of only $1/60^{th}$ the level of static friction

in the mechanism. Using a calibrated table of impulse magnitude and duration, Armstrong-Helouvry (1991) applied impulses that are only 10-20% bigger in magnitude than the static friction and achieved 10 micro-radians per impulse motions of the industrial manipulator.

M.R.Popovic, D.M.Gorinevsky and A.A.Goldenberg [18] (2000) tested the displacement for the impulses with different pulse amplitudes and different durations, and then designed an impulse controller based on their experimental results. An innovative feature of the controller is that the pulse amplitude and duration generated by the controller are computed using a fuzzy logic approximation of the dependence between the desired displacement and the pulse shape. The controller is able to achieve positioning precision close to the limits of position encoder resolution (less than 0.4 um).

The above impulse controllers use a square pulse shape as impulse input. They have in common the use of a long sampling interval. Underlying these impulse controllers is the requirement that the system be in the stuck condition when each impulse is applied. The method is, in essence, a small bang followed by an open-loop slide. Returning to the stuck condition imposes a number of limitations, but improves the predictability of response to the impulse. To reduce the sampling interval, Brandon W. Gordon (1995) [1] used a generalized impulse shape consisting of the first two harmonics of a general series expansion with fixed endpoints. That is,

$$u(t)= h_1 \sin(\pi \frac{t}{W}) + h_2 \sin(2\pi \frac{t}{W}) \qquad 0 \le t \le W \qquad (4\text{-}1)$$

The proposed controller can achieve a resolution of 0.2 um using a sampling rate of 250 ms.

Yang and Tomizuka [32] presented a variable structure controller in 1988. A

standard linear controller operates away from zero velocity. At or near zero velocity, the adaptive impulse controller takes over. Because of the existence of the parameter uncertainty, mainly friction uncertainty, the corresponding displacement (delta) of the controlled object to the duration of the square pulse is a non-predictable parabolic curve. The parameter of the parabolic curve is estimated online. Then, the impulse is tuned by varying the impulse duration (width), selected to achieve the desired displacement. They chose a force of about 4 times the level of static friction. This adaptive impulse control algorithm can achieve the control objective effectively. The authors also presented a rigorous demonstration of the stability of both their controller and the adaptive element. This variable structure controller exploits the capability of impulse control better.

In the following sections of this chapter, the experimental response based on a pulse shape of the equation (4-1) is tested for h_1 and h_2. Then an impulse controller is devised. The resolutions for conventional linear controller and impulse controller are tested. In next chapter an adaptive impulse control will be presented.

4.2 Physics of impulse: momentum, motion and energy

4.2.1 Motion and momentum of the motor inertia

The harmonic drive model in Figure 2-7 can be simplified as illustrated by Figure 4-1. Assume the motor input voltage is,

$$u(t) = h_1 \sin(\pi t / W) \qquad (4\text{-}2)$$

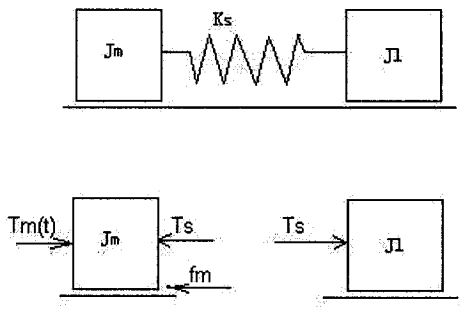

Figure 4-1 Harmonic drive model

where h_1 is the voltage amplitude, and W is the pulse width. For simplicity, assume that the motor torque is proportional to the input voltage:

$$T_m(t) = \frac{K_m}{R}u(t) = \frac{K_m h_1}{R}\sin(\pi t / W) = p\sin(\pi t / W) \tag{4-3}$$

$$p = \frac{K_m h_1}{R} \tag{4-4}$$

The motor torque pulse is shown in Figure 4-2.

Because load side friction is much smaller than motor side friction, it is reasonable to assume that the spring torque T_s

$T_s << f_m$ and $T_s << T_m(t)$

f_m is motor side friction. In the period $0 \le t \le W$, we use Newton's second law:

$$J_m\dot{\omega}_m = T_m(t) - f_m \tag{4-5}$$

$$\omega_m = \frac{1}{J_m}\int_0^t (T_m(\sigma) - f_m)d\sigma \tag{4-6}$$

The substitution of (4-3) into (4-6) yields

$$\omega_m = \frac{pW}{J_m\pi}(1 - \cos\frac{\pi t}{W}) - \frac{f_m}{J_m}t \tag{4-7}$$

The momentum of the pulse is:

$$m = \int_0^t T_m(\sigma)d\sigma = \frac{pW}{\pi}(1-\cos\frac{\pi t}{W}) \qquad (4\text{-}8)$$

From (4-7), it is apparent that the momentum is converted into two parts. The first part is the motor inertia momentum $J_m\omega_m$ that drives the motor inertia motion. The motion of motor inertia will accumulate potential energy in the spring and the load inertia will be driven by the potential energy in turn. The second part of the pulse momentum is consumed by friction. The momentum of the pulse is:

$$m = J_m\omega_m + f_m t \qquad (4\text{-}9)$$

Motor position can be obtained from (4-7):

$$q_m = \int_0^t \omega_m(\sigma)d\sigma = \frac{pW}{J_m\pi}(t - \frac{W}{\pi}\sin(\frac{\pi t}{W})) - \frac{f_m}{2J_m}t^2 \qquad (4\text{-}10)$$

It is evident that when t=W, the motor velocity obtains its maximal value. At t=W, the motor velocity and position are:

$$V_{mw} = \frac{2pW}{J_m\pi} - \frac{f_m W}{J_m} \qquad (4\text{-}11)$$

$$q_{mw} = \frac{pW^2}{J_m\pi} - \frac{f_m W^2}{2J_m} \qquad (4\text{-}12)$$

Assume the motor stops at time t_f, as shown in Figure 4-4. When $W \le t \le t_f$,

$$J_m\dot{\omega}_m = -f_m \qquad (4\text{-}13)$$

The motor velocity and position can be obtained by the integral:

$$\omega_m = -\frac{f_m}{J_m}t + C_1 \qquad (4\text{-}14)$$

$$q_m = -\frac{f_m}{2J_m}t^2 + C_1 t + C_0 \qquad (4\text{-}15)$$

The position response and velocity response are shown in Figure 4-3 and Figure 4-4. At t=W, $\omega_m = V_{mw}$ and $q_m = q_{mw}$. Then the constant C_0 and C_1 can be calculated;

$$C_0 = -\frac{pW^2}{J_m \pi}$$

$$C_1 = \frac{2pW}{J_m \pi}$$

The substitution of C_0 and C_1 into (4-14) and (4-15) yields:

$$\omega_m = -\frac{f_m}{J_m}t + \frac{2pW}{J_m \pi} \qquad (4\text{-}16)$$

$$q_m = -\frac{f_m}{2J_m}t^2 + \frac{2pW}{J_m \pi}t - \frac{pW^2}{J_m \pi} \qquad (4\text{-}17)$$

The motor position and velocity are shown in Figure 4-3 and Figure 4-4.

4.2.2 Motion of the load inertia

The load inertia is driven by the spring torque. We use Newton's second law:

$$J_l \dot{\omega}_l = K_s(rq_m - q_l) - f_l \qquad (4\text{-}18)$$

r is the harmonic drive gear ratio, f_l is load side friction. If we define

$$\begin{bmatrix} x_1 \\ x_2 \end{bmatrix} = \begin{bmatrix} q_l \\ \dot{q}_l \end{bmatrix} \qquad (4\text{-}19)$$

(4-18) can be expressed as the following state equation:

$$\begin{bmatrix} \dot{x}_1 \\ \dot{x}_2 \end{bmatrix} = \begin{bmatrix} x_2 \\ \frac{1}{J_l}(K_s(rq_m - x_1) - f_l) \end{bmatrix} \tag{4-20}$$

4.2.3 System energy

Energy is conservative in any system. When a pulse is applied to the system, the work done by the pulse is converted to the motor inertia kinetic energy and the spring potential energy. When potential energy has accumulated to a certain amount, it will be converted into load inertia kinetic energy. Therefore, the arm will move a certain displacement (delta).

System potential energy:

$$E_p = \frac{1}{2}K_s(rq_m - q_l)^2 \tag{4-21}$$

System kinetic energy:

$$E_k = \frac{1}{2}J_m\omega_m^2 + \frac{1}{2}J_l\omega_l^2 \tag{4-22}$$

4.2.4 Simulation

Figure 4-3 and Figure 4-4 show that the motor side will get stuck about 6ms after the pulse is applied. Due to the flexibility, the load side will get stuck after 20ms. We apply five pulses to the motor at an interval of 50ms. The input pulses are shown in Figure 4-5. Every pulse shape zoom is shown in Figure 4-2. The motor and load inertia position responses are shown in Figure 4-6 and Figure 4-7. The motor and arm velocity responses are shown in Figure 4-8 and Figure 4-9. The results demonstrate that

the arm moves after the spring deformation has accumulated to a special quantity because of the load side friction.

Since the load side friction is small, the arm moves fast once it starts moving and makes the spring tensional. Then the arm moves back towards the motor and the spring tension becomes small, as shown in Figure 4-7 and Figure 4-9. The spring deformation in Figure 4-12 shows a vibration in the arm. This is verified by the experimental pulse response in Figure 3-20 and Figure 3-23. The motor's kinetic energy is converted into potential energy and then converted into the load kinetic energy, as shown in Figure 4-10 and Figure 4-11. The spring deformation ($rq_m - q_l$) is shown in Figure 4-12.

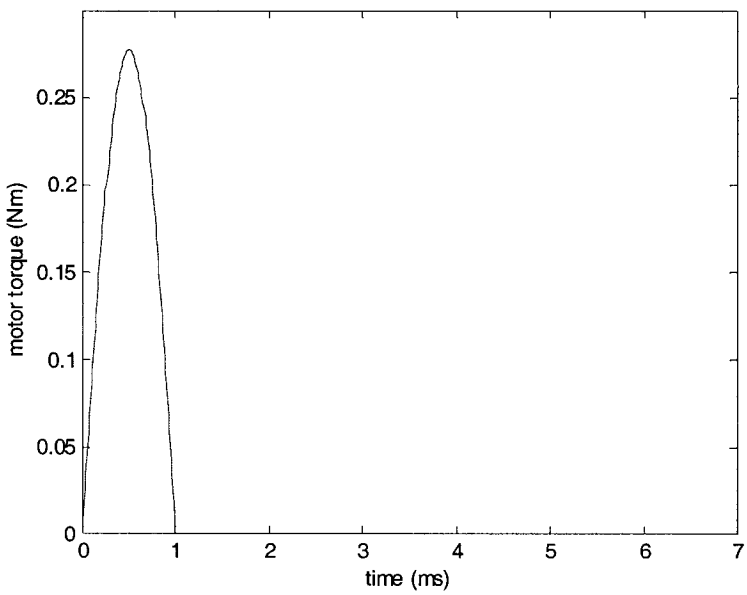

Figure 4-2 Motor torque pulse

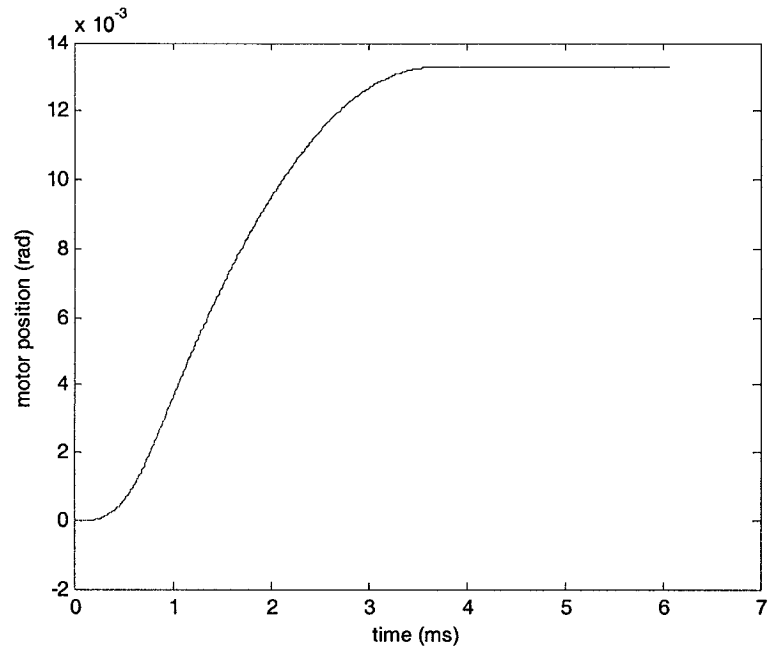

Figure 4-3 Motor position response to the pulse

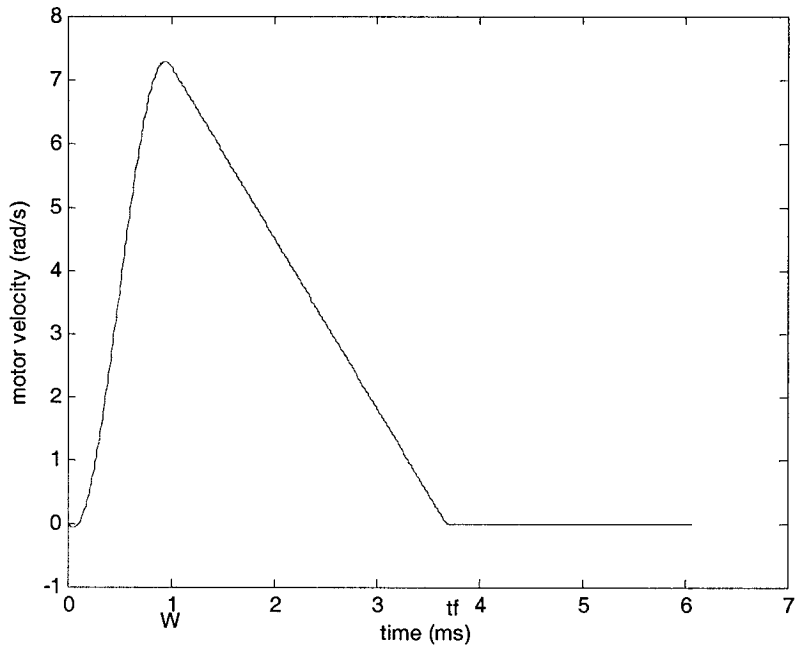

Figure 4-4 Motor velocity response to the pulse

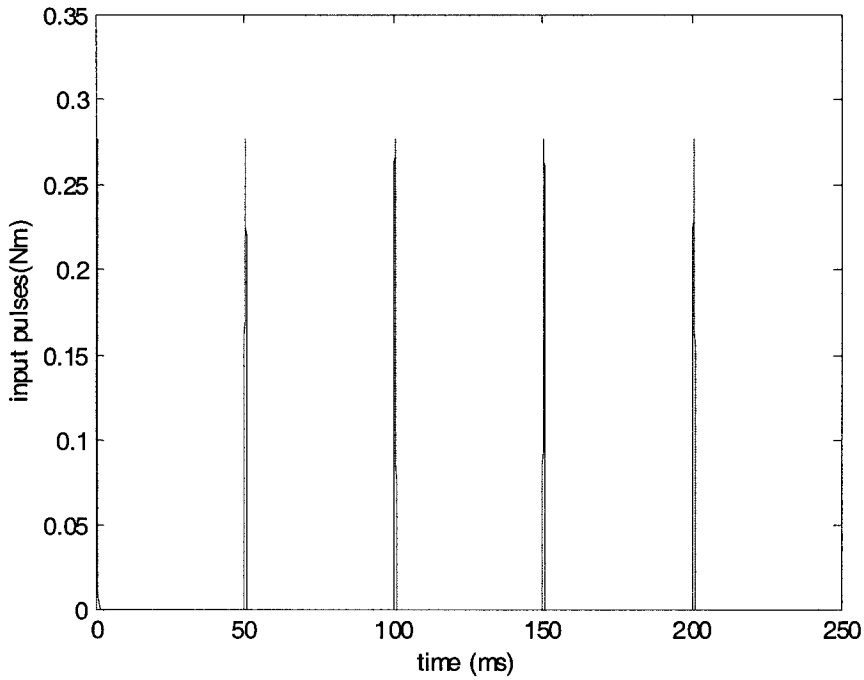

Figure 4-5 Input pulses

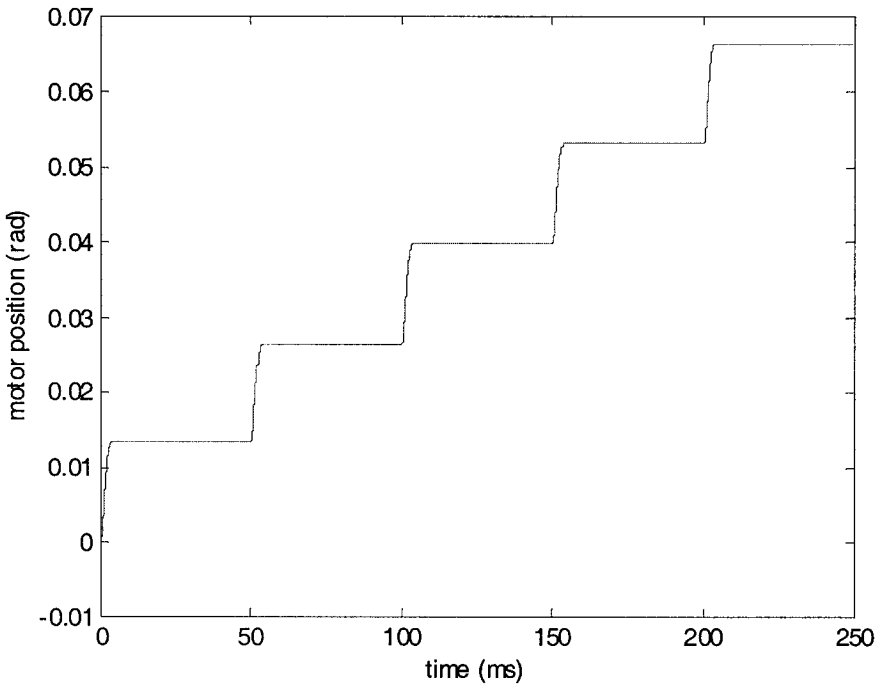

Figure 4-6 Simulation of motor position response to pulses

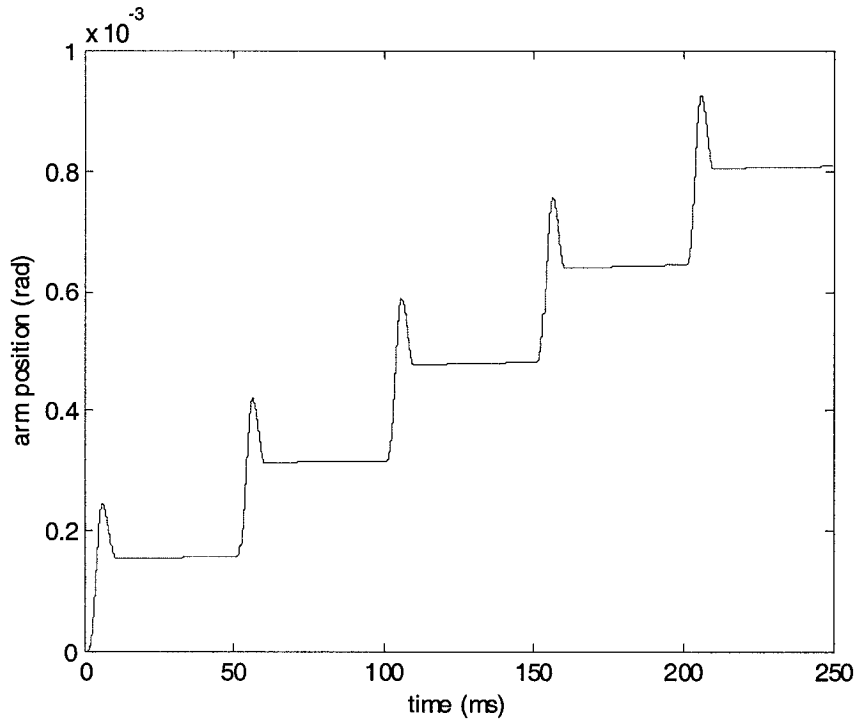

Figure 4-7 Simulation of arm position response to pulses

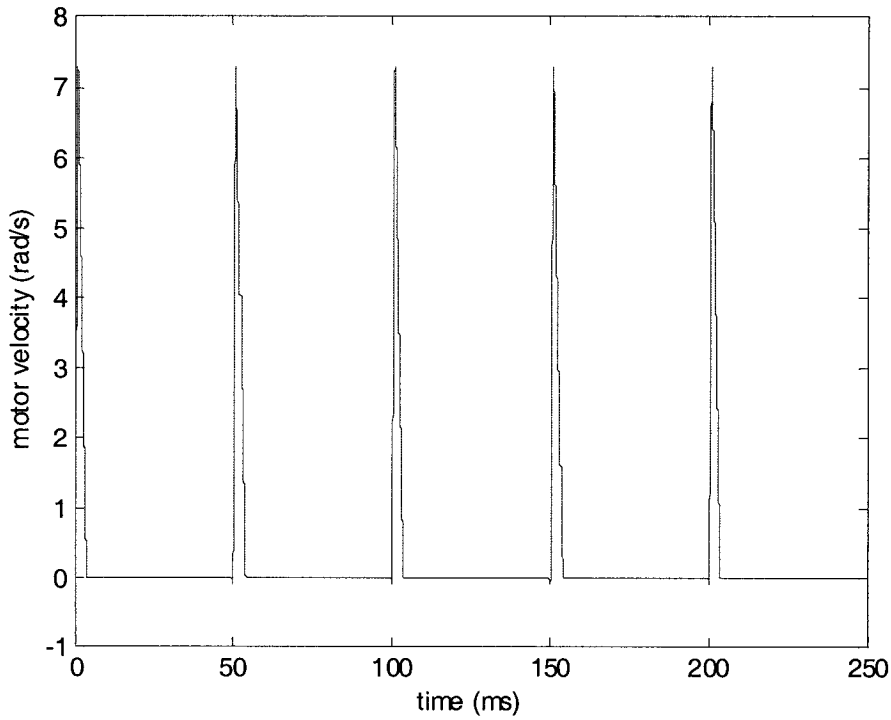

Figure 4-8 Simulation of motor velocity response to pulses

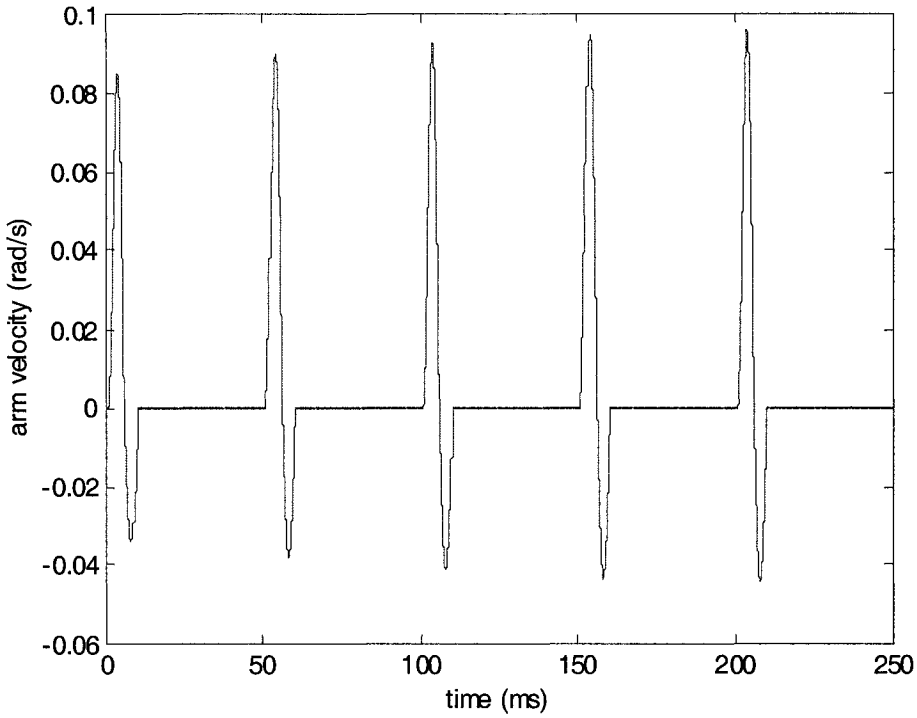

Figure 4-9 Simulation of arm velocity response to pulses

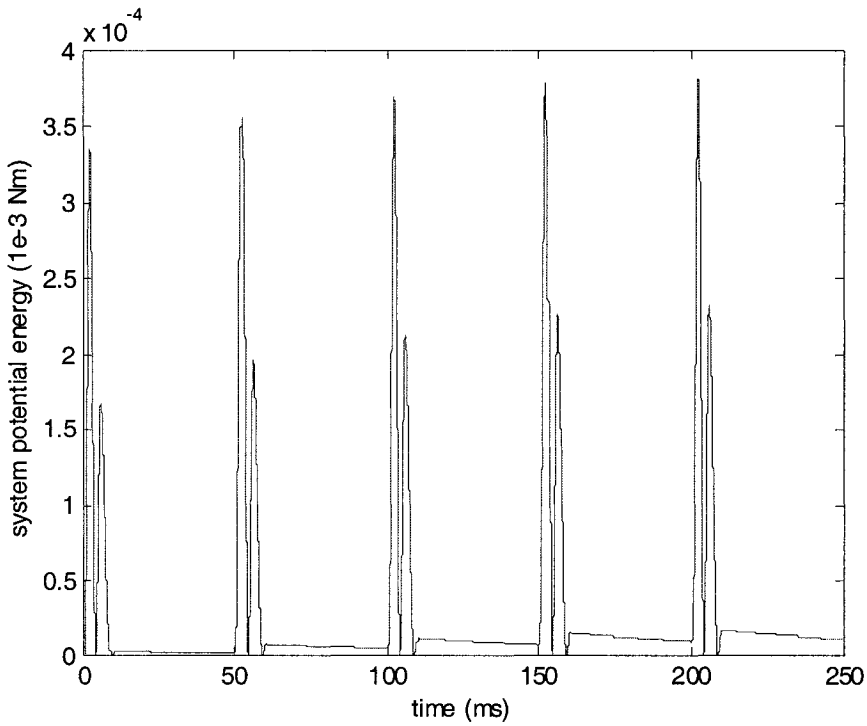

Figure 4-10 System's potential energy

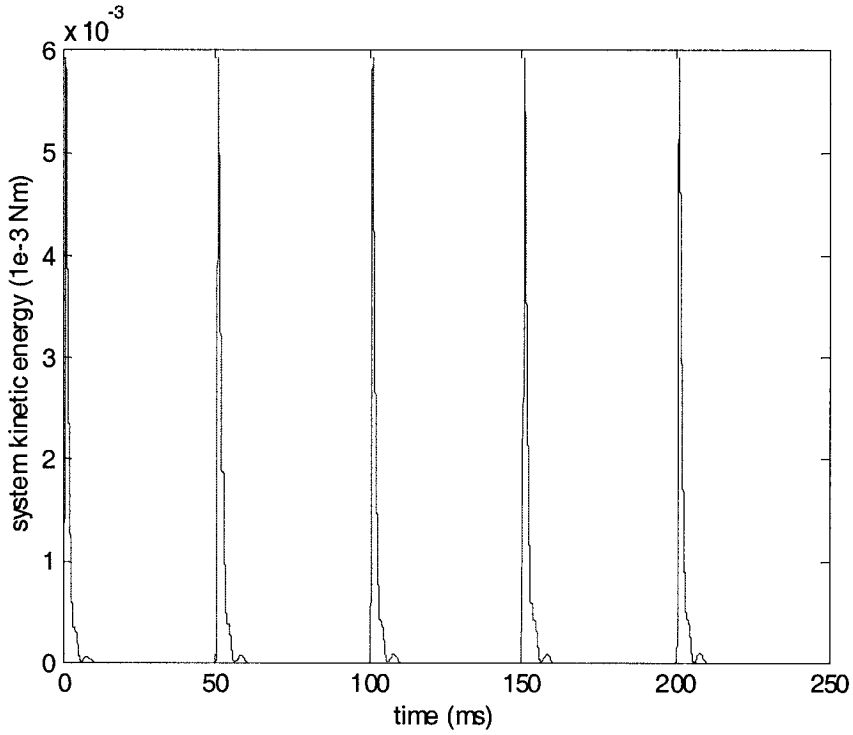

Figure 4-11 System's kinetic energy

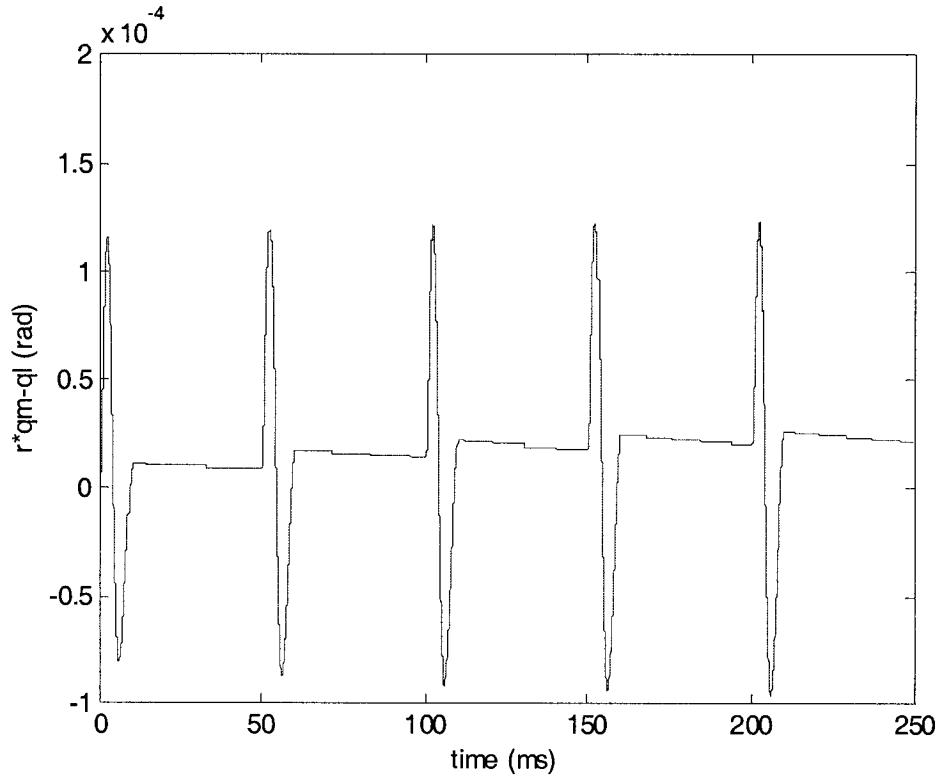

Figure 4-12 Spring deformation $rq_m - q_l$

4.3 Impulse response

Use the pulse shape with the form of equation (4-1):

$$u(t)= h_1 \sin(\pi \frac{t}{W}) + h_2 \sin(2\pi \frac{t}{W}) \qquad 0 \le t \le W$$

Where h_1 and h_2 are variable coefficients, and W is the pulse width. In this pulse shape, the first harmonic is the main pulse to drive the arm to move a displacement. The second harmonic has two functions: it enforces the main harmonic pulse in its first half that will help it to eliminate the dead zone (see Figure 4-17 and Figure 4-18), and it provides a minus pulse in its second half to stop the arm motion quickly. Set h_1= 4V, h_2=7.5V, and W = 1ms; the pulse input read from the oscilloscope is shown in Figure 4-13. The pulse voltage across the 1 Ω resistor is also shown in Figure 4-13. The motor position and arm position in the simulation and experiment are shown in Figure 4-14 and Figure 4-15. It is apparent that most of the motor motion occurs during the 3 ms, and most of the arm motion occurs during 20 ms. The simulations of motor and arm velocity are shown in Figure 4-16. The arm has some vibration due to the flexibility in the harmonic drive.

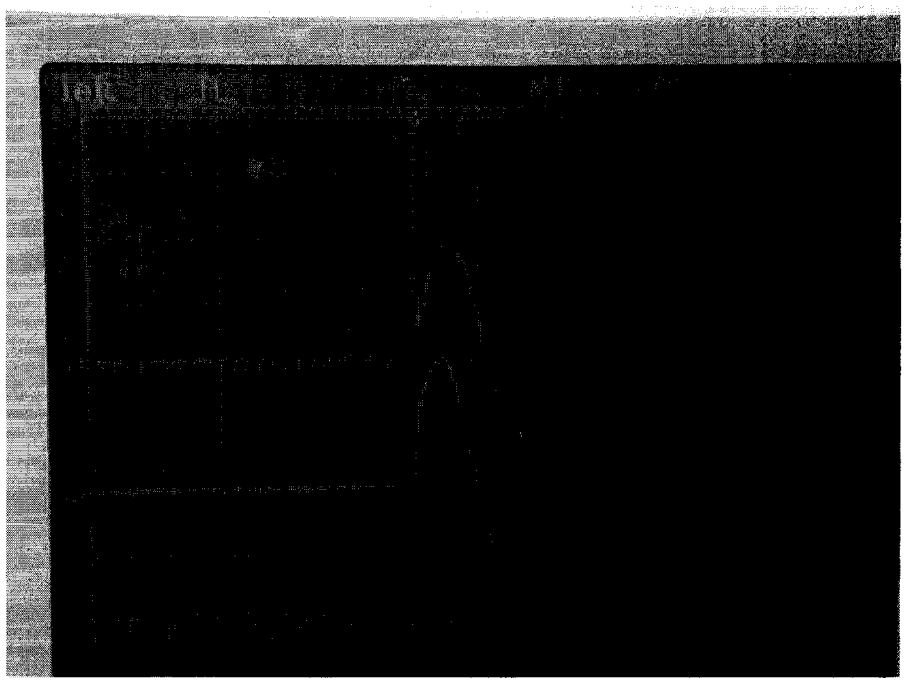

Figure 4-13 Input pulse and corresponding pulse across 1 Ω resistor

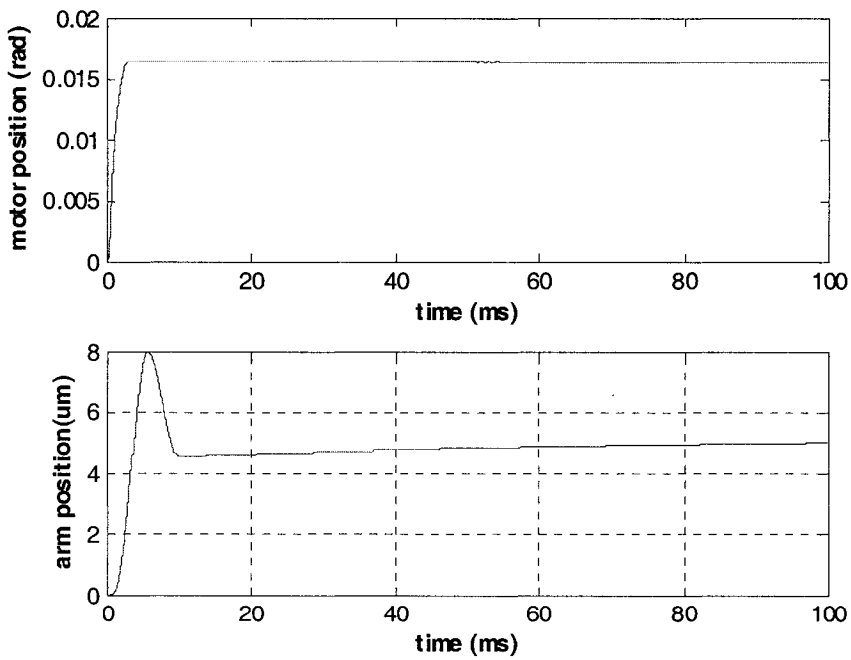

Figure 4-14 Simulation of pulse position response ($h_1 = 4\text{V}, h_2 = 7.5\text{V}$)

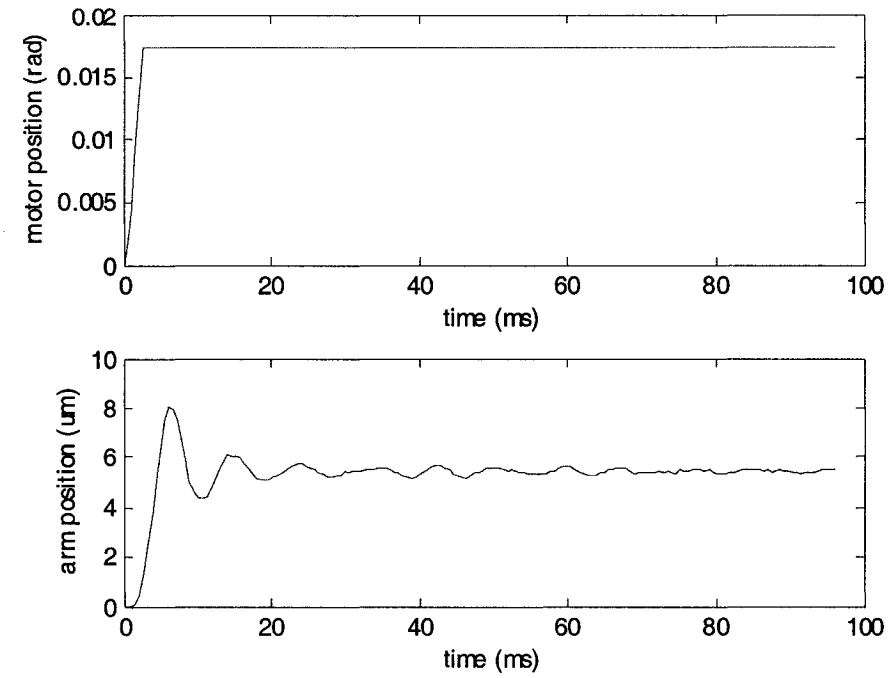

Figure 4-15 Experiment of pulse position response ($h_1 = 4\text{V}, h_2 = 7.5\text{V}$)

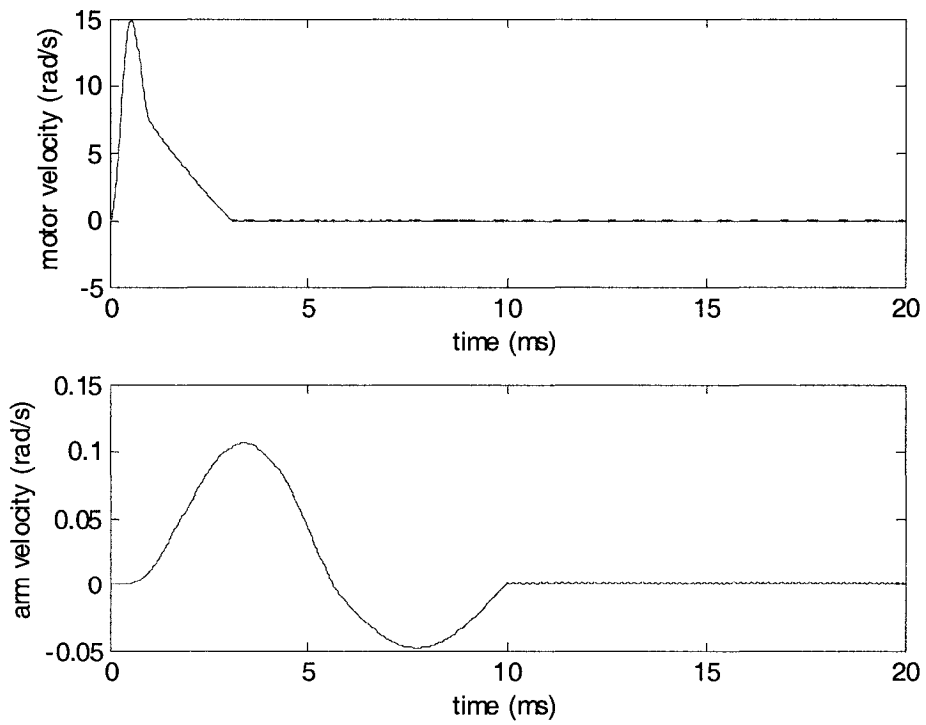

Figure 4-16 Simulation of impulse velocity response ($h_1 = 4\text{V}, h_2 = 7.5\text{V}$)

In general, the displacement (delta) of the arm due to a pulse is a function of h_1, h_2 and W. It is desirable to have W as short as possible to provide insensitivity to friction parameter uncertainty, but in practice, the system bandwidth limitation, amplifier saturation, and unwanted excitation of mechanical vibrations tends to limit the input frequency. For this investigation, W is set equal to 1ms to simplify analysis. This value seems to provide good control performance.

The input voltage to the motor is about Vs=1.8V in order to overcome the static friction. The values of h_1 and h_2 are divided by Vs to set them as non-dimensional quantities. The simulated arm displacement (delta) versus h_1/Vs and h_2/Vs is shown in Figure 4-17. The experimental arm displacement versus h_1/Vs and h_2/Vs is shown in Figure 4-18. Note that the experimentally obtained data in Figure 4-18 may have some local deviations that are caused by the random parameter variations such as friction uncertainty. For each pulse shape, the result shown in Figure 4-18 is the average of five experiments.

It is apparent that the system moves forward only when h_1 is bigger than some threshold. In other words, there is a dead zone in respect to h_1. The size of this dead zone can be decreased by increasing h_2. The dead zone is undesirable for control system design, so h_2/Vs will be chosen to eliminate the dead zone. This occurs when h_2/Vs=3.1278 in simulation and h_2/Vs=3.2 in experiment.

The friction is symmetrical when motor motion reverses. When implementing the controller, if the error between the desired position and current position is positive, we choose h_2/Vs= 3.1278 in the simulation and h_2/Vs= 3.2 in the experiment; if the error is

negative, we choose h_2/Vs= -3.1278 in the simulation and h_2/Vs= -3.2 in the experiment.

The simulated arm displacement varies with h_1/Vs when h_2/vs=3.1278 and is shown in Figure 4-19; the experimental arm displacement varies with h_1/Vs when h_2/vs=3.2 and is shown in Figure 4-20. The curves can be fit approximately by a parabolic function of h_1/Vs:

$$d = b \times (h_1 / Vs)^2 \times \mathrm{sgn}(h_1) \qquad (4\text{-}23)$$

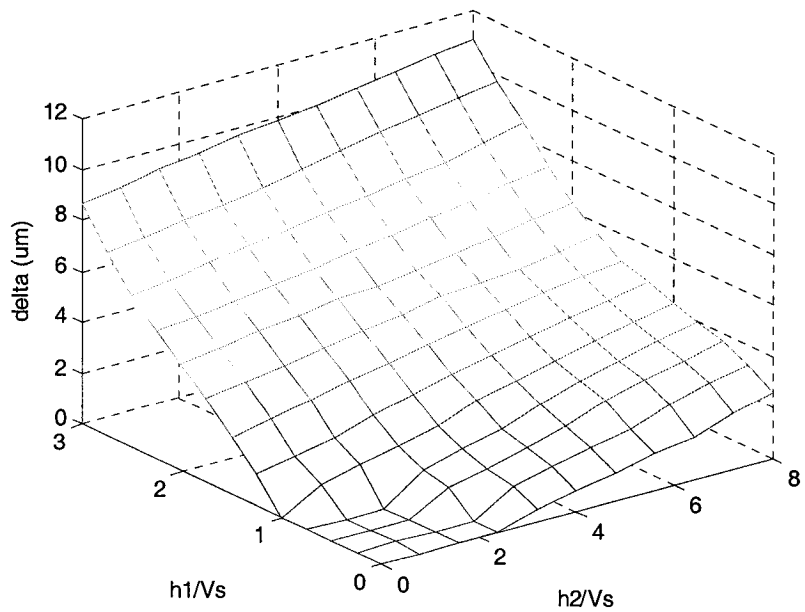

Figure 4-17 Generalized simulation impulse response

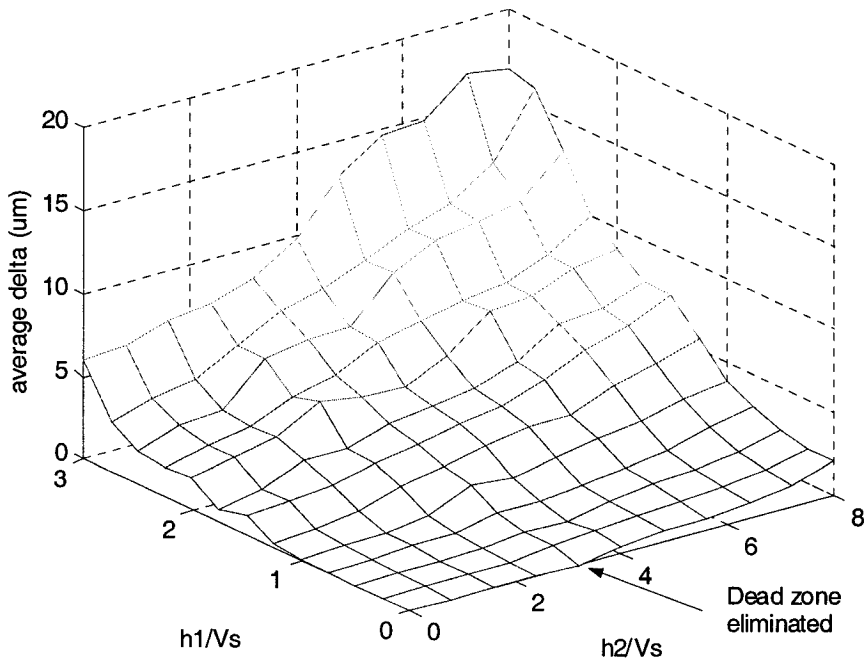

Figure 4-18 Generalized experimental impulse response

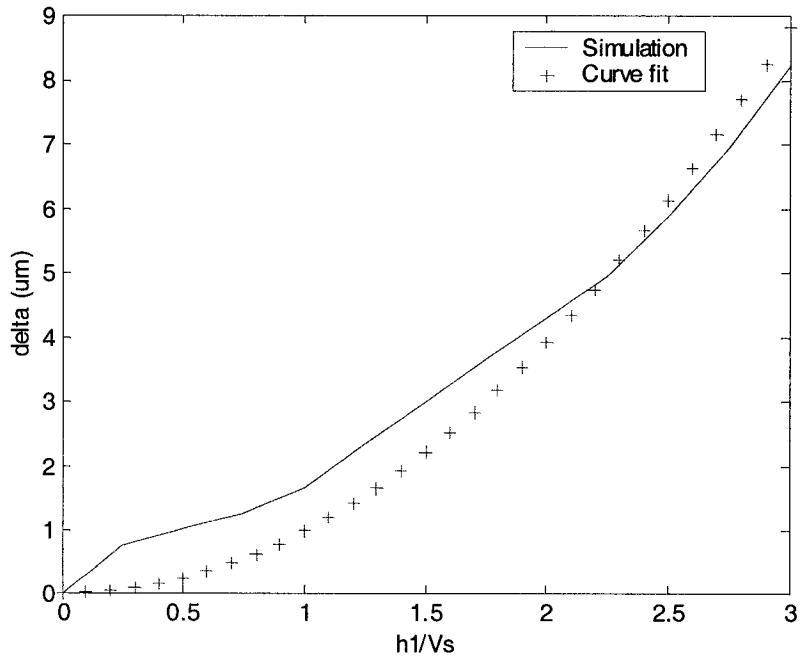

Figure 4-19 Arm displacement (simulation) (h_2/Vs=3.1278)

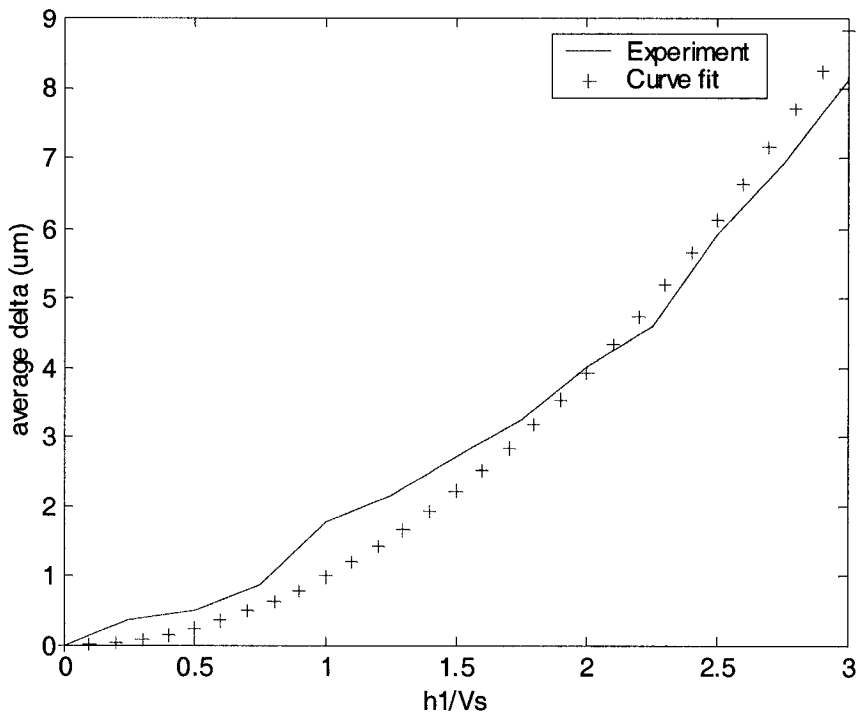

Figure 4-20 Arm displacement (experiment) (h_2/Vs=3.2)

4.4 Impulse feedback control

4.4.1 Controller

In impulse control, the position is the accumulation of the displacements. Hence, the appropriate discrete time state equation is,

$$x(k+1)=x(k)+d(k+1) \qquad (4\text{-}24)$$

Where x(k) and x(k+1) represent the arm position at time t and t+Δt, and d(k+1) is the arm displacement (delta) due to an impulse input at time t. This equation represents a first order difference equation with input d(k+1).

Equation (4-23) can be written as:

$$d(k+1)=bh_1^2\,\mathrm{sgn}(h_1)=bu_p(k) \qquad (4\text{-}25)$$

where

$$u_p(k) = h_1^2 \operatorname{sgn}(h_1) \tag{4-26}$$

d(k+1) can be considered an input variable since for any desired displacement value within a given range, we can calculate the required h_1 with equation (4-26). This technique is dependent on our ability to invert the relationship between d and h_1 which shows why a dead zone is highly undesirable in the system response as it makes the relationship difficult to invert.

If the desired position is x_d, the error can be defined by

$$e(k) = x_d - x(k) \tag{4-27}$$

If b is treated as known, for the feedback control law,

$$u_p(k) = \frac{1}{b} K_c e(k) \tag{4-28}$$

e(k+1) can be expressed as

$$e(k+1) = (1 - K_c)e(k) \tag{4-29}$$

Equation (4-29) is asymptotically stable for

$$0 < K_c < 2 \tag{4-30}$$

The controller proposed here should be used after a conventional controller (such as a PID controller) brings the system into the vicinity of a desired position and should operate as follows: first, the difference between the desired and actual positions of the system are determined using (4-27), and second, we use equations (4-28), (4-26) and (4-25) to calculate the d[k+1] and h_1. After sending the calculated pulse to the motor, the controller waits until the system is stuck (250 ms or more). If the difference

between the newly measured and the desired position is outside the bounds of the required precision, a new impulse control cycle is initiated.

4.4.2 Simulation

Using a sampling rate of 250ms, the simulation results for desired arm displacement x_d=100um and x_d= -100um are shown in Figure 4-21 and Figure 4-22.

4.4.3 Experiment

The impulse controller is implemented using a capacitance sensor for feedback and a sampling rate of 250 ms. Before every impulse is input into the system, the saturation condition for the amplifier must be checked. We choose K_c=1, and the results for the desired displacements x_d=100um and x_d= -100um are shown in Figure 4-23 and Figure 4-24.

It is evident that the system has a settling time of under 1s and that a steady state error of less than 0.3 um could be achieved. This is less than one fifth of an encoder count (about 1.5 um). Here, the sampling rate is 250 ms in order to make the impulse response more predictable. The physical reason for this is that the load inertia must slide to a complete stop in order for the next impulse response to be consistent. The optimal sampling rate will be investigated in next chapter.

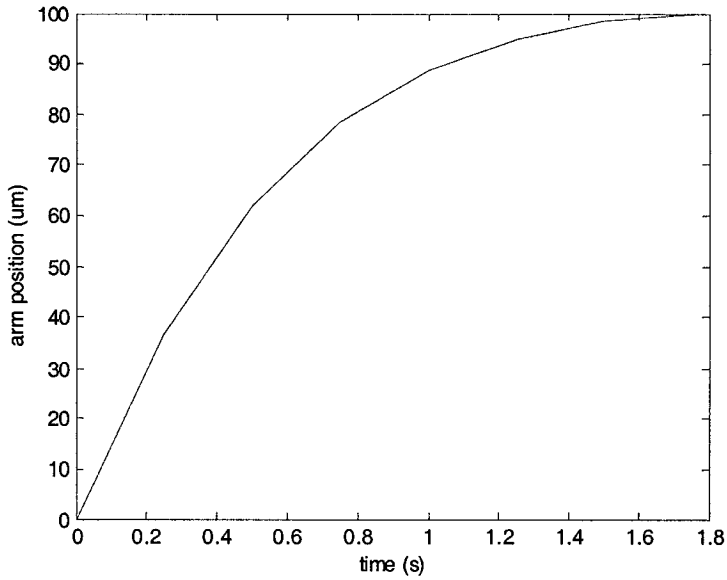

Figure 4-21 Impulse control simulation for x_d=100um

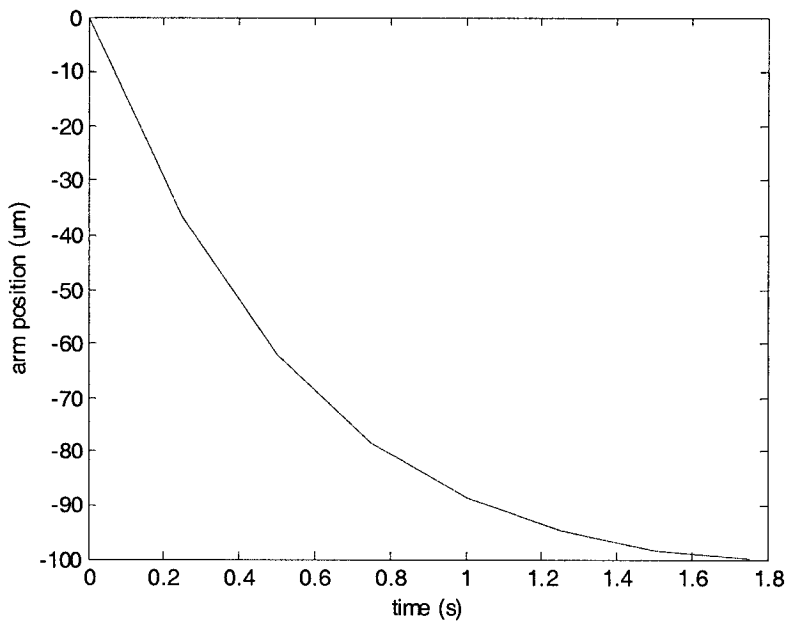

Figure 4-22 Impulse control simulation for x_d=-100um

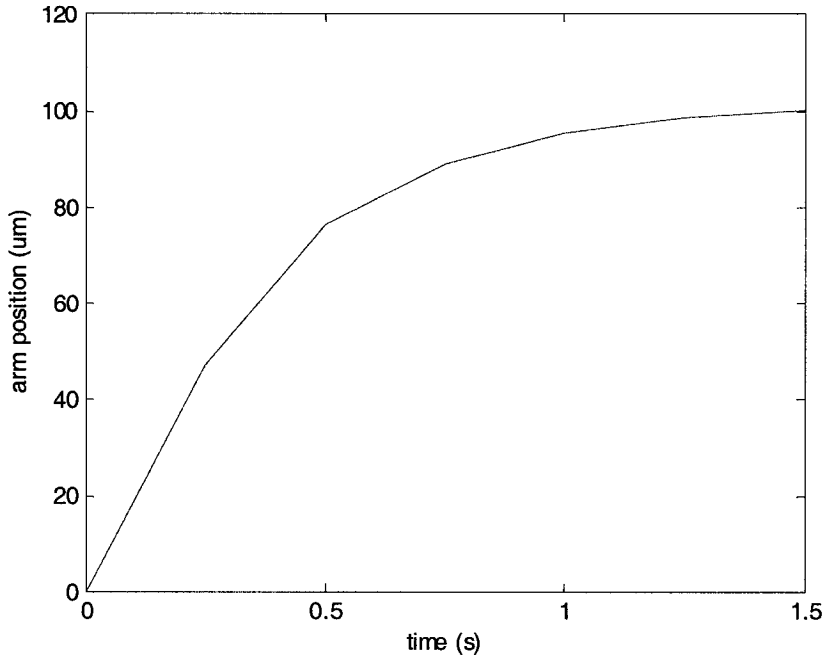

Figure 4-23 Impulse control experiment for x_d=100um

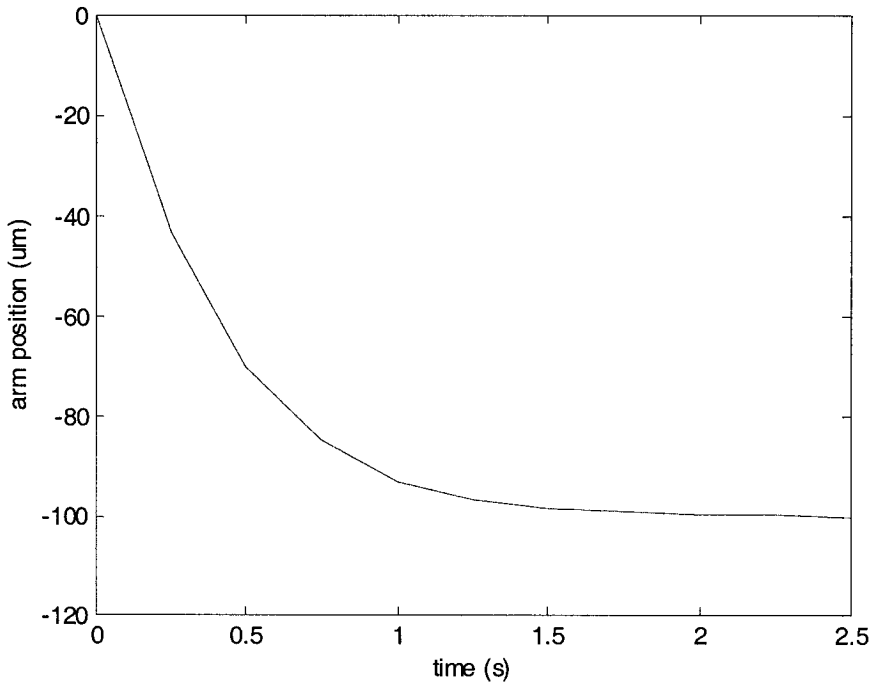

Figure 4-24 Impulse control experiment for x_d = -100um

4.5 Resolution Characterization

One of the most critical performance characteristics of the manipulator is the ability to consistently move in small motion increments. This characteristic is known as resolution and is defined as the smallest reproducible motion step the machine can consistently make during point to point motion. A machine's resolution effectively puts an upper limit on the repeatability and precision that can be achieved even with closed-loop feedback. The resolution of a machine should be verified experimentally since it often depends on subtle machine dynamic factors that are difficult to model; these can include gear meshing, bearing noise, and transmission stiffness. Statistical measurements should also be used since the factors that influence resolution can vary over time and the range of the mechanism.

The resolutions of one mechanism for different inputs may be different. For example, the resolution for a linear controller is different from that for an impulse controller. The resolutions under these two controllers are tested as follows.

4.5.1 Resolution for linear controller with motor position feedback

For this test we consider only the motor encoder sensor for feedback since it is the most common type used in industry. It is also much more practical (in terms of range) and more economical than other high accuracy sensors (such as capacitance sensors). The resolution test for the arm consists of 1000 steps in one direction from which a histogram of the resultant displacement is made. The displacements are determined using a capacitance sensor that measures the output of the arm. The initial step size

used is one motor encode count. If this size produces inconsistent increments, the magnitude of the step is increased by one encoder count and the test is run again. This process is repeated until consistent motion is observed. By consistent motion we mean that for every input, the output of the arm is approximately the same. For example, Figure 4-25 shows the output of the arm motion when the motor moves one encoder count every time, and it is an inconsistent motion; in Figure 4-26 the arm motion is consistent. The minimum value of the arm consistent increments is the resolution of the mechanism.

For the 1000 steps of one encoder count increment (approximately 1.5 um of arm displacement), the arm displacement is shown in Figure 4-27. The histogram of the arm displacement is shown in Figure 4-28.

It is apparent from the histogram that consistent motion of one encoder count is possible. It should be noted that due to the non-Cartesian nature of the arm kinematics, one encoder count can represent between 1um to 2um depending on the position of the sensor mounted. However, for most of the workspace, one encoder count is less than 1.5um; all motions that occur are less two encoder counts (3um). Therefore, the resolution of the arm for linear controller is 3um.

4.5.2 Resolution for impulse controller

For the resolution of the impulse controller, if the capacitance sensor is used for feedback, the motor can have a step motion less than one encoder count. To determine the resolution under impulse control, the pulse width is set to some nominal value (W=1 ms) and the impulse amplitude is increased from zero until the smallest consistent arm

motion is observed. In order to obtain consistent resolution measurements from simulations and experiments, the following mathematical definition of resolution was used:

Definition: Resolution for impulse inputs

A sequence of N impulse inputs with the same amplitude is applied to the system and the median and maximum value of the N increments is recorded. Starting from an impulse amplitude of zero, it is gradually increased until a consistent median increment is achieved that is larger than a small threshold tolerance ε_1. This threshold input is then multiplied by $(1+\varepsilon_2)$ where ε_2 is the small tolerance that provides consistent motion in the presence of small input and parameter variations. The maximum increment due to this input is defined as the resolution of the system.

In our application we set ε_1=0.1um and ε_2=0.01. This above definition was used to test the resolution under an impulse control with N=1000 pulses. The measured arm position is shown in Figure 4-29. The histogram of the arm increment is shown in Figure 4-30. It is evident from the histogram that almost all motion increments are less than 0.3um so the resolution under impulse control is 0.3um. This resolution is ten times better than can be achieved using conventional linear control.

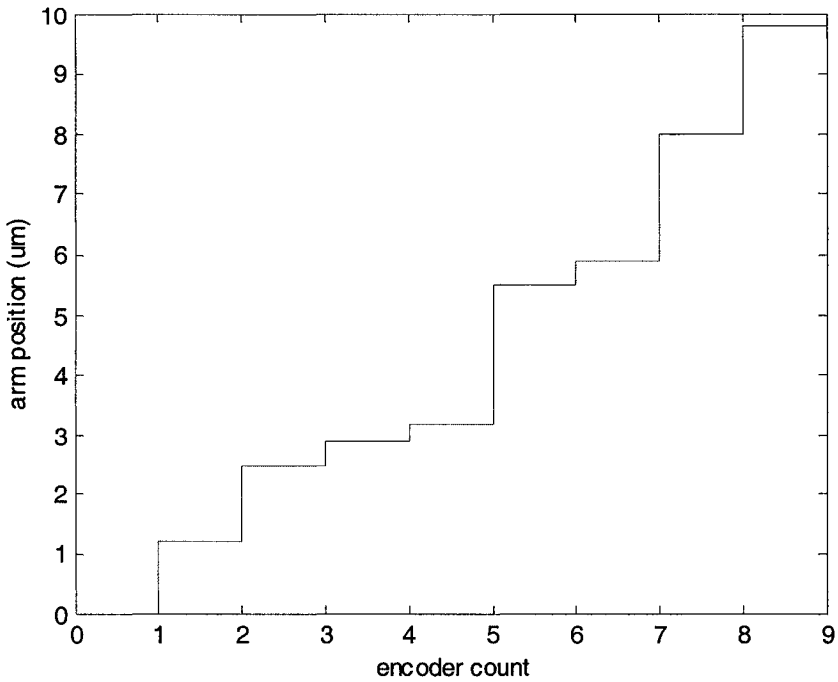

Figure 4-25 Inconsistent motion

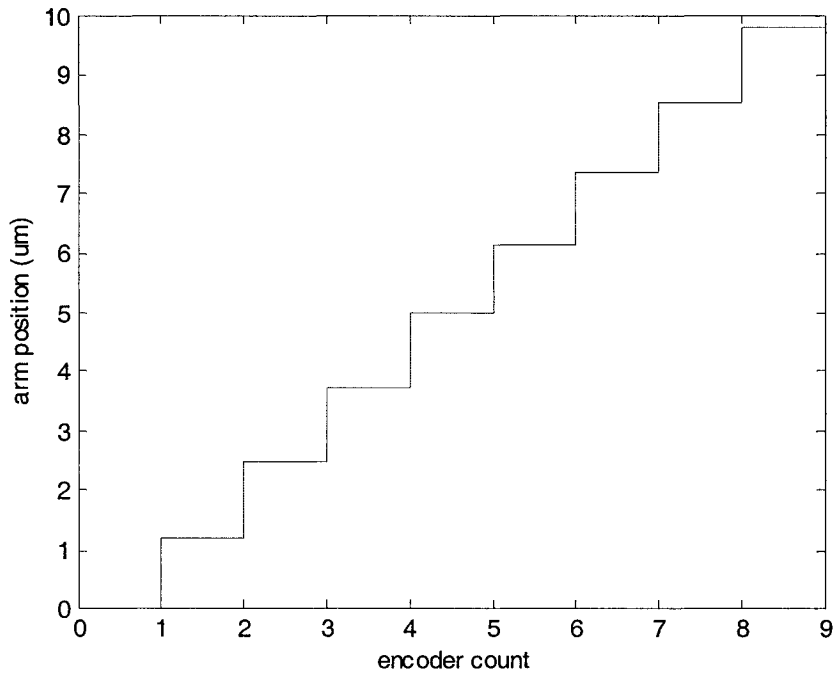

Figure 4-26 Consistent motion

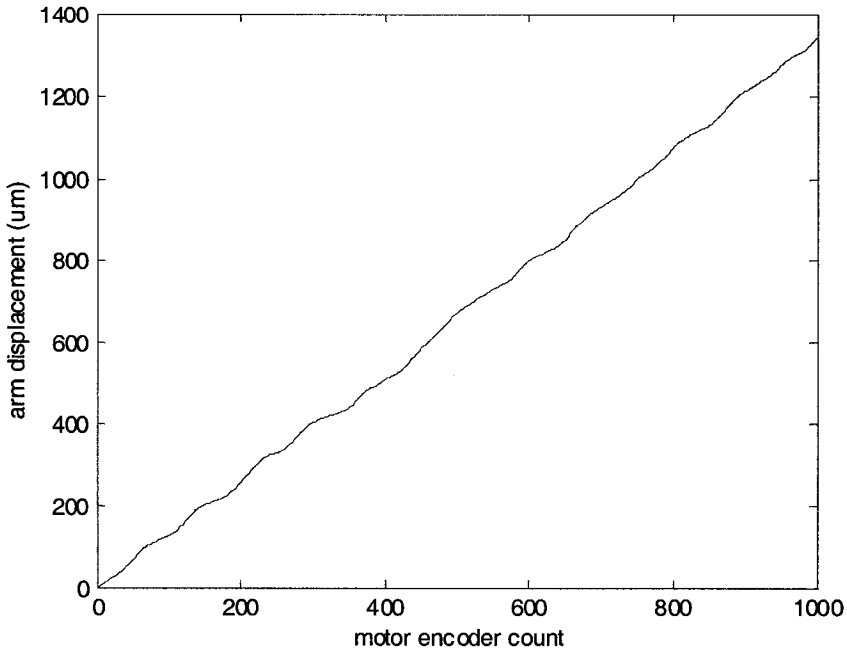

Figure 4-27 Arm displacements for 1000 encoder count steps

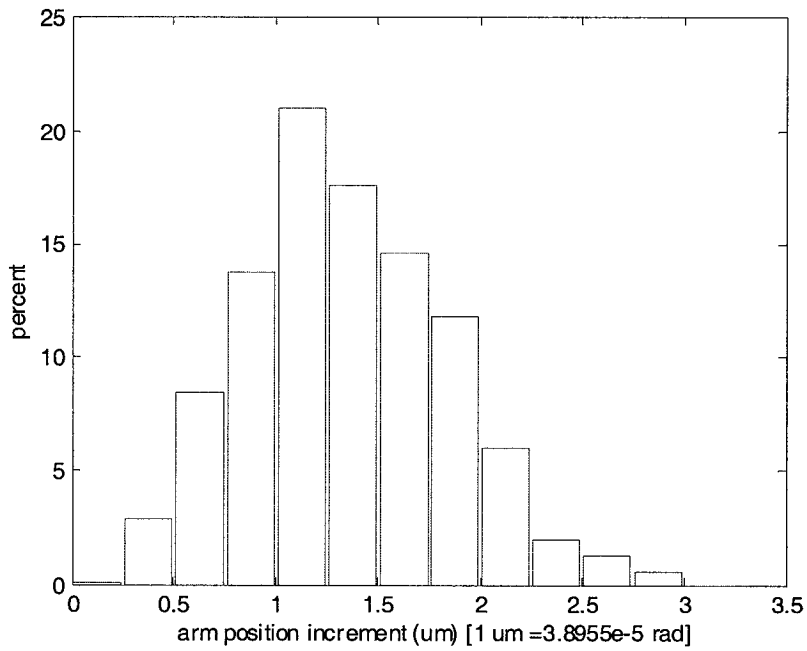

Figure 4-28 Histogram of resolution for 1000 encoder count steps

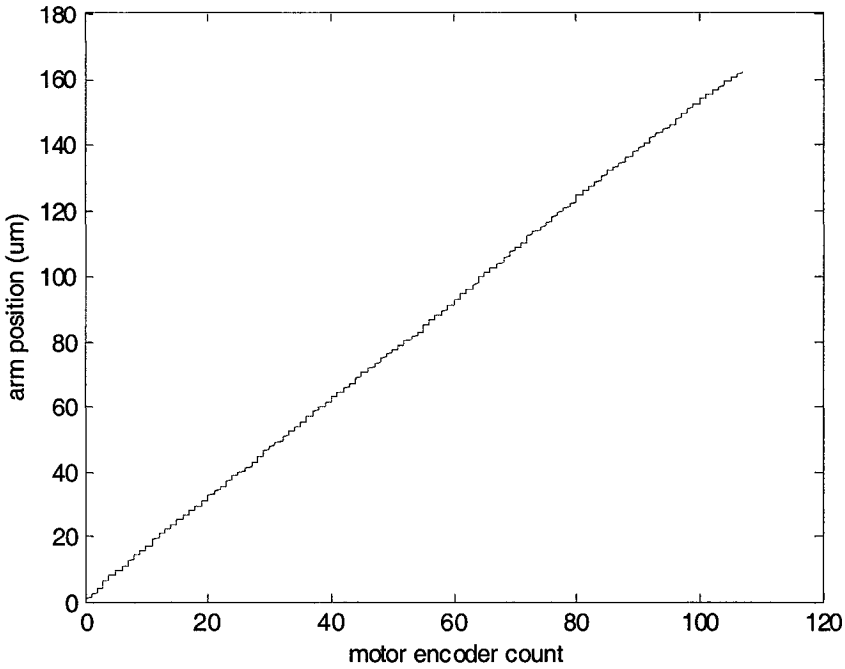

Figure 4-29 Arm displacements for 1000 impulse steps

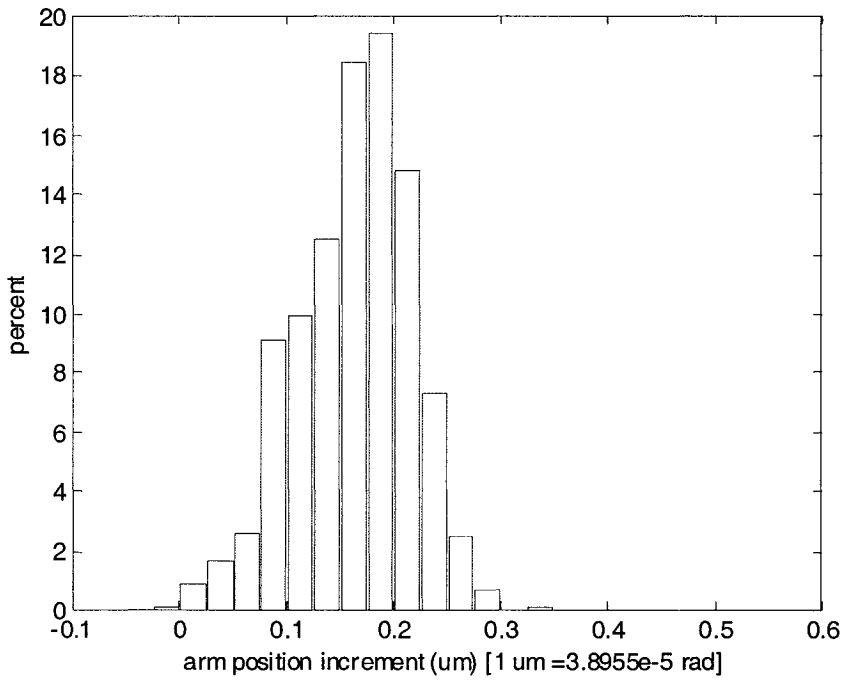

Figure 4-30 Histogram of resolution for 1000 impulse steps

Chapter 5 Adaptive Impulse Control

5.1 Introduction

Some issues must be considered when using impulse control. The first is resolution, the second is dead zone, the third is settling time, and the fourth is robustness to parameter variations. Resolution is related to control precision; the higher the resolution, the better control precision we can achieve. A dead zone is quite undesirable in impulse control. Getting rid of the dead zone is our objective in impulse control. The settling time is related to production rate and should be small so that the system converges as quickly as possible. Since parameter uncertainties exist in the system, the selected control algorithm should be robust so that the control results are consistent.

In order to make the impulse control more predicable, every pulse must be applied after the system sticks. Additionally, the pulse rate must be long enough. If the pulse rate is too long, the system will still be stuck when another pulse is applied, but if the settling time is too long, the production rate will decrease. Section 5.2 investigates if there are any optimal pulse rates for impulse control. One attempt made to decrease settling time is through adaptive impulse control, which will be presented in Sections 5.5 and 5.6.

Equation (4-9) demonstrates that the motor inertia can be moved only when the pulse momentum is big enough to overcome the motor inertia friction momentum. Once the

motor inertia moves, the motor inertia kinetic energy also must be exceed a certain amount so that the accumulated potential energy can drive the load inertia motion. If the work done by pulse momentum is smaller than that threshed, the load inertia cannot move. This is why a dead zone appears in Figure 4-17 and Figure 4-18. From the above analysis, we can conclude that the product of pulse amplitude and pulse width must be bigger than the threshed to eliminate the dead zone.

As mentioned in the last chapter, the combination of the first two harmonic pulses is one option to get rid of a dead zone. In this pulse shape, the function of the first harmonic is the main control input to drive the arm to move a desired displacement. When the amplitude of the second harmonic is bigger than the threshed, the dead zone is eliminated. Other questions such as, is there any other pulse shape can also get rid of dead zone? and which is the best pulse shape for impulse control? will be answered in section 5.3

When h2 = 3.2Vs, the dead zone can be eliminated. But when system friction is increased, the dead zone may come back again. Is there any way to increase system friction that will be robust to the friction variation? This will be also presented in section 5.3 and 5.4.

In the last chapter, the resolution is tested for the harmonic motor system. As the friction of the system changes, the resolution and dead zone may change as well. Other parameters such as flexibility (spring constant K_s), and load inertia J_l may also have an effect on the resolution. How do they influence the resolution and dead zone? This will be studied in section 5.4.

The main issues that must be considered and the factors that may have influence on

the issues are listed in Table 5-1:

Table 5-1 Main issues in impulse control and their factors

issue	factors
resolution	load side friction, flexibility, load inertia
dead zone	load side friction, flexibility, load inertia
settling time	pulse rate, control approach
robustness	pulse shape

5.2 Pulse rate optimization

When a pulse is applied to the motor side of harmonic drives, the momentum of the pulse makes the motor inertia motion. The kinetic energy of motor inertia is then converted to potential energy. The load inertia starts moving only when the potential energy has accumulated to a certain amount. Since flexibility exists in harmonic drives, the load inertia has a vibration during its motion. Furthermore, because the load side friction is relatively small, it will take a relatively long period to make the load inertia stick; it is important to find an optimal pulse rate.

We take nine pulse rates (10ms, 20ms, 50ms, 100ms, 200ms, 250ms, 400ms, 600ms, 800ms) and test resolutions under impulse control for these pulse rates; it is found that the resolutions are different, as shown in Figure 5-1.

It is clear from Figure 5-1 that the resolution goes up if the pulse rate is less than

250ms. This is because the arm is still in vibration condition and the maximum delta is big. The measured displacement is not consistent. Figure 5-2 shows the motion of the arm in the first 6 pulses when the pulse rate is 50ms. After 250ms, the system is stuck and the resolution becomes steady. When the pulse rate is 400ms, the motion of the arm in the first 6 pulses is shown in Figure 5-3.

It is apparent that the optimal pulse rate is around 250ms. This pulse rate can assure that the system sticks and also provides the highest production rate.

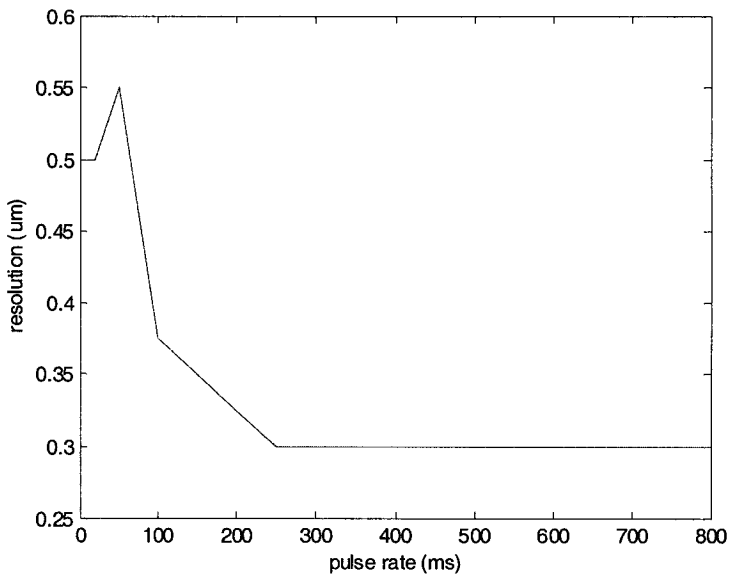

Figure 5-1 Resolution varies with pulse rate

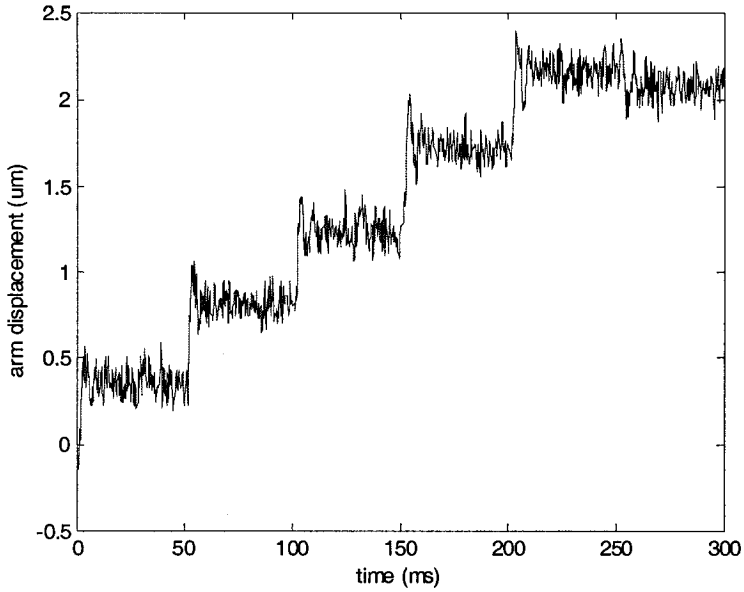

Figure 5-2 Pulse rate 50 ms: inconsistent motion

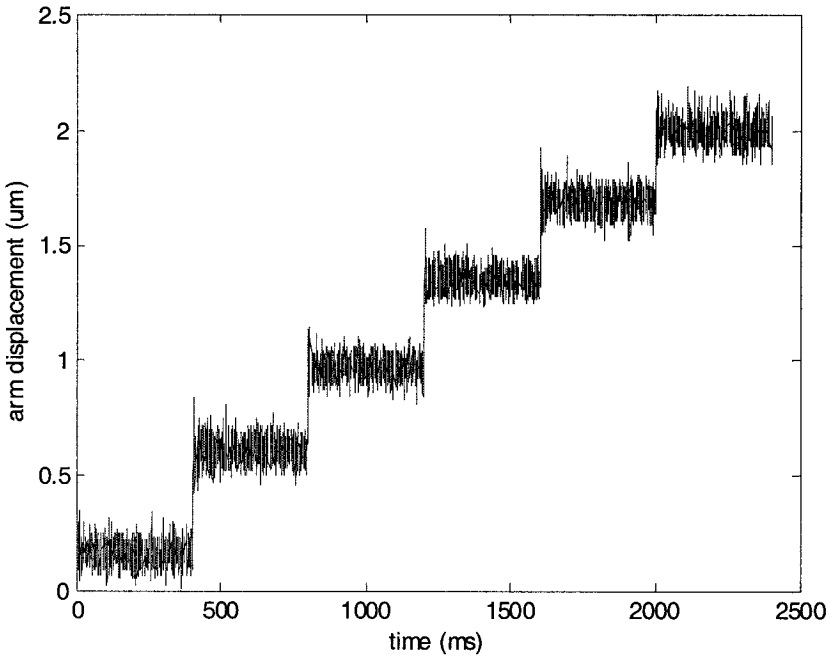

Figure 5-3 Pulse rate 400ms: consistent motion

5.3 Pulse shape optimization

Normally, the pulse shapes used are square, sine wave and their combinations. The different pulse shapes have different control effects. These pulse shapes are studied in detail in this section.

5.3.1 Square pulse

In order to overcome the static friction, the square pulse amplitude is fixed in four times of static friction, h=4Vs. The pulse shape is shown in Figure 5-4.

For different pulse width and amplitude, the simulation of arm displacement to the pulse is shown in Figure 5-5. The experimental results are similar to that of the simulation and are shown in Figure 5-6. There is a dead zone that appears in the graphs. Even when the pulse amplitude is 4 times that of the static friction, the pulse width must be bigger than 0.2ms so that the pulse momentum is big enough to drive the arm's motion.

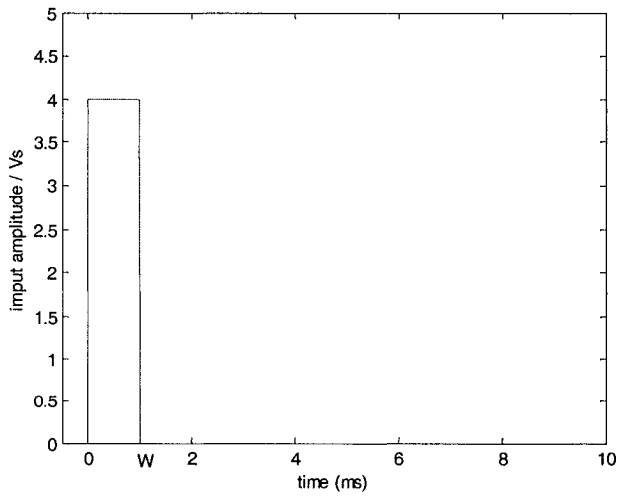

Figure 5-4 Square pulse shape

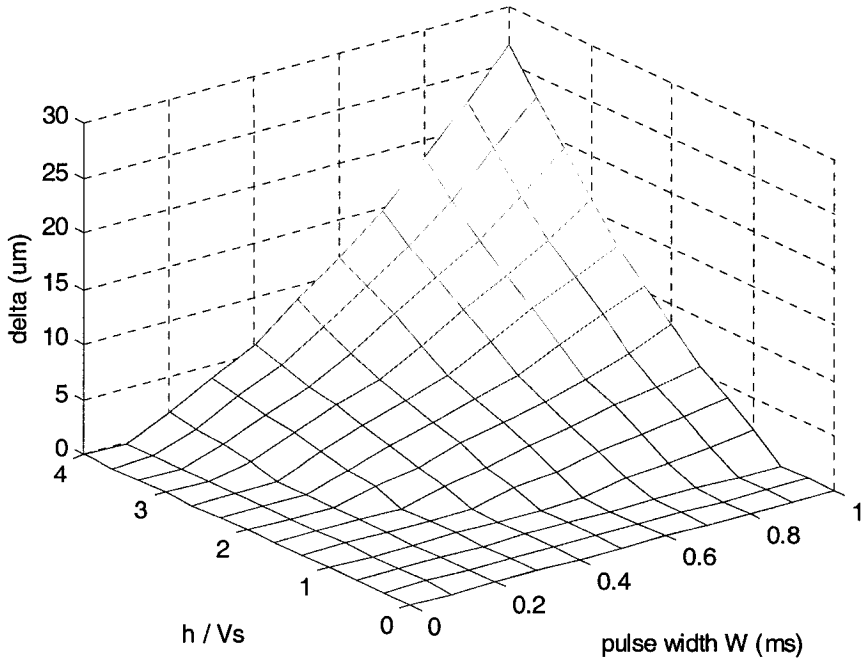

Figure 5-5 Simulation of arm response to the square pulse

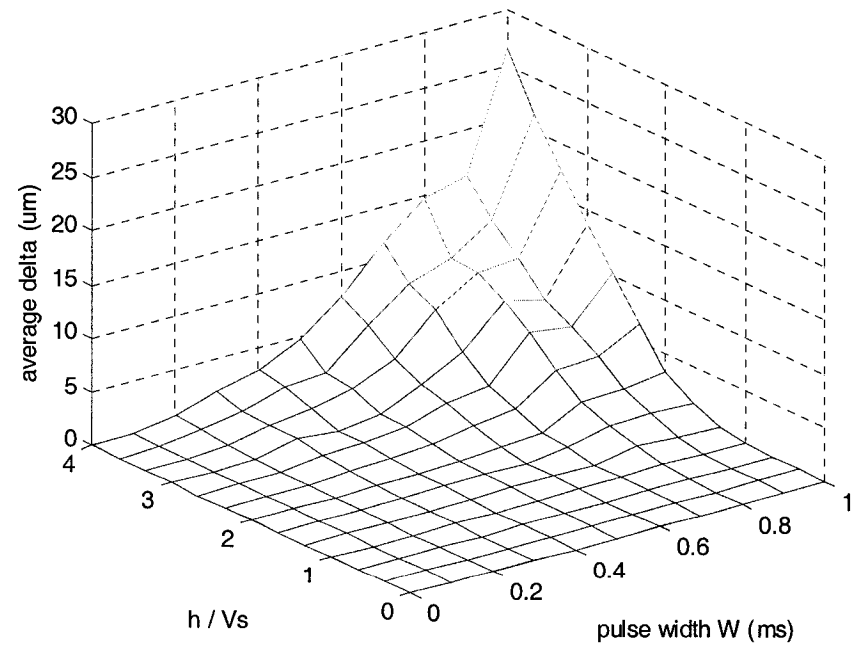

Figure 5-6 Experiment of arm response to the square pulse

5.3.2 First harmonic pulse

We use the first harmonic pulse shape:

$$V = h_1 \sin(\pi t/W) \qquad (5\text{-}1)$$

where h_1 is the amplitude. Similar to the square pulse, let h_1 equal four times the static friction: $h_1 = 4Vs$. If we set W= 1ms, the pulse shape is shown in Figure 5-7.

For different pulse widths and amplitudes, the simulation and experimental responses are shown in Figure 5-8 and Figure 5-9. It is clear that there is a dead zone similar to that in the square pulse. The dead zone is bigger than that in the square pulse and is apparent because the momentum is smaller.

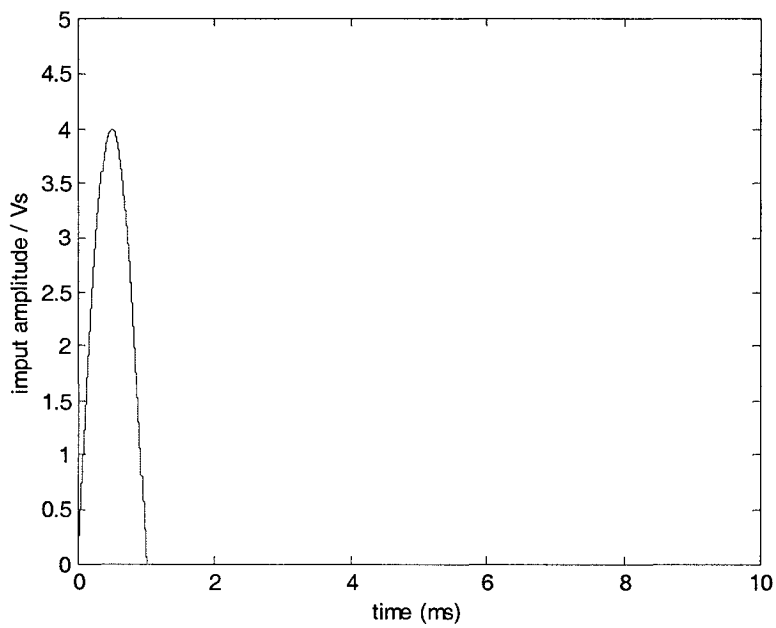

Figure 5-7 First harmonic pulse shape

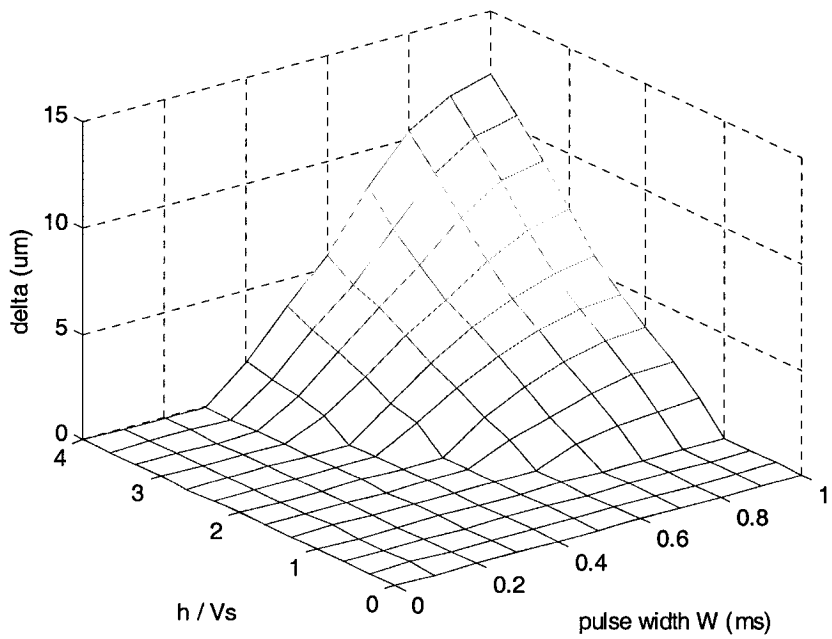

Figure 5-8 Simulation of arm response to first harmonic pulse

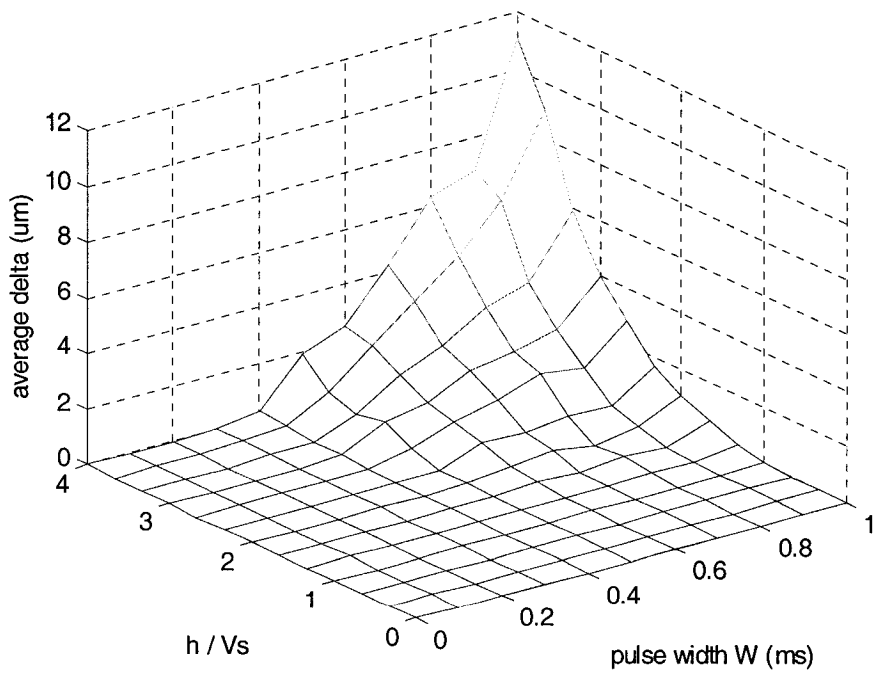

Figure 5-9 Experiment of arm response to first harmonic pulse

5.3.3 Pulse of the sum of two harmonics

For the combinations of the first four harmonics, the following three forms of pulse shape are studied:

(1) First and second harmonics:

$$V=h_1 \sin(\pi t/W)+ h_2 \sin(2\pi t/W) \quad 0 \le t \le W \qquad (5\text{-}2)$$

(2) First and third harmonics

$$V=h_1 \sin(\pi t/W)+ h_3 \sin(3\pi t/W) \quad 0 \le t \le W \qquad (5\text{-}3)$$

(3) First and fourth harmonics

$$V=h_1 \sin(\pi t/W)+ h_4 \sin(4\pi t/W) \quad 0 \le t \le W \qquad (5\text{-}4)$$

In equation (5-2),

$$V(h_1, h_2)=h_1 \sin(\pi t/W)+ h_2 \sin(2\pi t/W)$$

If we use a negative amplitude

$$V(-h_1, -h_2)= -h_1 \sin(\pi t/W) -h_2 \sin(2\pi t/W)= - V(h_1, h_2) \qquad (5\text{-}5)$$

$$V(-h_1, h_2)= -h_1 \sin(\pi t/W) +h_2 \sin(2\pi t/W)= - V(h_1, -h_2) \qquad (5\text{-}6)$$

Meaning that the arm displacement in the first quadrant is a negative symmetrical to the third quadrant, and arm displacement in the second quadrant is a negative symmetrical to the fourth quadrant, Similarly, this applies to equations (5-3) and (5-4). This can be verified in the following simulations.

5.3.3.1 First and second harmonics

The pulse shape is shown in Figure 4-13. The simulation arm displacement to the

above pulse shape is shown in Figure 5-10. When h_2 is set to zero, the arm's displacements vary with h_1 as shown in Figure 5-11. When h_1 is set to zero, the arm's displacements vary with h_2 as shown in Figure 5-12.

It is evident that the main displacement is produced by the first harmonic pulse. The second harmonic pulse can eliminate the dead zone when $h_2 \geq 3.1278$ Vs.

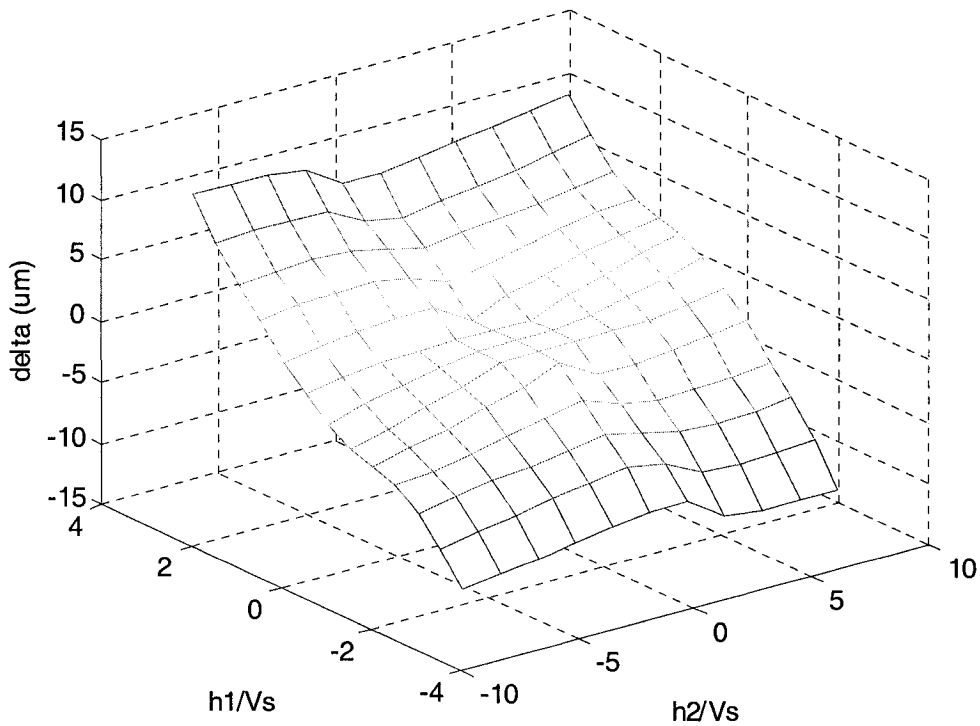

Figure 5-10 Simulation response to the pulse of first two harmonics

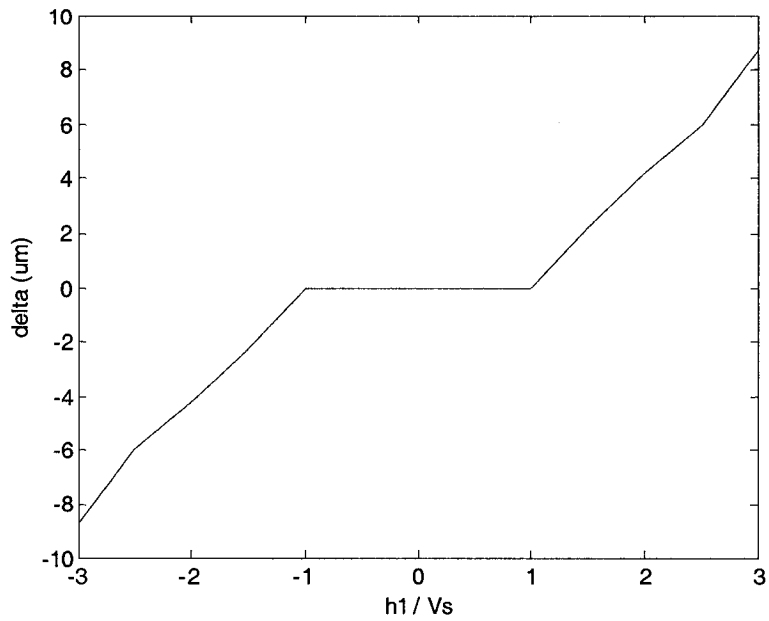

Figure 5-11 Arm increment varies with h_1 when h_2=0

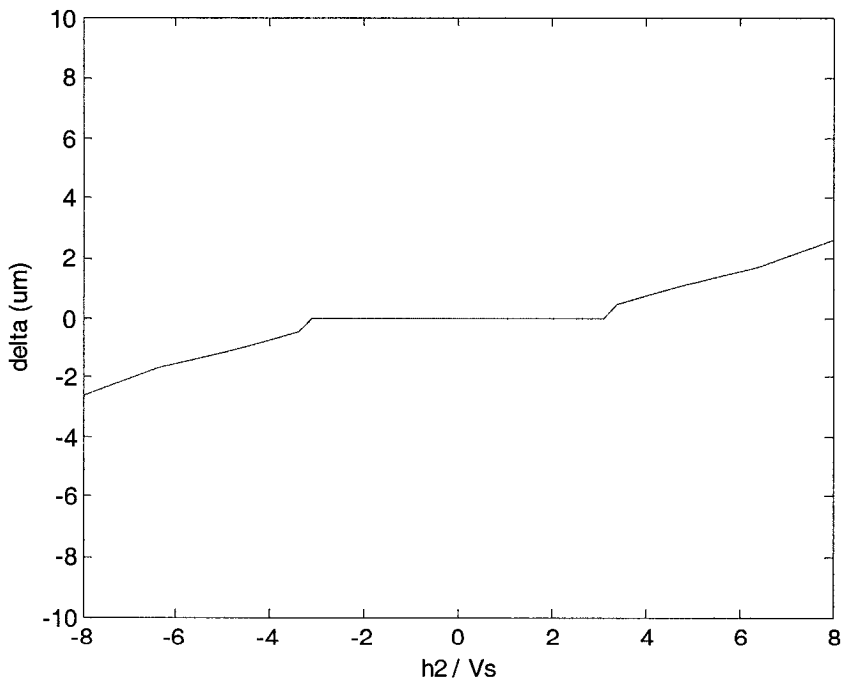

Figure 5-12 Arm increment varies with h_2 when h_1=0

5.3.3.2 First and third harmonics

The pulse shape is shown in Figure 5-13. There are two of the same pulses in 1ms. Simulation arm displacement to the above pulse shape is shown in Figure 5-14. When h_3 is equal to zero, the arm's displacements varied with h_1 like in Figure 5-11. When h_1 is equal to zero, the arm displacements varied with h_3 as shown in Figure 5-15. Clearly, the third harmonic pulse has a similar effect as the first harmonic, but it produces much less arm displacement than the first harmonic pulse. Furthermore, the frequency of the third harmonic is three times that of the first harmonic. It is harder to keep the pulse shape in a small pulse width in experiments, so it is better not to use the third harmonic pulse.

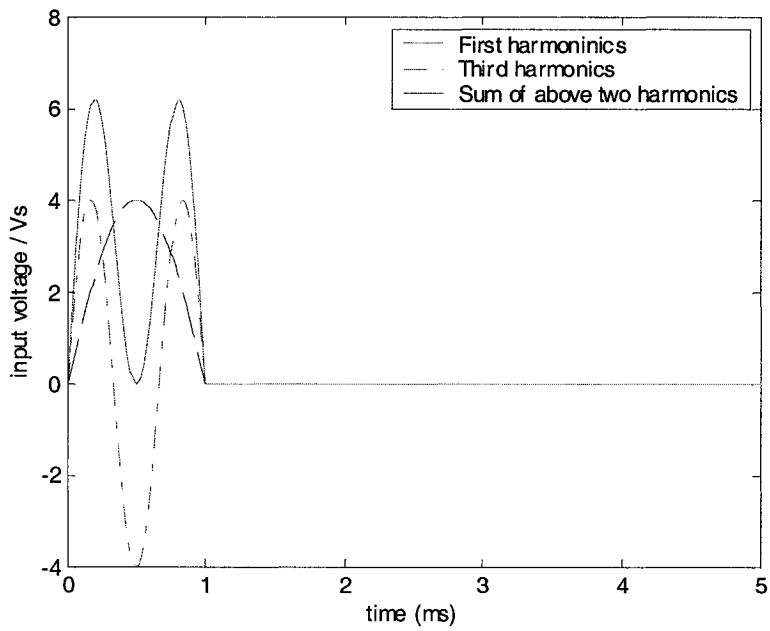

Figure 5-13 Pulse shape of first and third harmonics

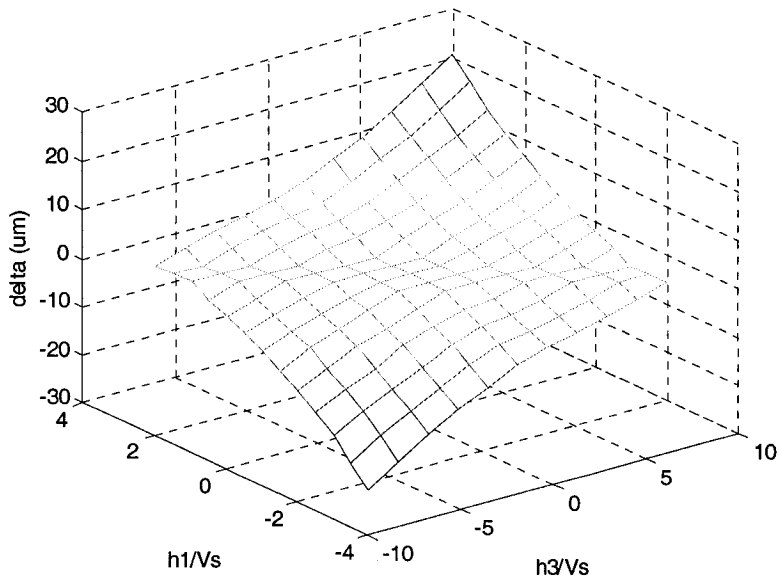

Figure 5-14 Simulation of response to the pulse of first and third harmonics

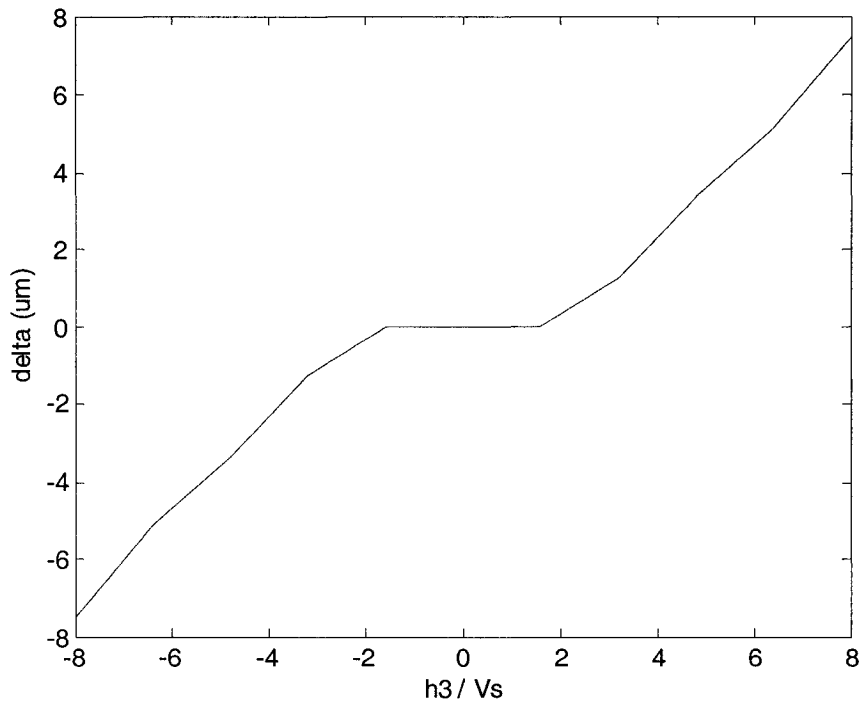

Figure 5-15 Arm increment varies with h_3 when h_1=0

5.3.3.3 First and fourth harmonics

The pulse shape is shown in Figure 5-16. There are three pulses in 1ms: two pulses are positive and one is negative. The simulation arm displacement to the above pulse shape is shown in Figure 5-17. Similarly, when h_4 is equal to zero, the arm displacements varied with h_1 and are the same as in Figure 5-11. When h_1 equals zero, the arm displacements varied with h_4 as shown in Figure 5-18. It is evident that the fourth harmonic has a similar effect as the second harmonic, but the arm displacement is even smaller than that of the second harmonic. It can eliminate the dead zone only when h_4>5Vs. The large amplitude of h_4 will produce the problem of amplifier saturation.

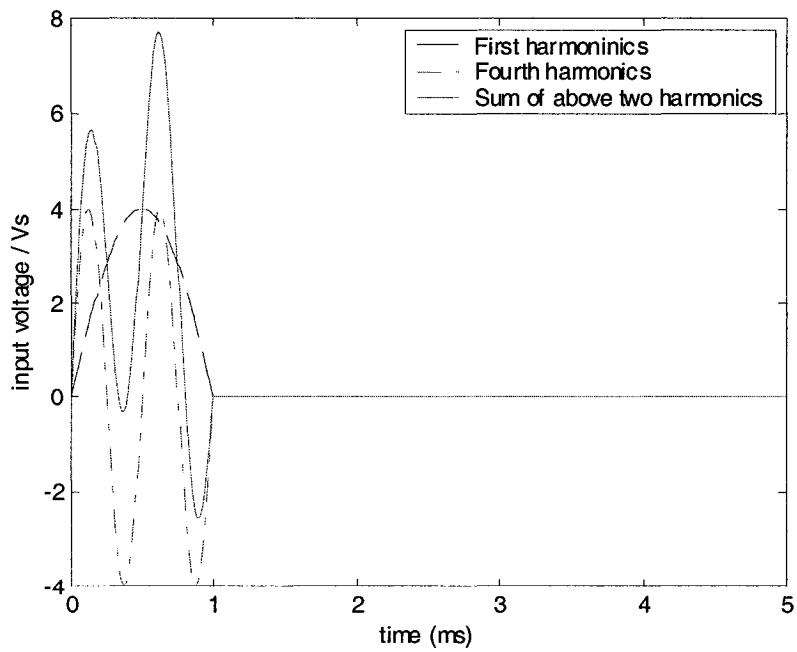

Figure 5-16 Pulse shape of first and fourth harmonics

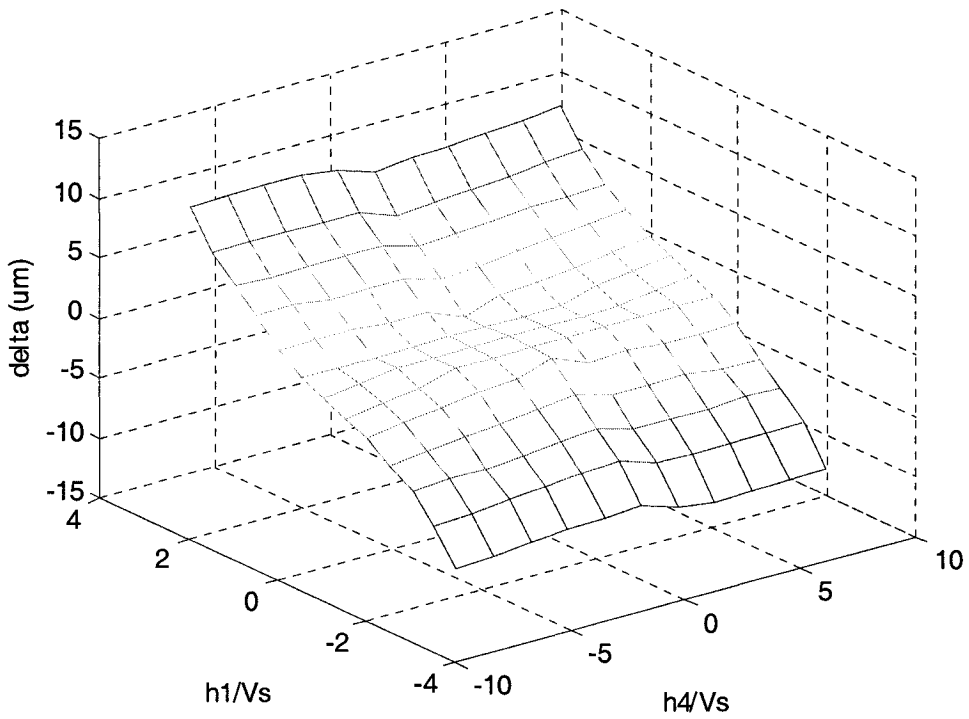

Figure 5-17 Simulation of response to the pulse of first and fourth harmonics

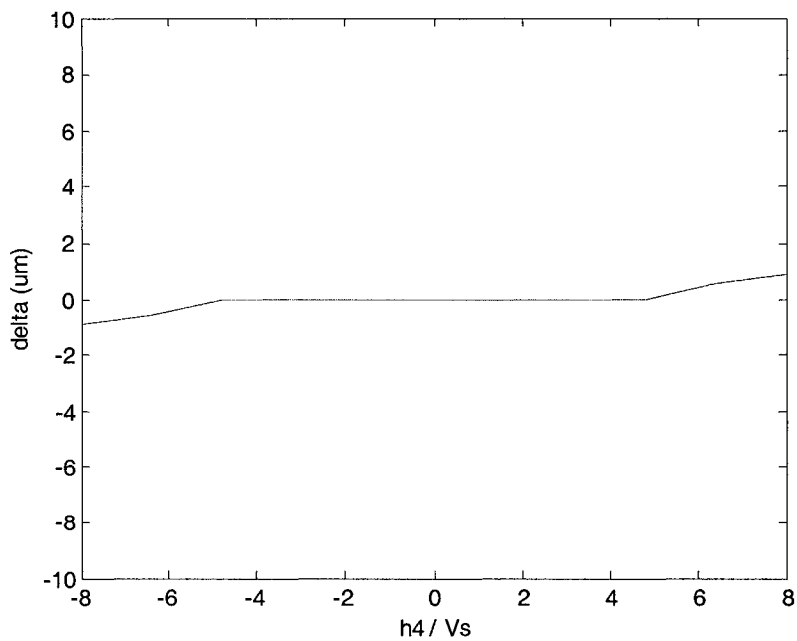

Figure 5-18 Arm increment varies with h_4 when h_1=0

5.3.3.4 Robust impulse shapes

In impulse control, if a pulse shape can eliminate a dead zone every time in load side friction variation, this pulse shape is a robust pulse shape.

When h_2=3.1278Vs in simulation, the dead zone can be eliminated. The arm displacement varies with h_1 and is shown in Figure 4-19. If it is extended to the third quadrant, there is still a dead zone when h_1 is a small negative value, as shown in Figure 5-19. Since the friction is symmetrical, when the error is negative, the h_1 needs to be negative to drive the motor's movement in a negative direction, and h_2 is also required to be equal to –3.1278Vs in order to extend the parabolic curve to the third quadrant negative symmetrically as shown in Figure 5-20.

To see the robustness of the pulse shape in relation to the friction variation, the load side friction f_l is increased from its original value of 0.0018Nm to 0.00313Nm (increase friction about 75%), keeping h_2=3.1278Vs even when the motor moves in a negative direction, and a dead zone appears again, as shown in Figure 5-21.

In order to eliminate the dead zone after load side friction increases, h_2 is required to be increased to h_2=5Vs, as shown in Figure 5-22. It is clear that the curve is not a negative symmetrical in the first and third quadrant since h_2 is kept positive when the motor moves in a negative direction.

Now if the load side friction returns to the original value of f_l=0.0018Nm, the dead zone does not appear again, as shown in Figure 5-23. In both graphs, the points of the curve across the x-axis are almost the same.

So we can use a large value of h_2 (bigger than 3.1278Vs) to eliminate the dead zone even if we do not change the sign of the h_2 when the error is negative. It is robust to the friction variation by using h_2 to eliminate the dead zone. This will be verified in robust adaptive impulse control in section 5.6.

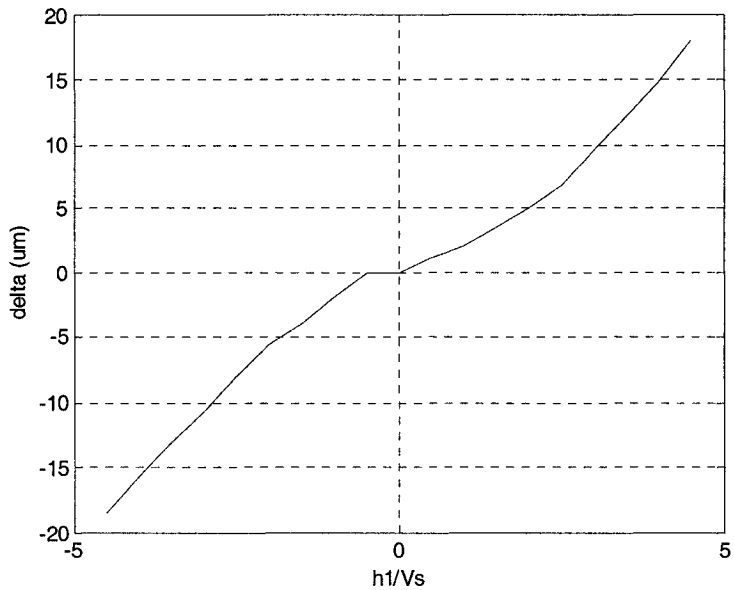

Figure 5-19 Arm increment (simulation) (h_2/Vs=3.1278, f_l=0.0018Nm)

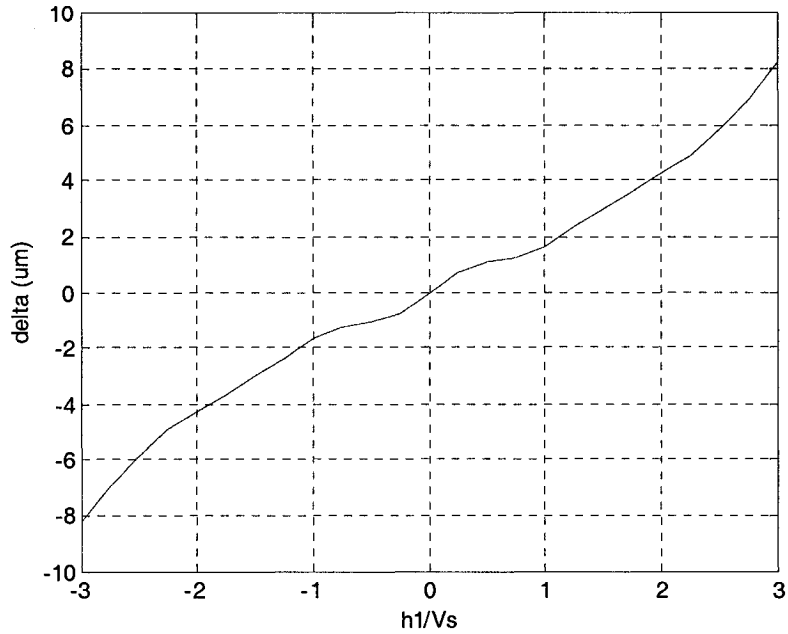

Figure 5-20 Arm increment (simulation) (h_2/Vs=±3.1278, f_l=0.0018Nm)

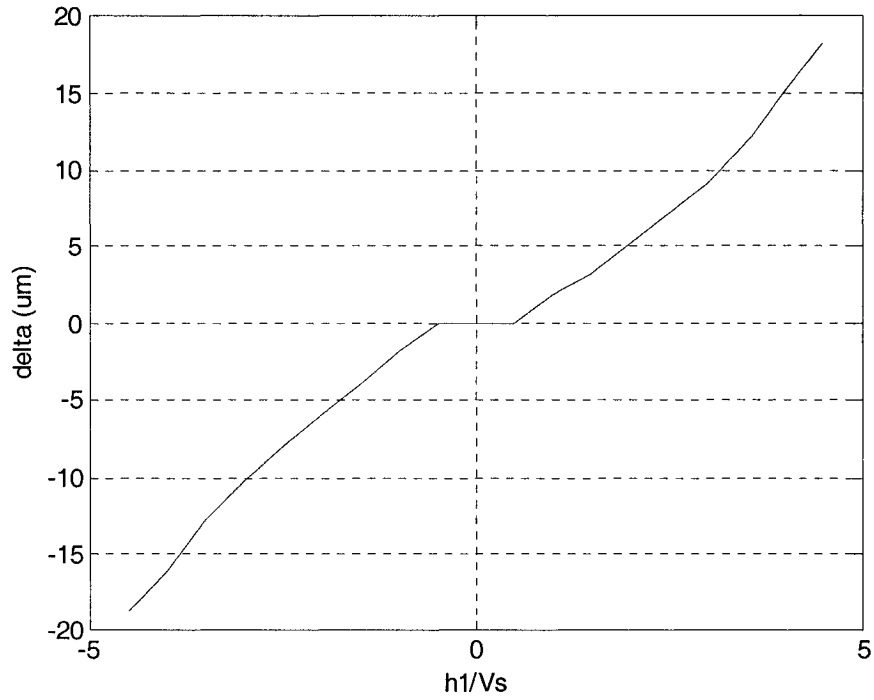

Figure 5-21 Arm increment (simulation) (h_2/Vs=3.1278, f_l=0.00313Nm)

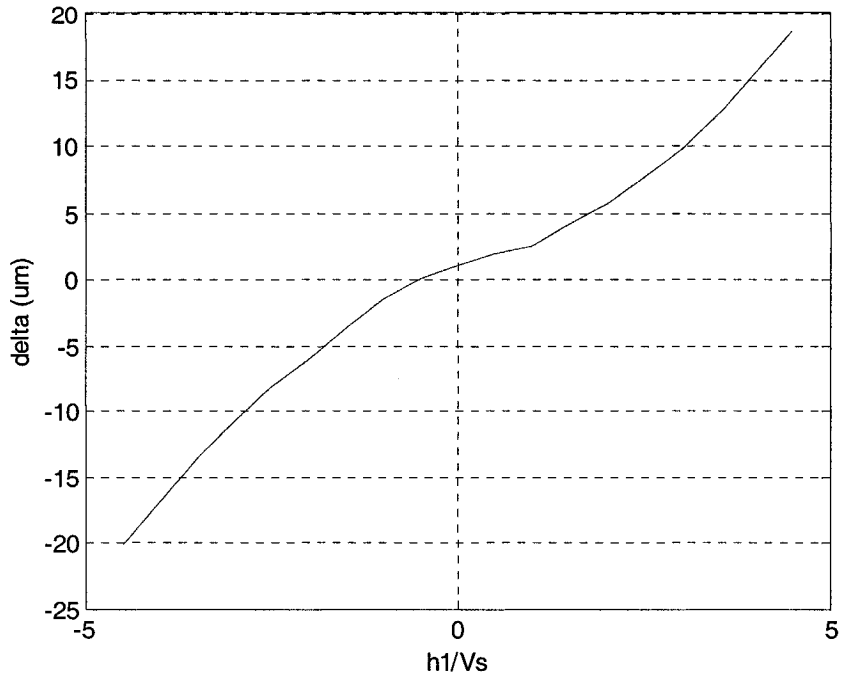

Figure 5-22 Arm displacement (simulation) (h_2/Vs=5, f_1=0.00313Nm)

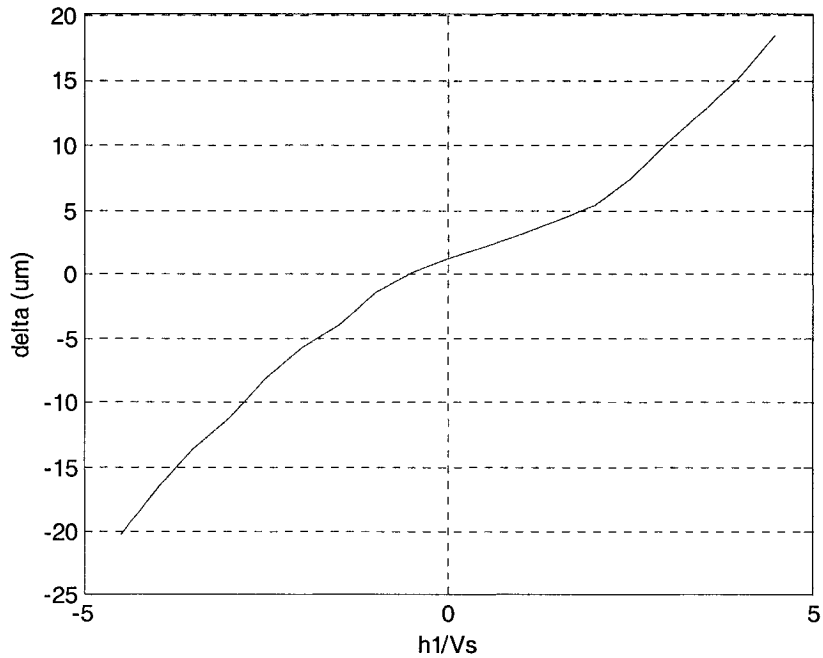

Figure 5-23 Arm displacement (simulation) (h_2/Vs=5, f_1=0.0018Nm)

5.3.3.5 Conclusion for pulse shape optimization

Since single square pulse or first harmonic pulse has dead zone problems, and they cannot be eliminated in practical control, they are not the optimal pulse shape. Using the sum of two harmonic pulses can eliminate the dead zone.

The arm displacement can mainly be produced by odd order harmonic pulses, and the dead zone can be eliminated by even order harmonic pulses. The higher order the harmonic pulse is, the harder it is to realize the pulse shape in practical digital control. For the even order harmonic pulse, the higher the order is, the bigger the amplitude required to eliminate the dead zone. Furthermore, the harmonic pulse effect decreases when the order increases.

From the above analysis, the optimal pulse shape is the sum of the first two harmonics. When a large h_2 value is used, the system is robust to the friction variation in eliminating the dead zone. The bigger h_2 is, the more robust to the friction variation, as long as the amplifier is not saturated.

5.4 Parameter variations

5.4.1 Non-dimensional equation

The system parameters have a great effect on the impulse control effect such as resolution and dead zone. Unfortunately, there is almost no literature investigating this area so far.

In order to understand how the parameter variations affect the output displacement and make the following analysis more general to other systems, the non-dimensional

equations are derived first. The system's mathematical model stated in Chapter 2:

$$J_m\ddot{q}_m = F_m - rK_s(rq_m - q_l) - \frac{K_m K_b}{R}\dot{q}_m + \frac{K_m}{R}u(t) \tag{5-7}$$

$$J_l\ddot{q}_l = F_l + K_s(rq_m - q_l) \tag{5-8}$$

when the velocity is not zero and we neglect the viscous friction, set $f_m = f_{sm} = f_{cm}$, $f_l = f_{sl} = f_{cl}$, the friction can be written as:

$$F_m = -\text{sgn}(\dot{q}_m) f_m \tag{5-9}$$

$$F_l = -\text{sgn}(\dot{q}_l) f_l \tag{5-10}$$

The motor input torque is $T_m = \frac{K_m}{R}u(t) - \frac{K_m K_b}{R}\dot{q}_m$, then equation (5-7) and (5-8) can be written as:

$$J_m\ddot{q}_m = -\text{sgn}(\dot{q}_m) f_m - rK_s(rq_m - q_l) + T_m \tag{5-11}$$

$$J_l\ddot{q}_l = -\text{sgn}(\dot{q}_l) f_l + K_s(rq_m - q_l) \tag{5-12}$$

We define system characteristic frequency as:

$$\omega_c = \sqrt{\frac{f_m}{J_m}} \tag{5-13}$$

then the system characteristic time is:

$$T_c = \frac{1}{\omega_c} = \sqrt{\frac{J_m}{f_m}} \tag{5-14}$$

The non-dimensional time is defined as:

$$t^* = \frac{t}{T_c} \tag{5-15}$$

Then

$$t = T_c t^* \tag{5-16}$$

$$dt = T_c dt^* \tag{5-17}$$

(5-11) and (5-12) can be written as:

$$\frac{d^2 q_m}{(dt^*)^2} = -\frac{T_c^2 f_m}{J_m}\mathrm{sgn}(\frac{dq_m}{dt^*}) - \frac{T_c^2 r K_s}{J_m}(rq_m - q_l) + \frac{T_c^2 T_m}{J_m}$$

$$= -\mathrm{sgn}(\frac{dq_m}{dt^*}) - \frac{rK_s}{f_m}(rq_m - q_l) + \frac{T_m}{f_m} \tag{5-18}$$

$$\frac{d^2 q_l}{(dt^*)^2} = -\frac{T_c^2 f_l}{J_l}\mathrm{sgn}(\frac{dq_l}{dt^*}) + \frac{T_c^2 K_s}{J_l}(rq_m - q_l)$$

$$= -\frac{J_m f_l}{J_l f_m}\mathrm{sgn}(\frac{dq_l}{dt^*}) + \frac{J_m K_s}{J_l f_m}(rq_m - q_l) \tag{5-19}$$

We define following non-dimensional parameters:

$$K^* = \frac{K_s}{f_m} \tag{5-20}$$

$$J_l^* = \frac{J_l}{J_m} \tag{5-21}$$

$$f_l^* = \frac{f_l}{f_m} \tag{5-22}$$

$$\tau^* = \frac{T_m}{f_m} \tag{5-23}$$

$$r^* = r \tag{5-24}$$

The substitution of (5-20) to (5-24) in equations (5-18) and (5-19) yields:

$$\frac{d^2 q_m}{(dt^*)^2} = -\mathrm{sgn}(\frac{dq_m}{dt^*}) - r^* K_s^* (r^* q_m - q_l) + \tau^* \tag{5-25}$$

$$\frac{d^2 q_l}{(dt^*)^2} = -\frac{f_l^*}{J_l^*}\mathrm{sgn}(\frac{dq_l}{dt^*}) + \frac{K_s^*}{J_l^*}(r^* q_m - q_l) \qquad (5\text{-}26)$$

5.4.2 Friction variation

5.4.2.1 Simulation for friction effect on resolution

The load side friction level f_l^* is defined in equation (5-22).

Take 25 friction levels from 0.01 to 1. For different friction levels, we use 1000 pulse inputs to simulate the resolution as defined in section 4.5. A simulated histogram can be obtained. For example, the histograms for f_l^*=0.01, 0.1, 0.3 0.6 and 1 are plotted in Figure 5-24 through Figure 5-28.

The simulation demonstrates that when friction level is big, the arm can only move after a number of pulses are applied and the spring deformation has accumulated to a certain amount. This is because the spring potential energy must accumulate to a certain amount to overcome the friction. The higher the friction level, the bigger the potential energy needed to drive the arm's motion. The first step of the delta is very big, and then gets smooth afterwards, as shown in Figure 5-29. The potential energy is accumulated before the load starts moving. Once the load moves, the system's potential energy decreases just like an avalanche, as shown in Figure 5-30.

The friction and flexibility in harmonic drives create a hysteresis signature. The bigger the friction is, the more effect the hysteresis has. The simulated hysteresis curve for friction level f_l^* =0.01 and 0.1 are shown in Figure 5-31 and Figure 5-32.

For different friction levels, the maximum delta, median delta, and minimum delta are plotted in Figure 5-33 which shows that the resolution gets worse proportional to the friction level. We use the following equation to calculate the standard deviation:

$$\sigma = \sqrt{\frac{\sum_{i=1}^{N}(\delta_{average} - \delta_i)^2}{N-1}}$$

The standard deviation is plotted in Figure 5-34.

5.4.2.2 Experiment for friction effect on resolution

The following experiments are devised to verify the above simulation results:

We put a wedge under the output arm and push the wedge towards the arm to increase the load side friction. We then measure the friction f_l and calculate the friction level f_l^* using equation (5-22). The resolution is then tested in the different friction levels. The histograms are plotted in Figure 5-35 through Figure 5-38. The delta versus friction level is plotted in Figure 5-39. From this graph, we can see that the resolution is degraded linearly to the friction level. The experimental results are consistent with the simulation. The standard deviation is plotted in Figure 5-40.

From the last section and this section, we can conclude that friction does not only increase the dead zone, but also degrades the resolution. It is very important to decrease the friction in precision control systems.

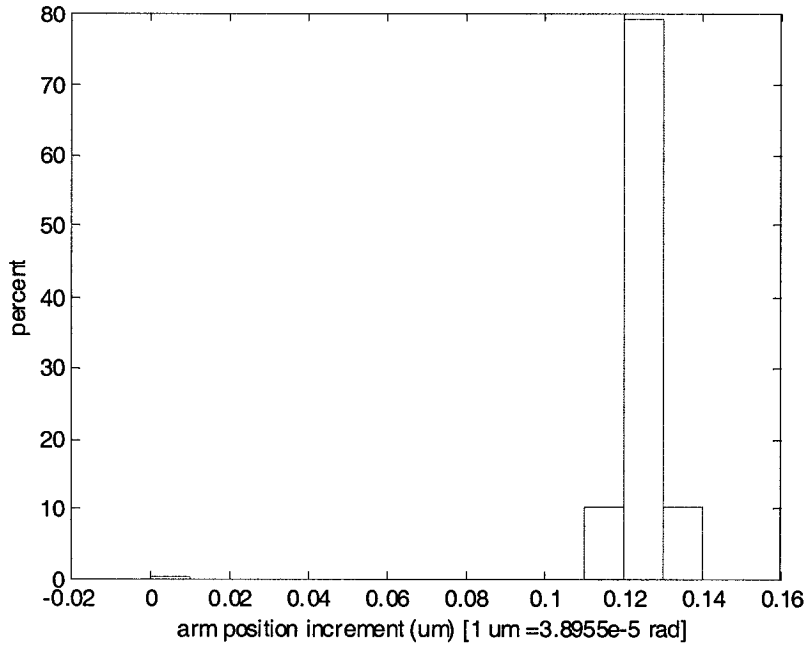

Figure 5-24 Simulation histogram for friction level f_l^*=0.01(1000 pulses)

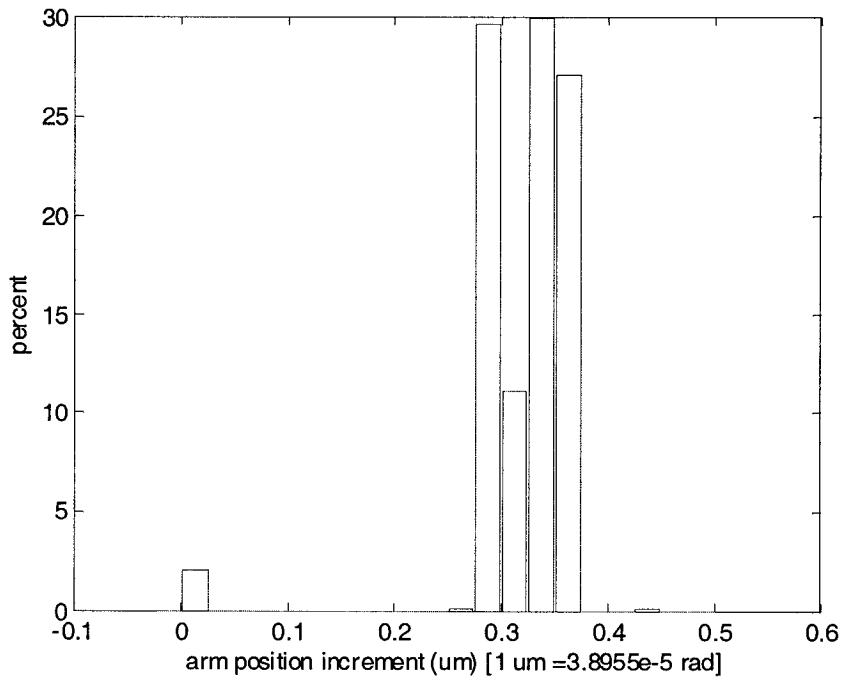

Figure 5-25 Simulation histogram for friction level f_l^*=0.1(1000 pulses) (There is one point at 2.139um)

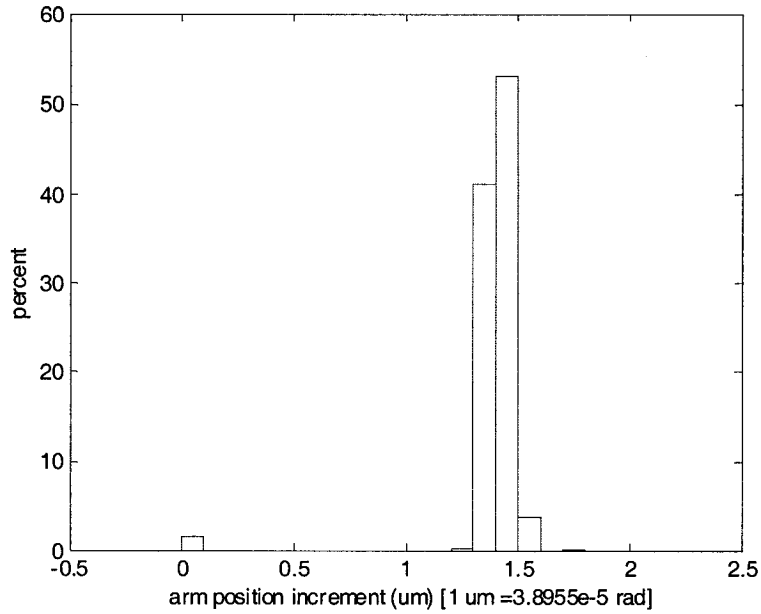

Figure 5-26 Simulation histogram for friction level $f_l^* = 0.3$(1000 pulses) (There is one point at 6.467um)

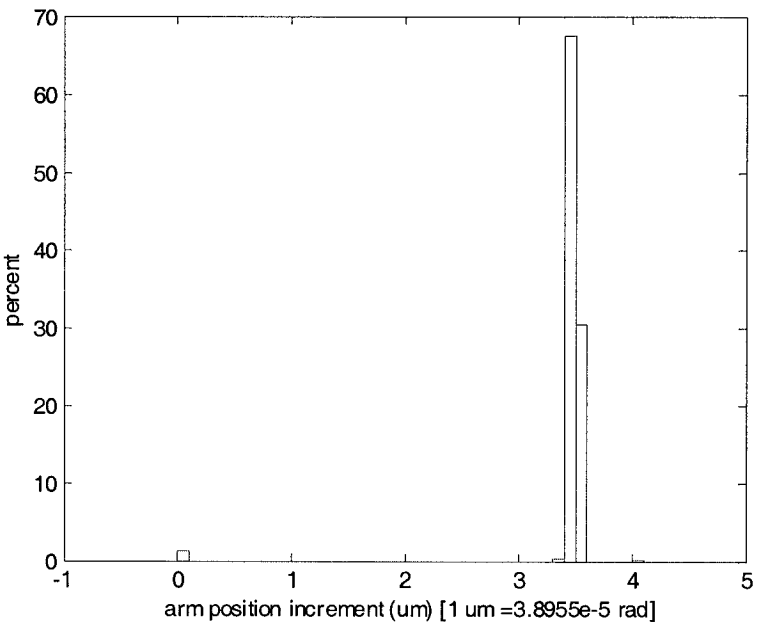

Figure 5-27 Simulation histogram for friction level $f_l^* = 0.6$ (1000 pulses) (There is one point at 12.972um)

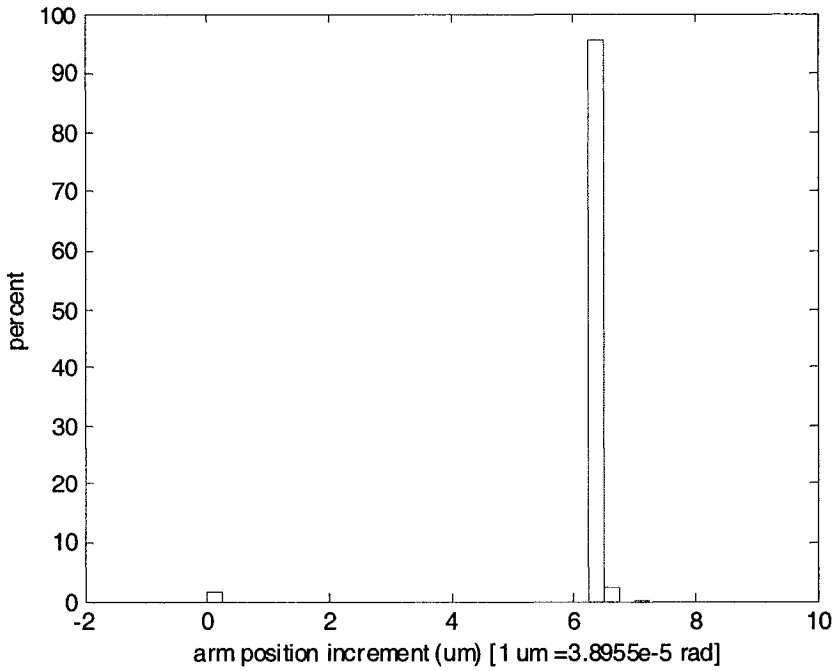

Figure 5-28 Simulation histogram for friction level $f_l^* = 1$ (1000 pulses) (There is one point at 21.648um)

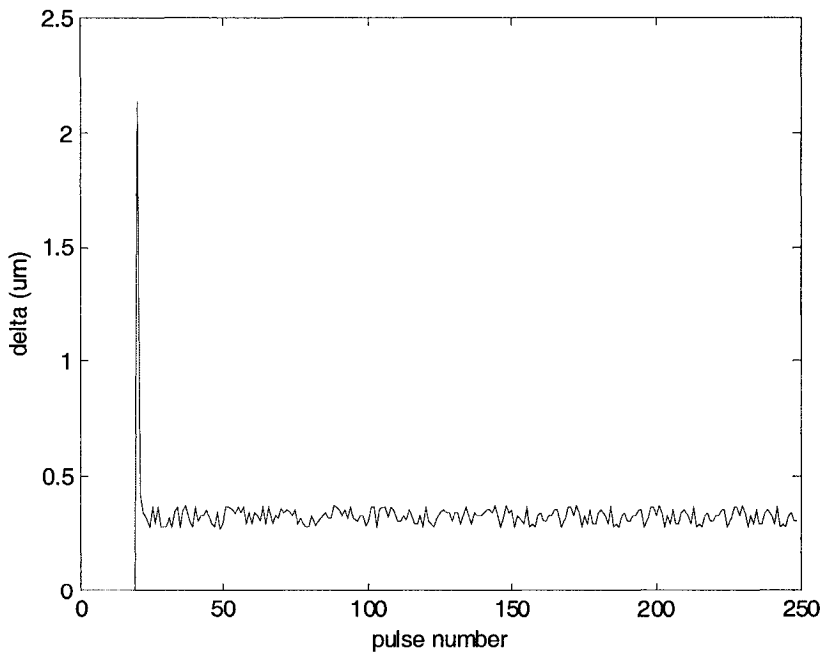

Figure 5-29 Delta versus pulse number, $f_l^* = 0.1$

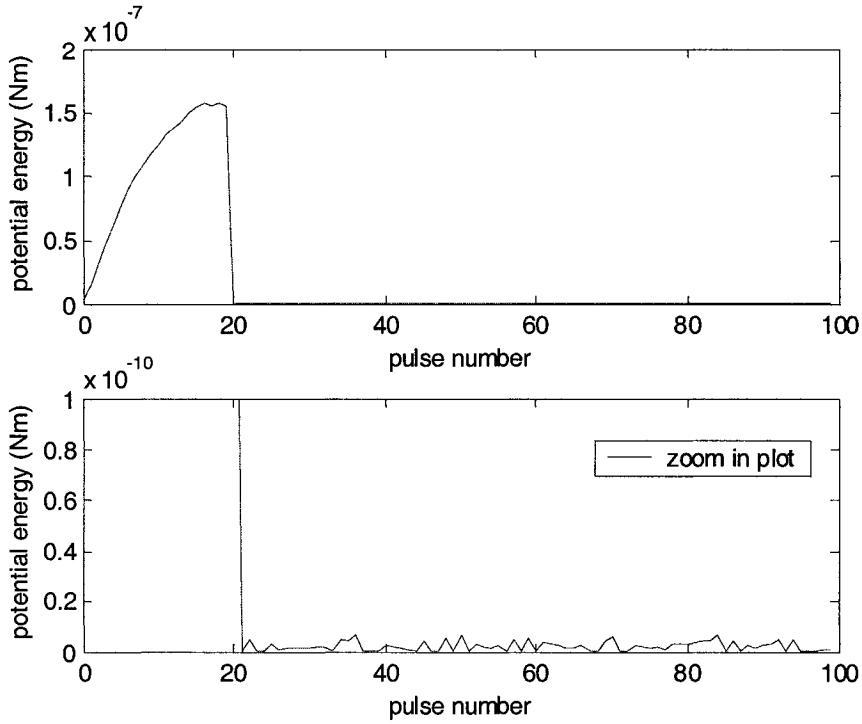

Figure 5-30 Potential energy $f_l^* = 0.1$

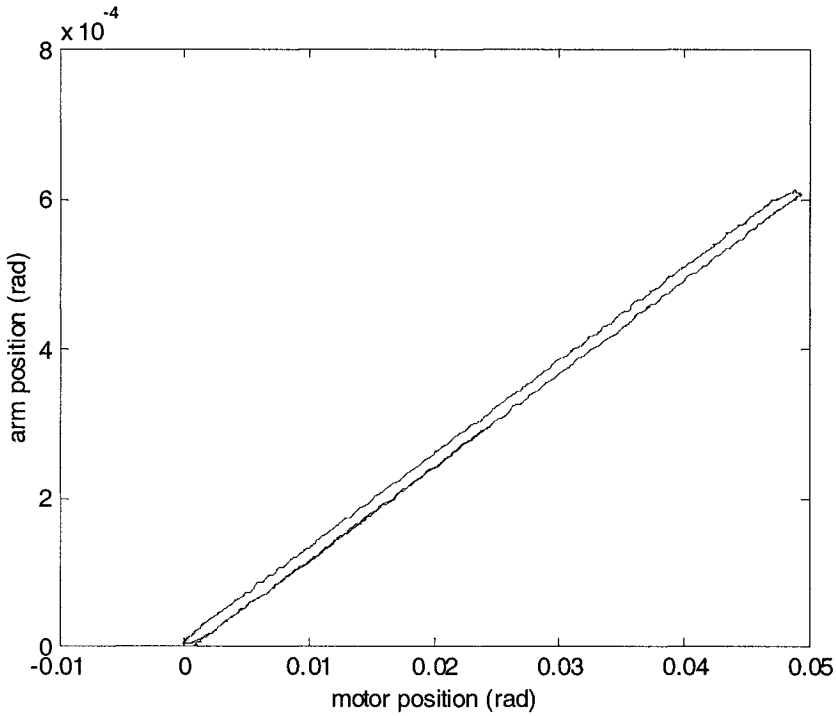

Figure 5-31 Hysteresis curve, $f_l^* = 0.01$

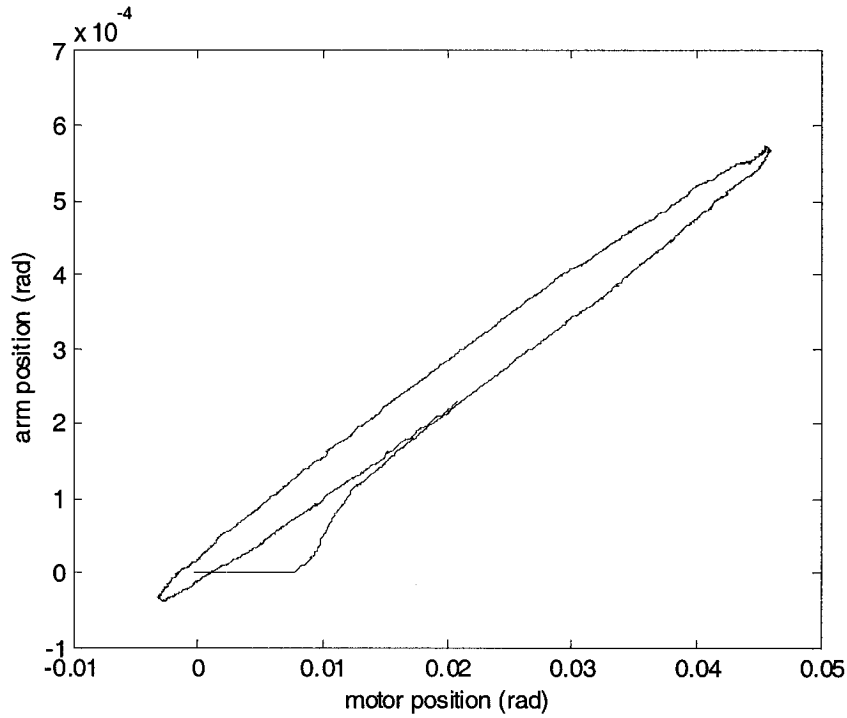

Figure 5-32 Hysteresis curve, $f_l^* = 0.1$

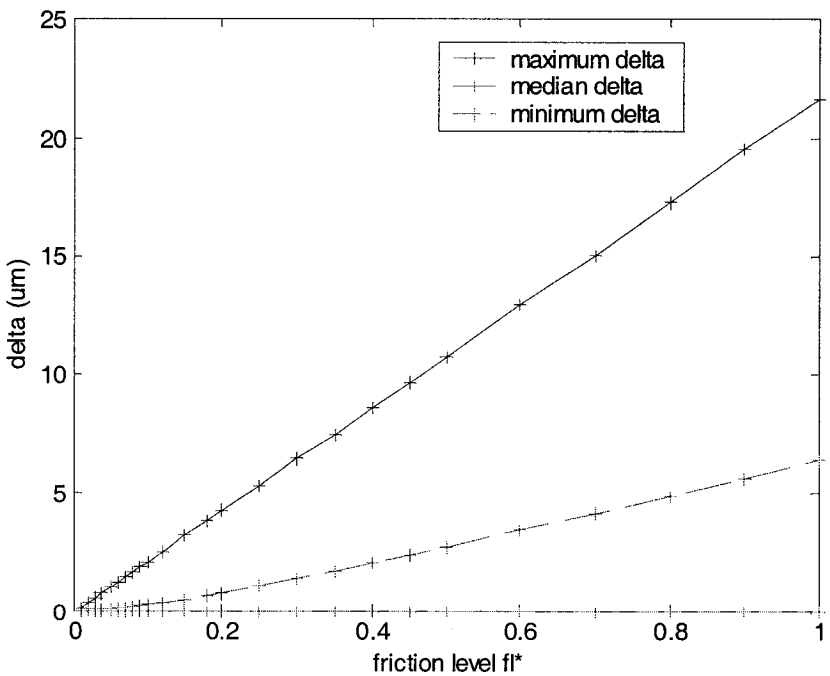

Figure 5-33 Delta versus friction level f_l^* (simulation)

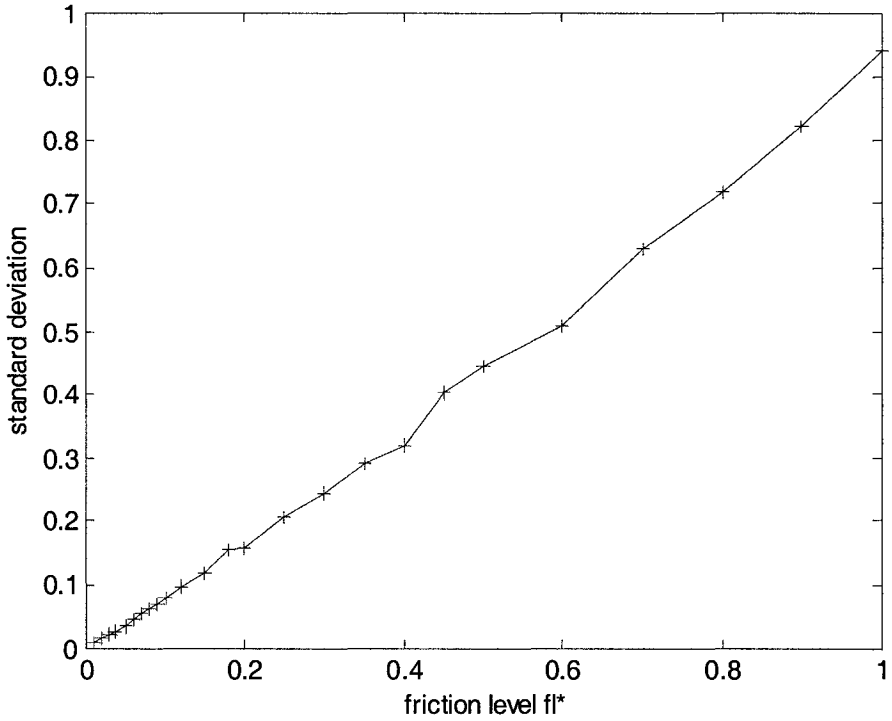

Figure 5-34 Standard deviation (simulation)

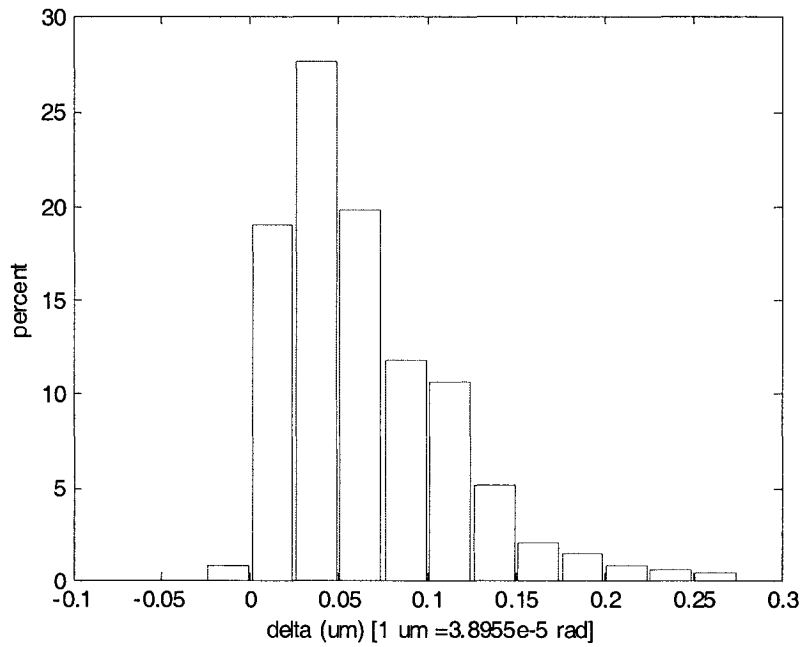

Figure 5-35 Experimental histogram for friction level $f_l^* = 0.176$

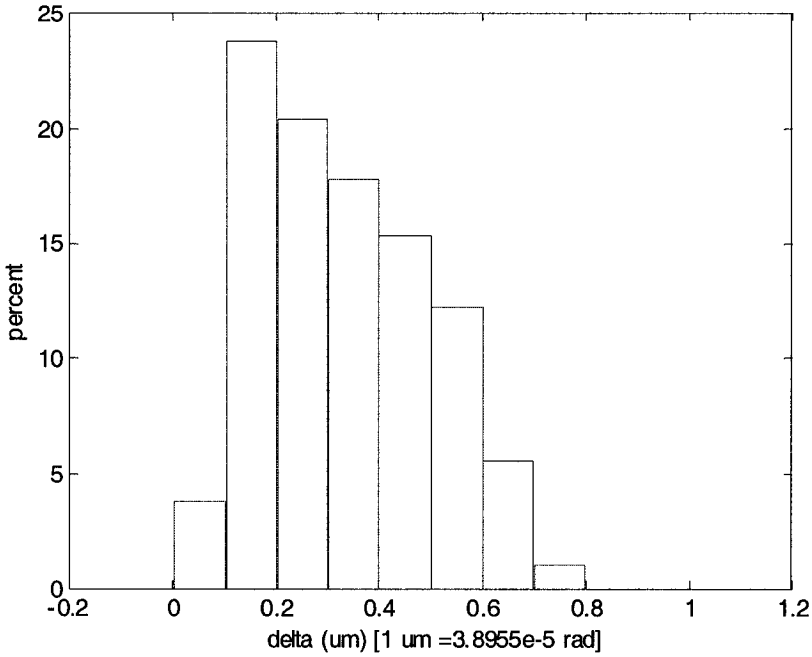

Figure 5-36 Experimental histogram for friction level $f_l^* = 0.311$

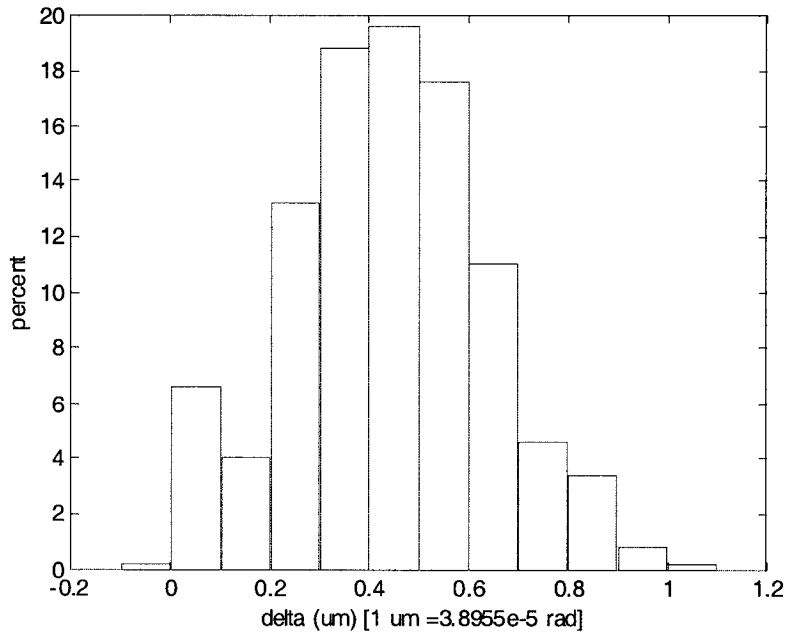

Figure 5-37 Experimental histogram for friction level $f_l^* = 0.391$

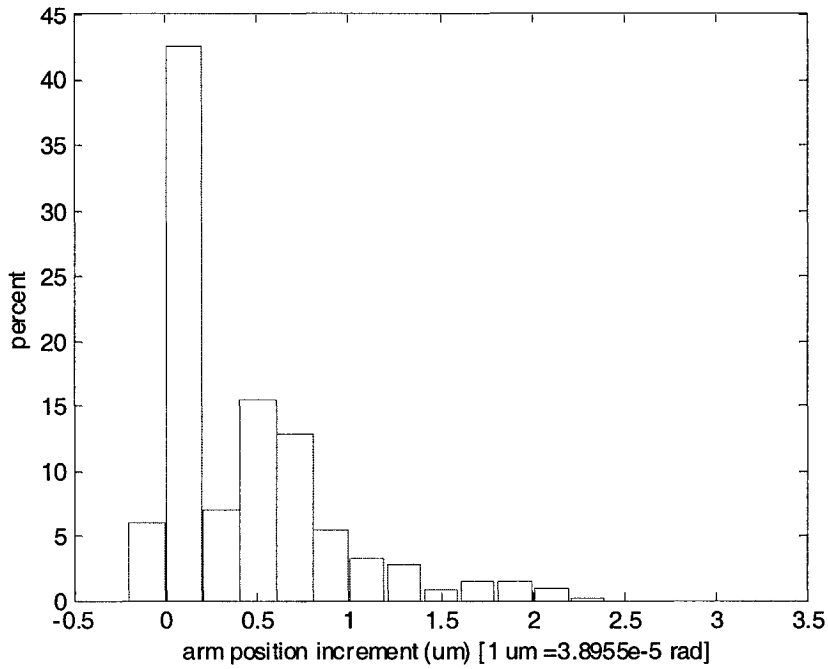

Figure 5-38 Experimental histogram for friction level f_l^* =0.703

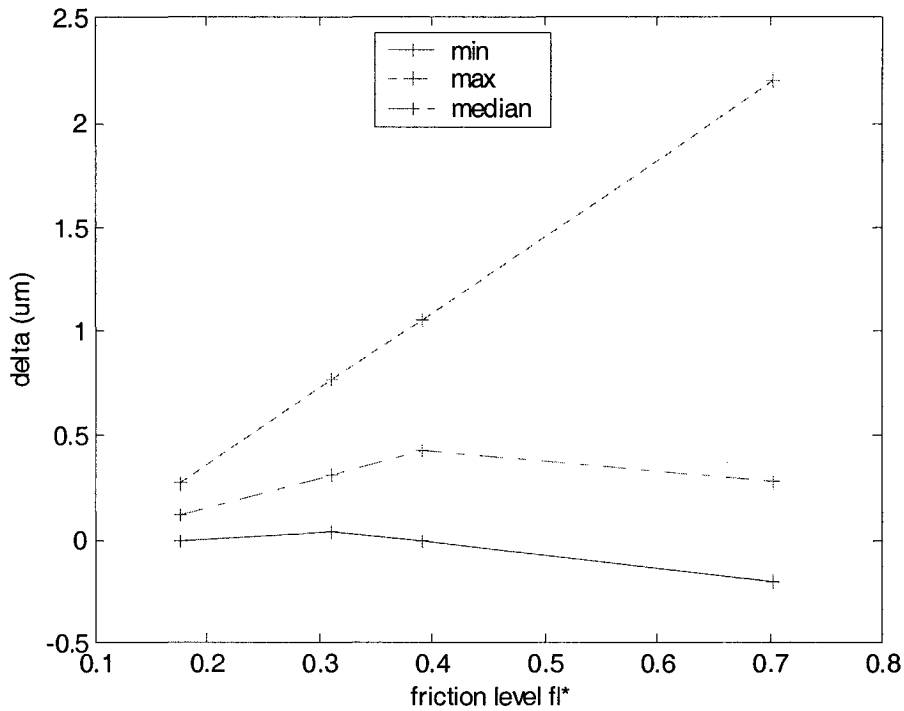

Figure 5-39 Delta versus friction level f_l^* (experiment)

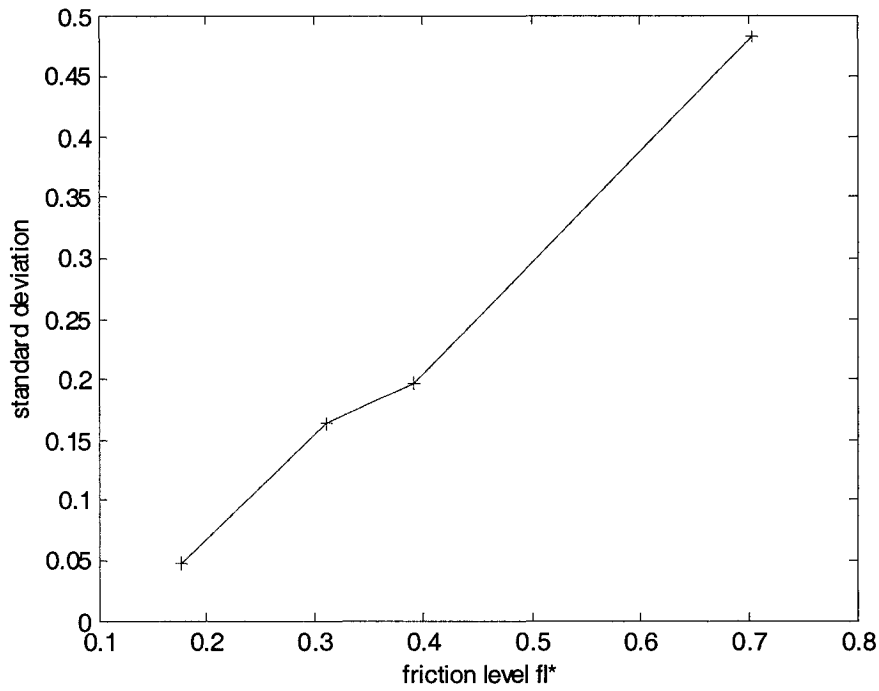

Figure 5-40 Standard deviation (experiment)

5.4.3 Flexibility variation

5.4.3.1 Simulation of effect of flexibility on resolution

K^* has been defined in (5-20). For K^* = 520.8, 730, 1050.4, 1250, and 1458.3, we simulate the resolution as defined in Section 4.5. The histogram is shown in Figure 5-41 through Figure 5-45. The resolution is plotted in Figure 5-46. It is apparent that the resolution improves as the spring constant increases. The standard deviation is plotted in Figure 5-47.

5.4.3.2 Simulation for effect of flexibility on dead zone

For each K^*, a different pulse amplitude can be used to simulate the arm

displacement (delta) response. For each of the pulse amplitudes, 1000 pulses are applied. The simulated delta responses are shown in Figure 5-48 through Figure 5-50. When K^* increases, the dead zone does not change at first. When K^* gets big enough, the maximum and minimum value of delta get close to each other. That means the arm moves more consistently.

From the above analysis, we can see that the resolution gets worse when the flexibility in harmonic drives is bigger (K^* is small). The flexibility also makes the arm's motion inconsistent. Therefore, the flexibility in harmonic drive degrades the performance of impulse control.

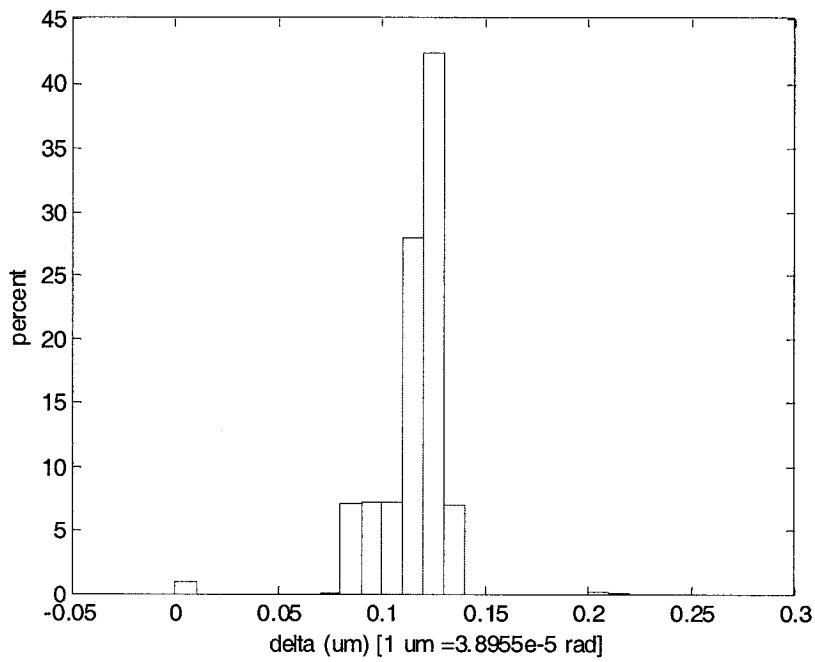

Figure 5-41 Simulation histogram for K^*=520.8 (1000 pulses) (There is one point at 1.348 um)

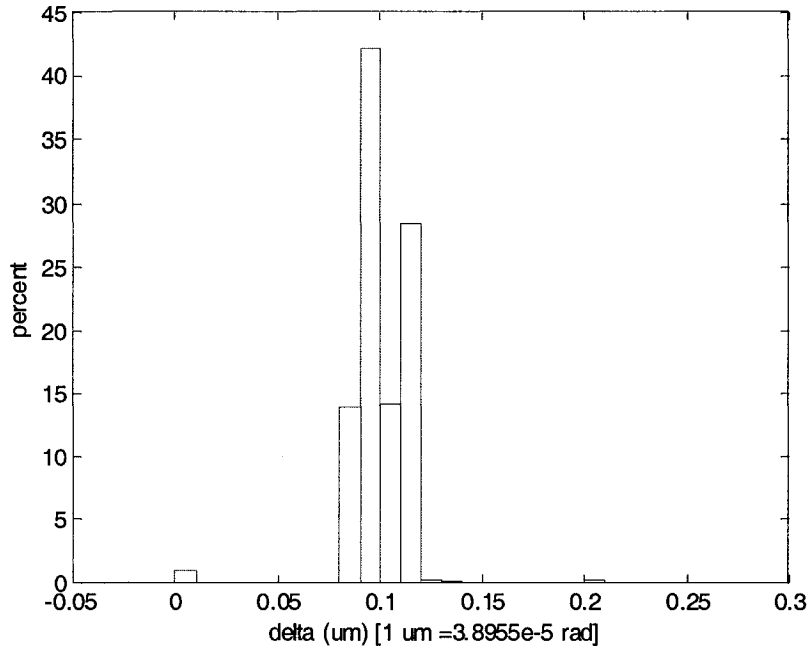

Figure 5-42 Simulation histogram for K^*=730 (1000 pulses) (There is one point at 1.093 um)

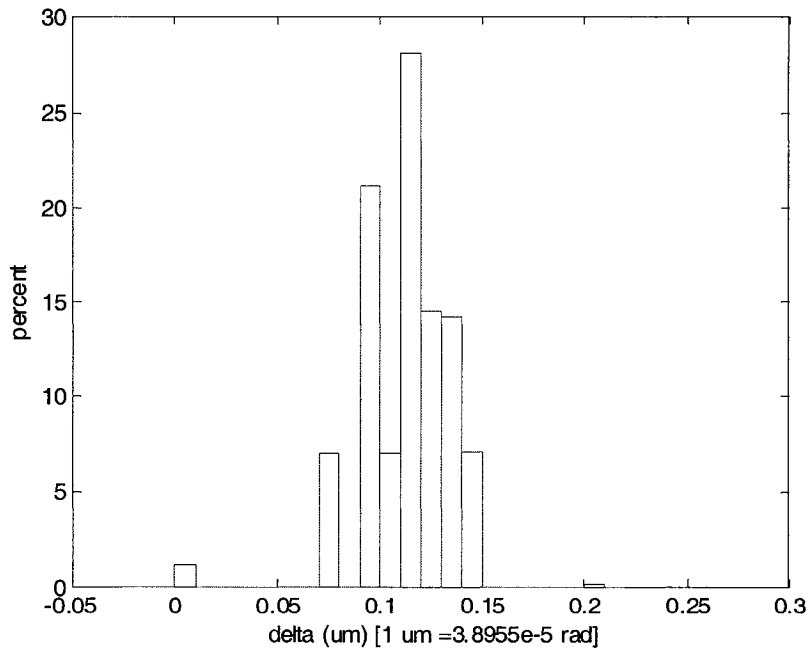

Figure 5-43 Simulation histogram for K^*=1050.4 (1000 pulses) (There is one point at 0.732 um)

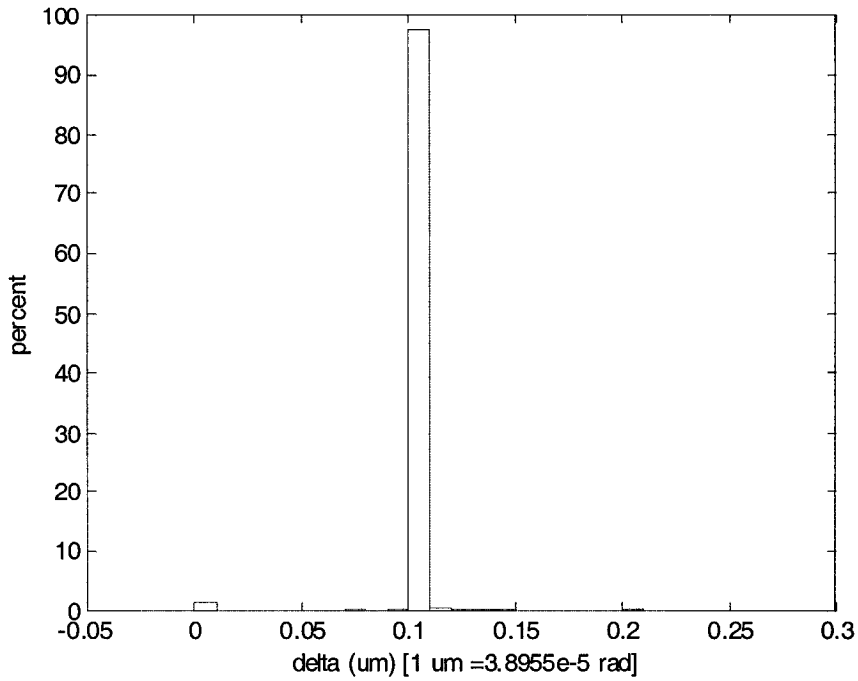

Figure 5-44 Simulation histogram for K^*=1250 (1000 pulses) (There is one point at 0.61 um)

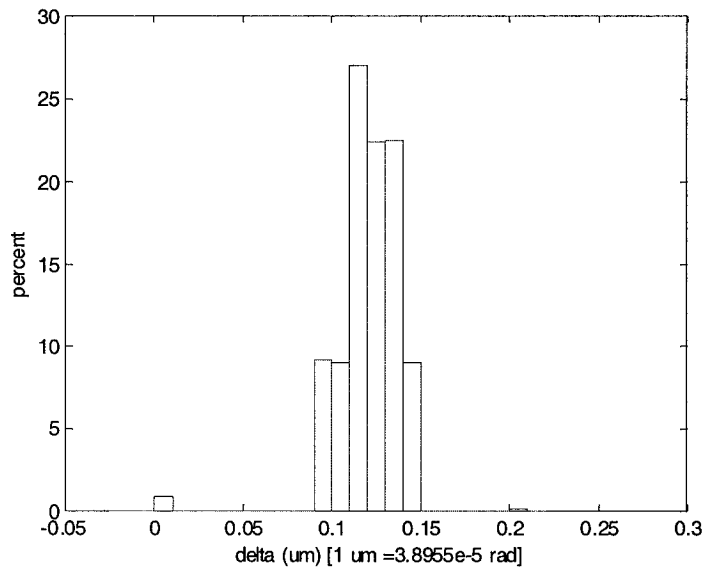

Figure 5-45 Simulation histogram for K^*=1458.3 (1000 pulses) (There is one point at 0.526 um)

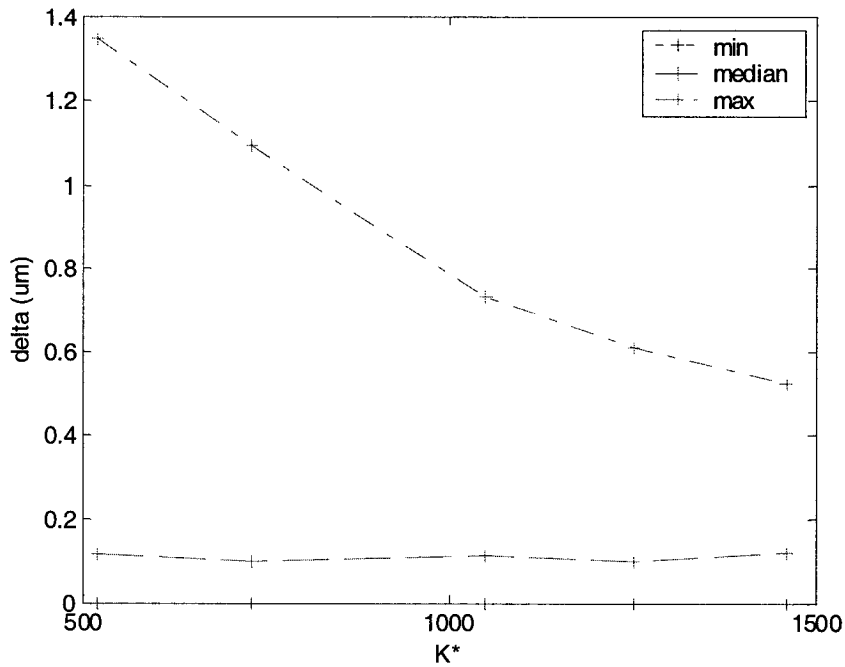

Figure 5-46 Delta versus flexibility

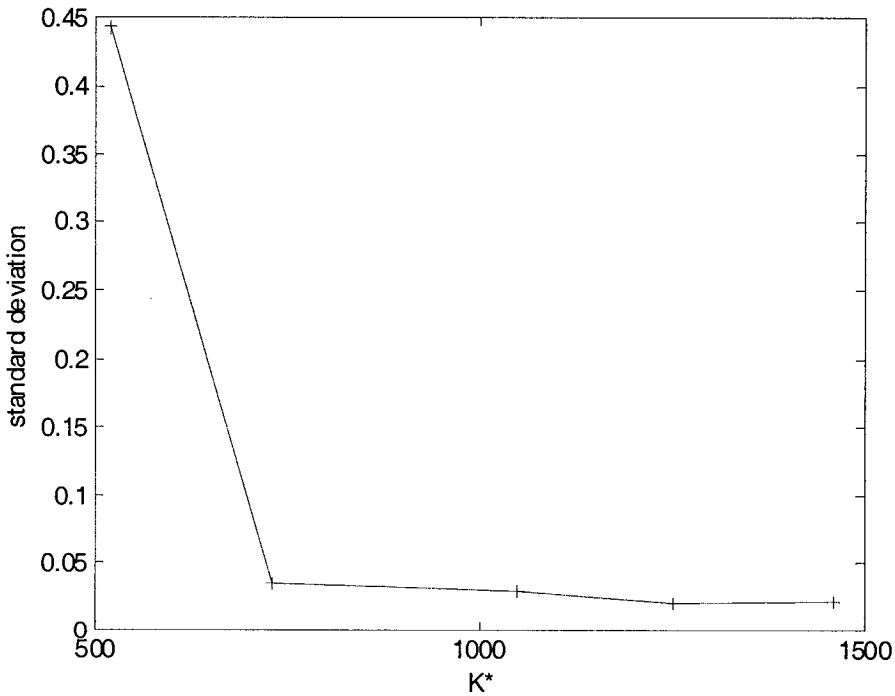

Figure 5-47 Standard deviation

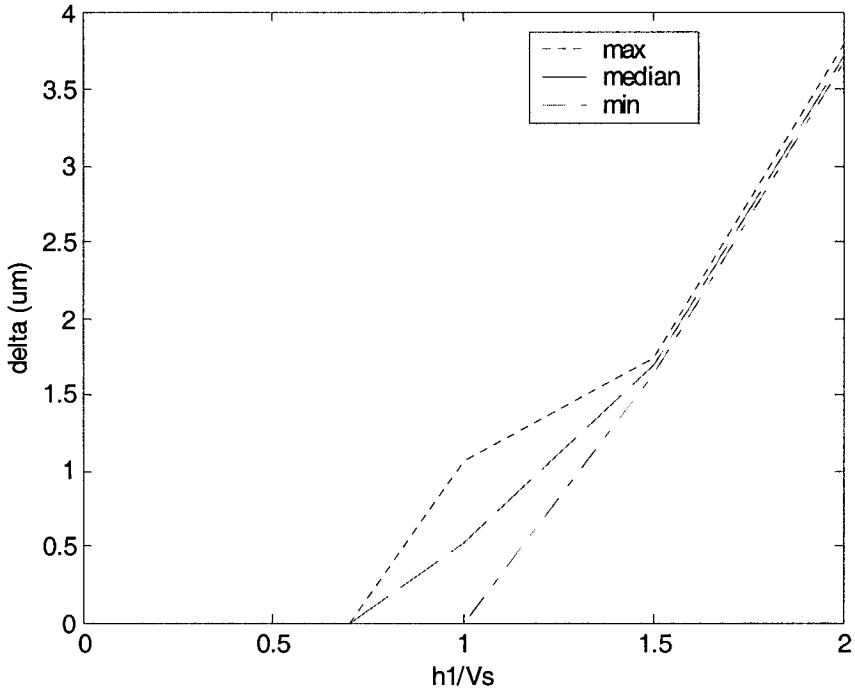

Figure 5-48 Simulation of dead zone for K^*=729

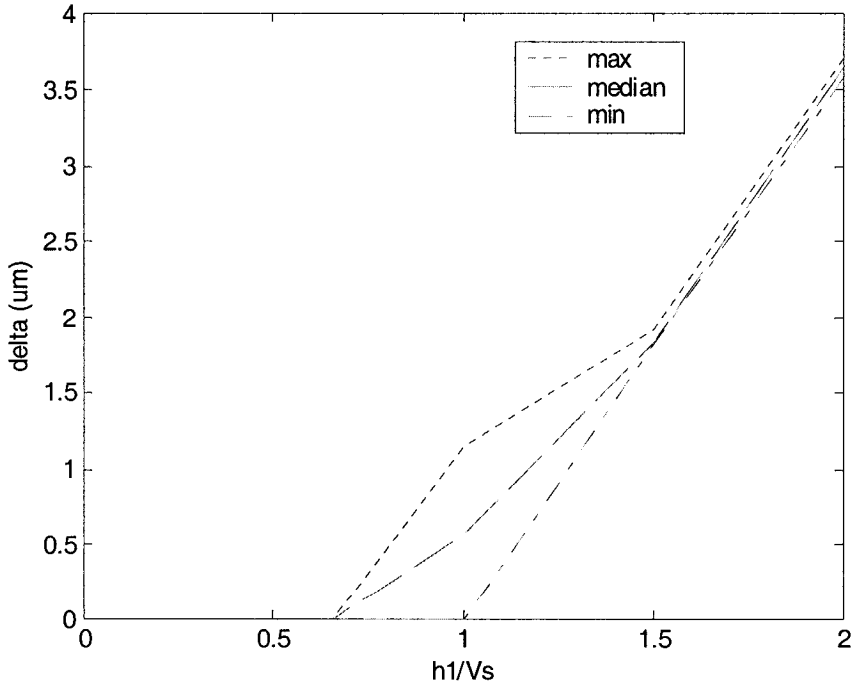

Figure 5-49 Simulation of dead zone for K^*=1042

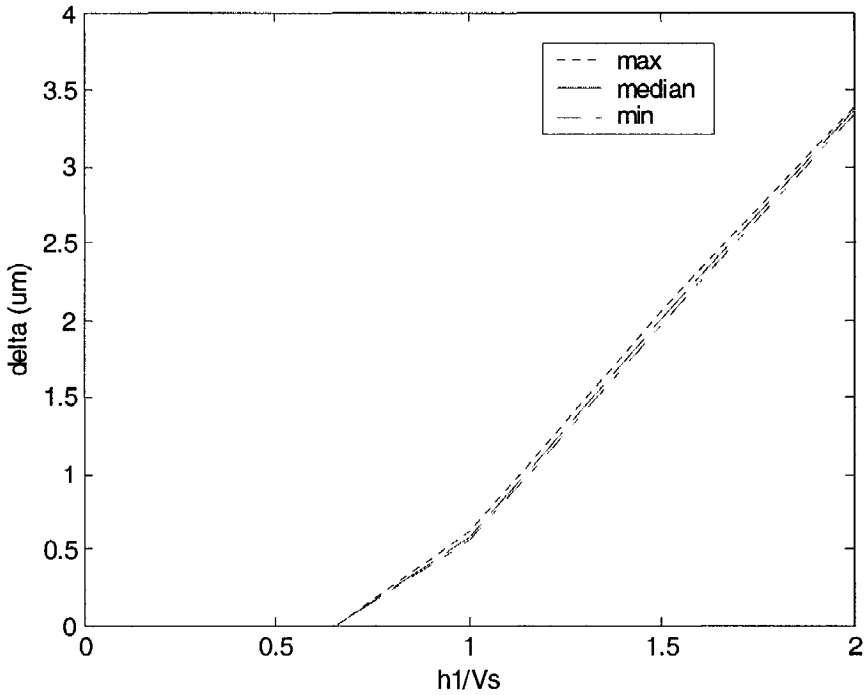

Figure 5-50 Simulation of dead zone for K^*=1354

5.4.4 Load inertia variation

5.4.4.1 Simulation for effect of load inertia on resolution

For different load inertias, calculation of J_l^* has been defined in (5-21). The simulated histograms are shown in Figures 5-51 through 5-57. The resolution improves slightly with an increase of J_l^*, as shown in Figure 5-58. The standard deviation is plotted in Figure 5-59.

5.4.4.2 Simulation for effect of load inertia on dead zone

For different values of J_l^*, the dead zone is simulated in Figure 5-60 through Figure 5-66. It is evident that the load inertia has almost no effect on the dead zone.

The above analysis shows that the load side inertia has less effect on impulse control. When load inertia increases, the resolution improves slightly, and it has almost no effect on the dead zone.

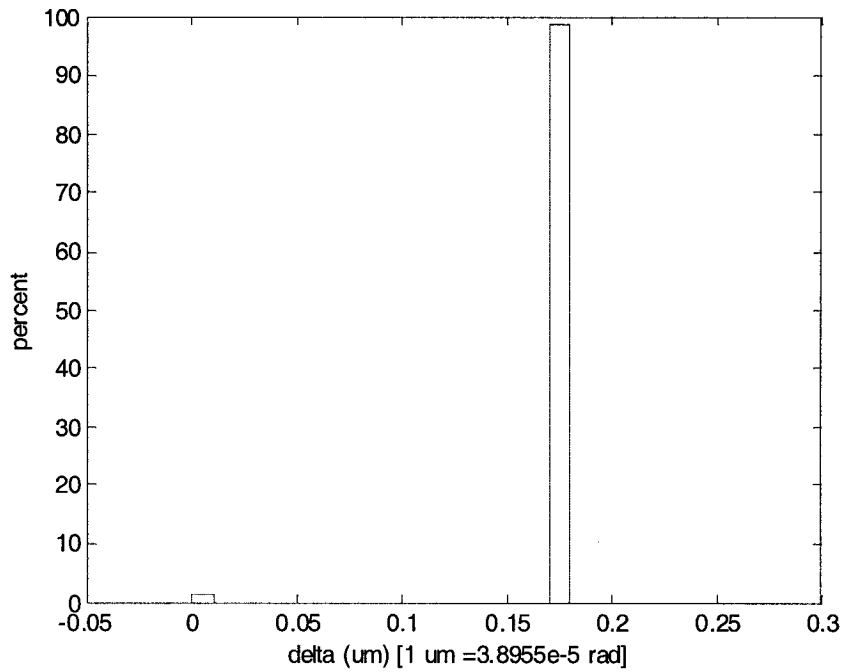

Figure 5-51 Simulation of histogram for J_l^*=100 (There is one point at 0.856um)

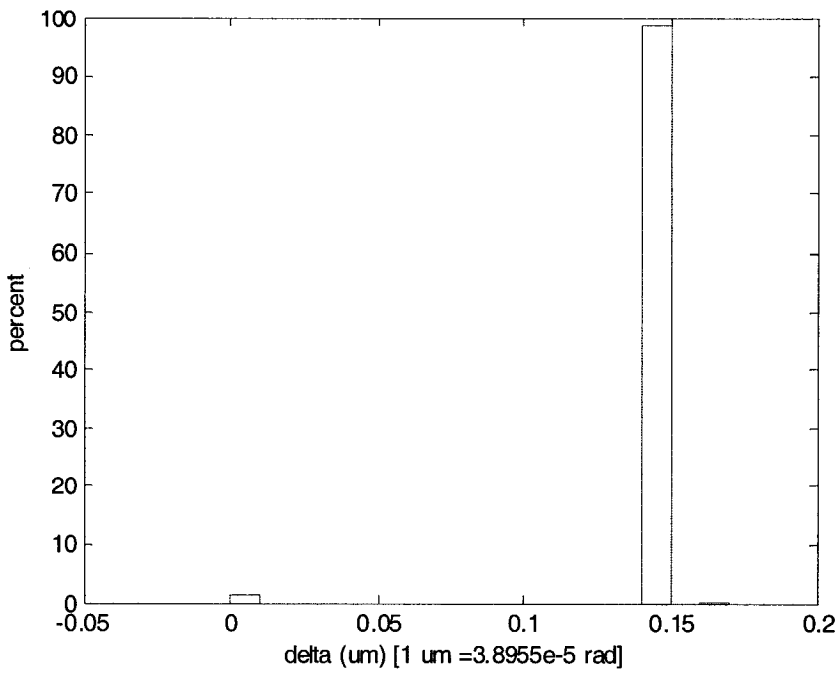

Figure 5-52 Simulation of histogram for J_l^*=200 (There is one point at 0.822um)

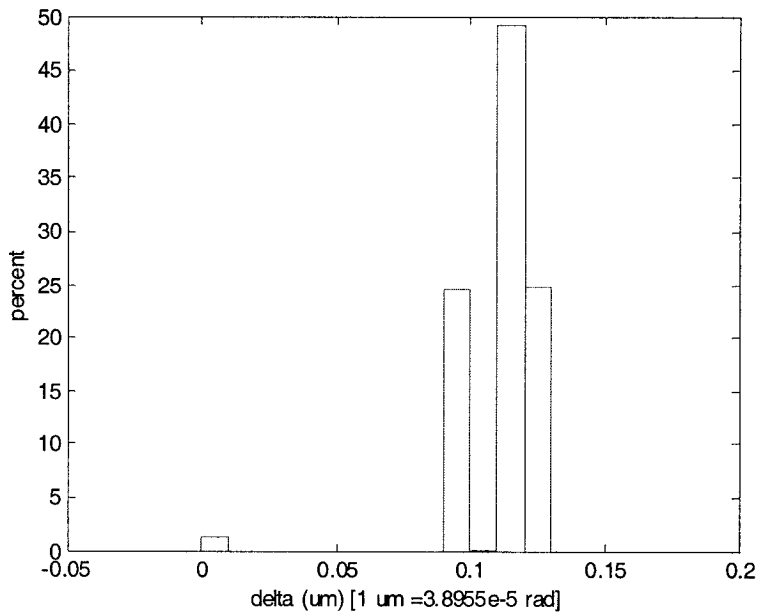

Figure 5-53 Simulation of histogram for J_l^*=300 (There is one point at 0.797um)

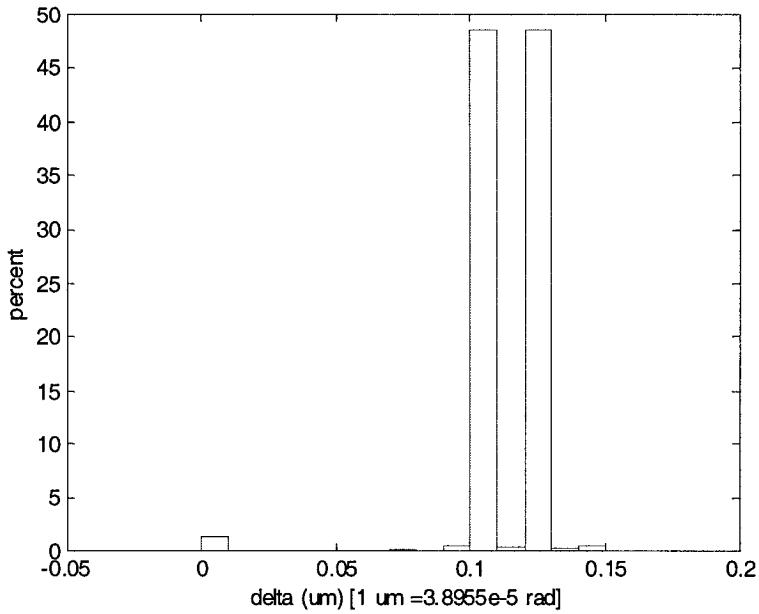

Figure 5-54 Simulation of histogram for J_l^*=400 (There is one point at 0.762um)

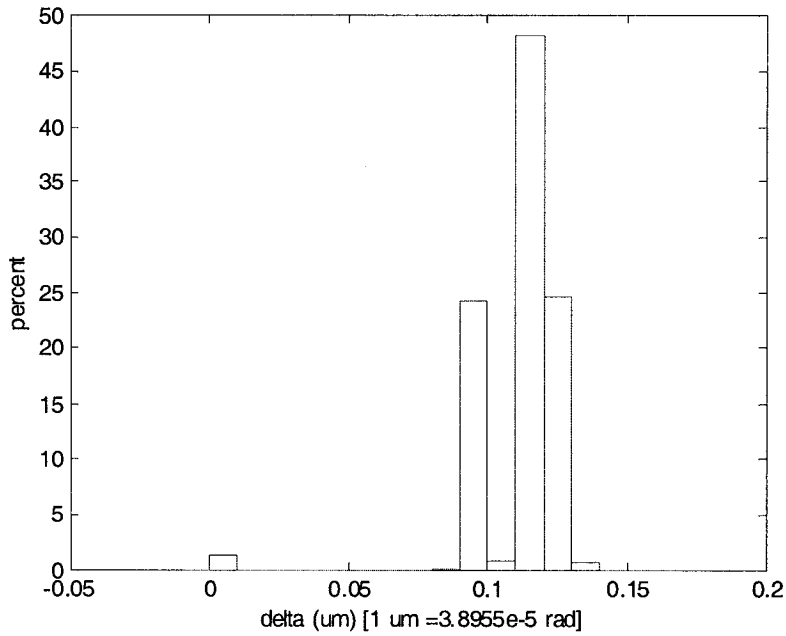

Figure 5-55 Simulation of histogram for J_l^*=500 (There is one point at 0.745um)

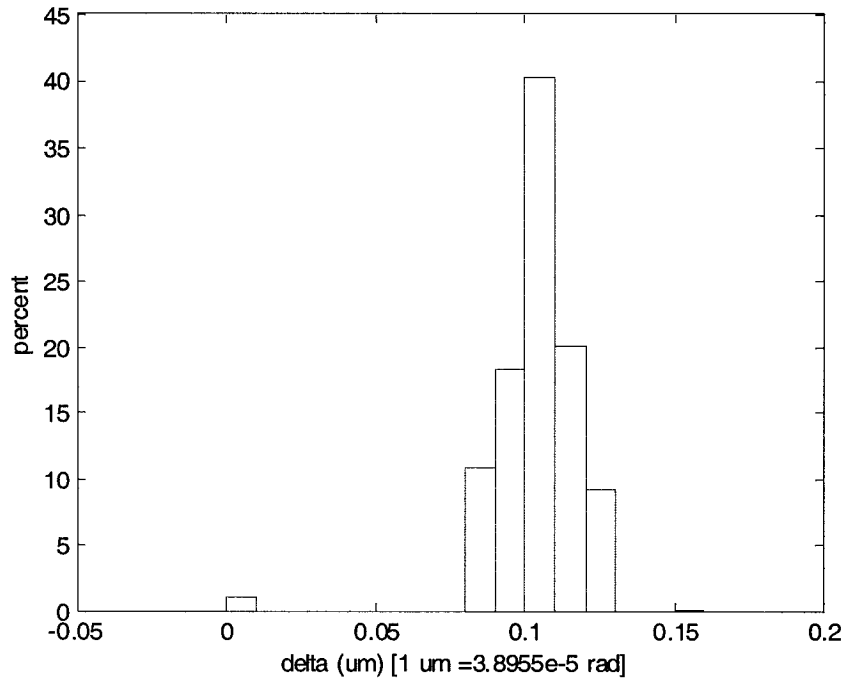

Figure 5-56 Simulation of histogram for J_l^*=600 (There is one point at 0.743um)

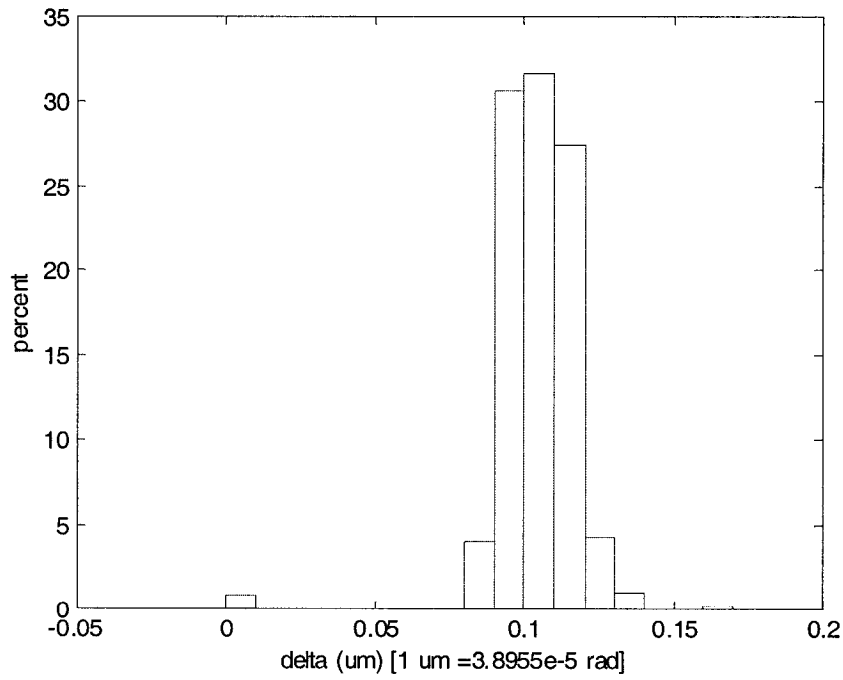

Figure 5-57 Simulation of histogram for J_l^*=700 (There is one point at 0.671um)

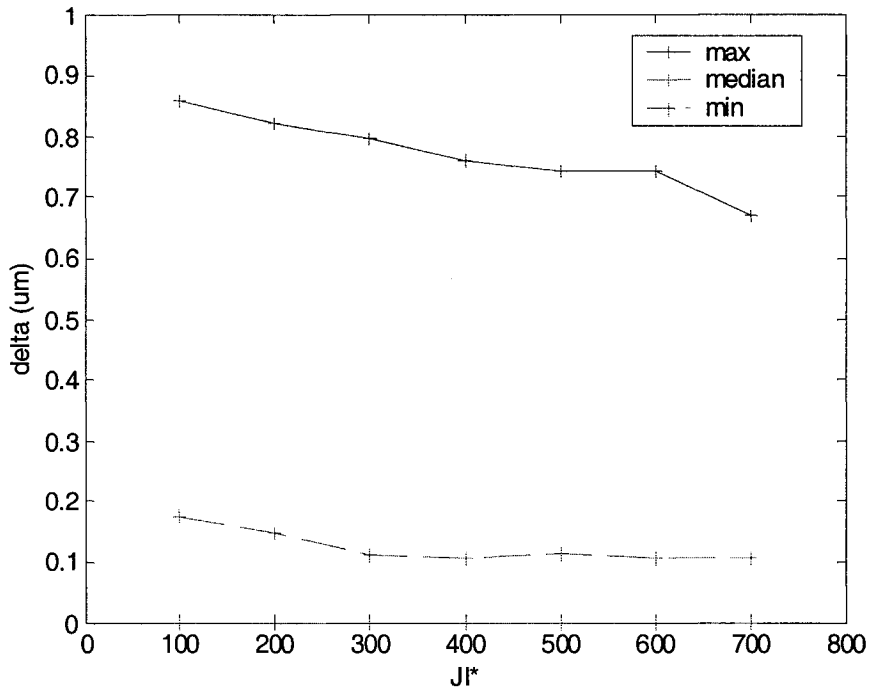

Figure 5-58 Simulation of resolution versus J_l^*

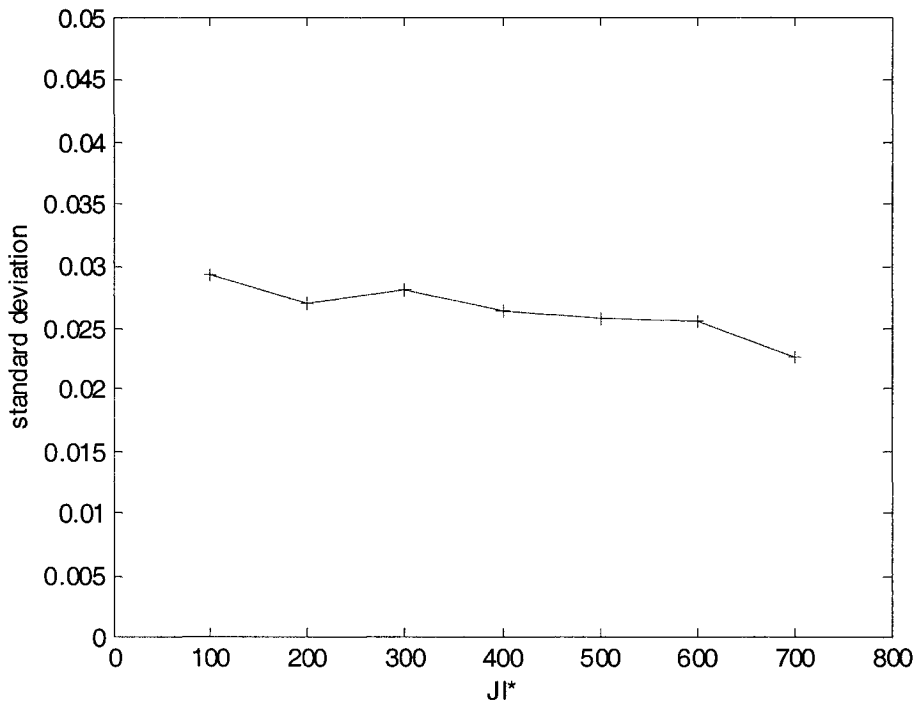

Figure 5-59 Simulation of standard deviation versus J_l^*

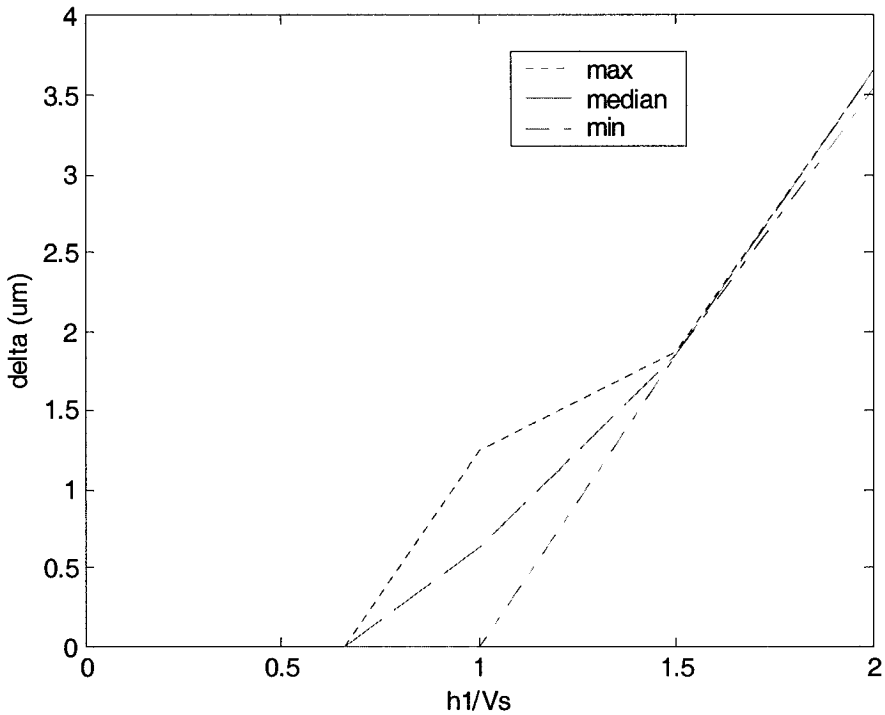

Figure 5-60 Simulation of dead zone for J_l^*=100

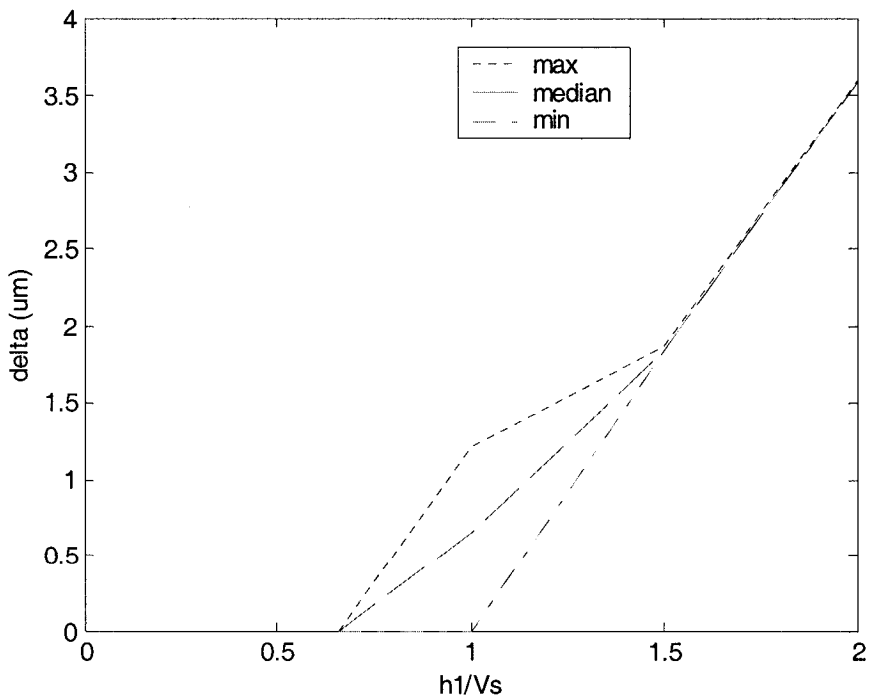

Figure 5-61 Simulation of dead zone for J_l^*=200

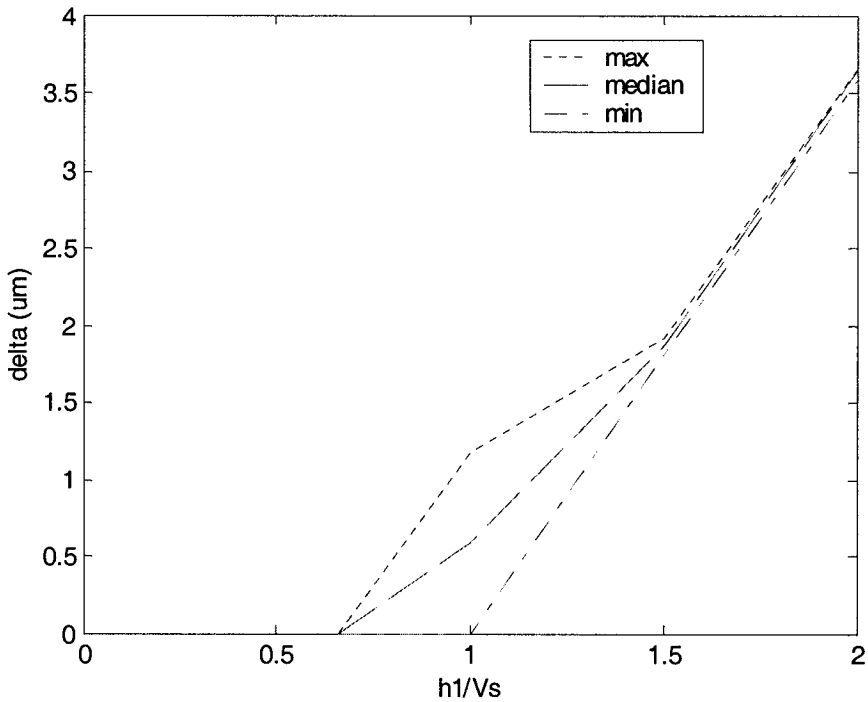

Figure 5-62 Simulation of dead zone for J_l^*=300

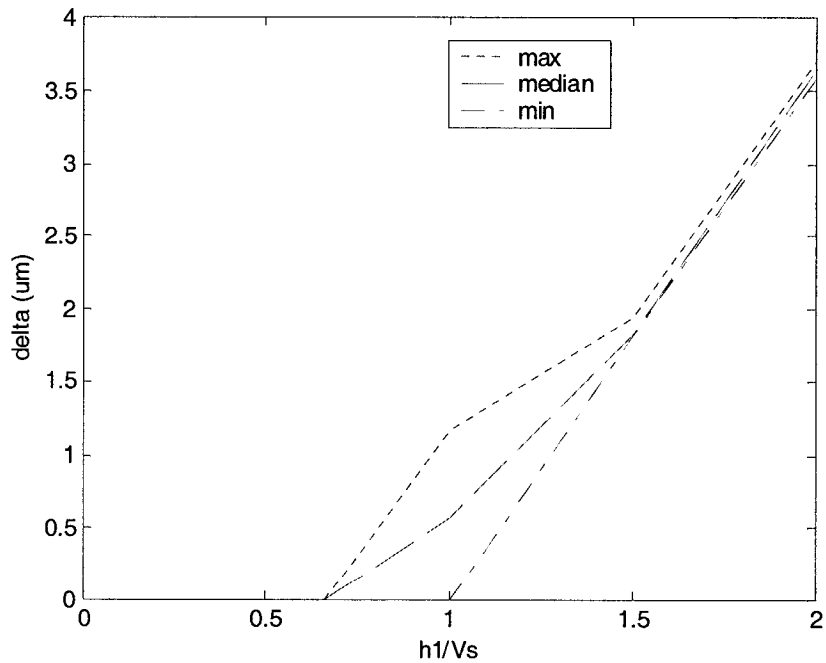

Figure 5-63 Simulation of dead zone for J_l^*=400

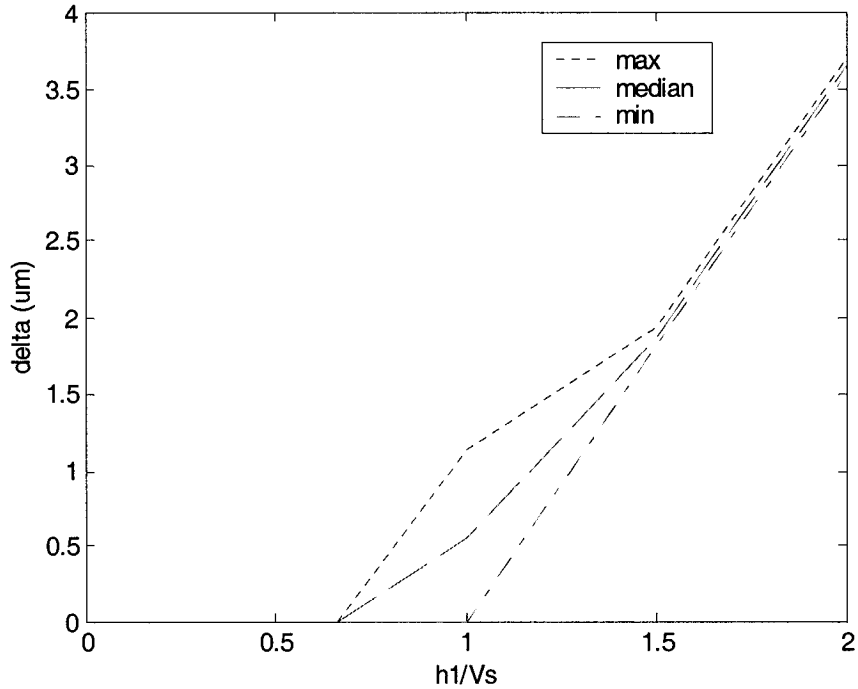

Figure 5-64 Simulation of dead zone for J_l^*=500

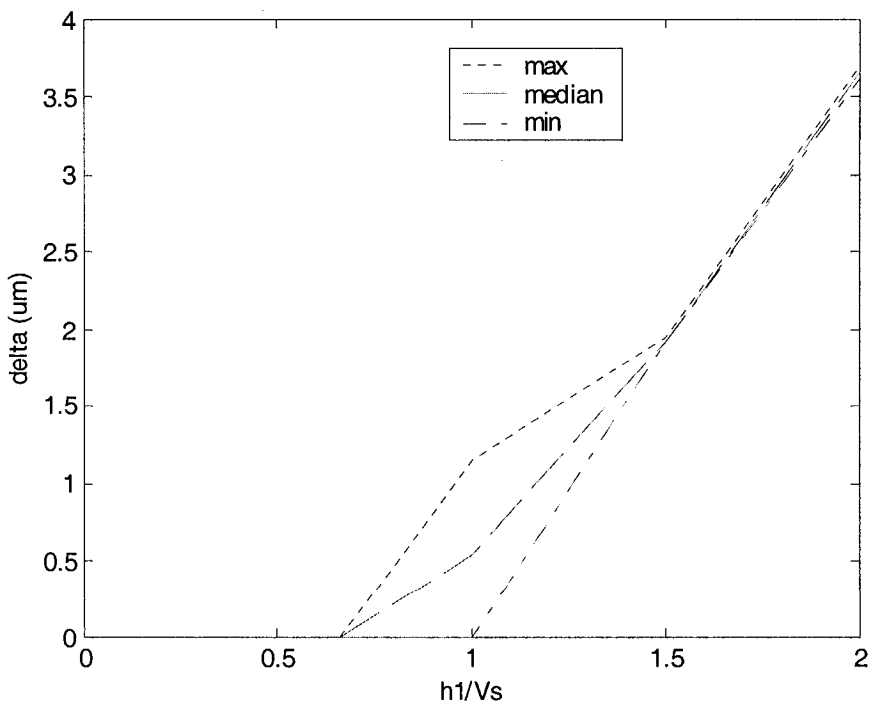

Figure 5-65 Simulation of dead zone for J_l^*=600

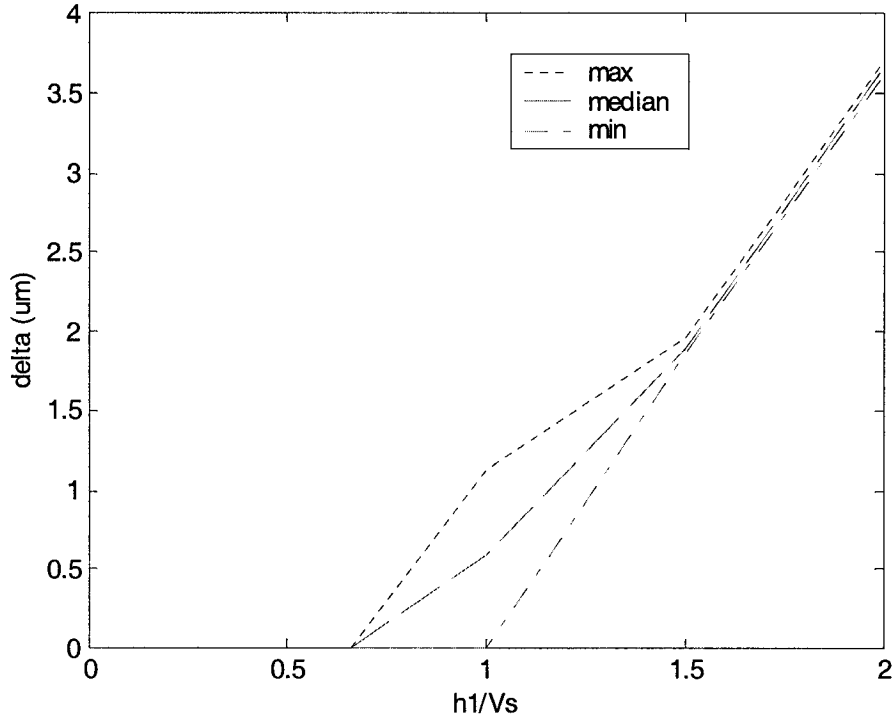

Figure 5-66 Simulation of dead zone for J_l^*=700

5.5 Adaptive impulse control

5.5.1 Adaptive impulse controller

Since the friction uncertainty exists, the coefficient b in equation (4-23) is not a constant in a real system. It may vary with position dependent friction. As an attempt to reduce the settling time in impulse control, an adaptive controller is developed as follows.

Let

$$a = \frac{1}{b} \tag{5-27}$$

the control law of equation (4-28) can be written as,

$$u_p(k+1) = K_c a[k] e[k] \tag{5-28}$$

We use the model reference adaptive controller (MRAC) developed in [32]:

$$a[k] = a[k-1] + Fe[k-1]\varepsilon[k] \tag{5-29}$$

$$\varepsilon[k] = \frac{K_c e[k-1] - d[k]}{1 + Ke^2[k-1]} \tag{5-30}$$

The block diagram of adaptive control based on the MRAC approach is depicted in Figure 5-67.

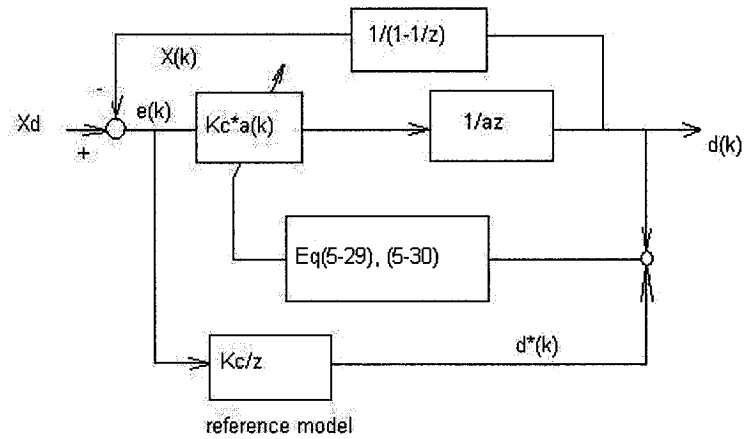

Figure 5-67 Block diagram of adaptive control system

5.5.2 Adaptive control simulation

For the previous adaptive controller, the simulation results for x_d=100um and x_d= -100um are shown in Figure 5-68 and Figure 5-69.

5.5.3 Experimental testing

We choose K = 0, K_c = 0.5 and F = 1.0e-3. The experimental results for x_d =100um and x_d = -100um are shown in Figure 5-70 and Figure 5-71 which

demonstrate that it can get the tracking error of the system resolution (0.3um). The settling time is about 0.6s. It is faster than an impulse feedback control.

The parameter tracking performance for different initial values is shown in Figure 5-72. The conclusion is that the parameter converges. The converged values have a small difference between them that may be caused by the different initial position.

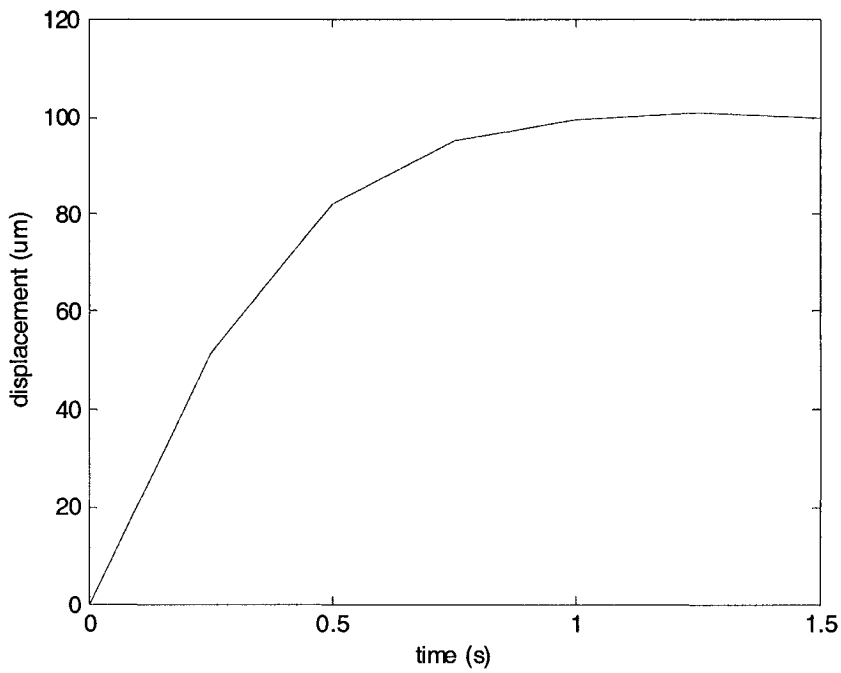

Figure 5-68 Adaptive impulse control simulation x_d=100um

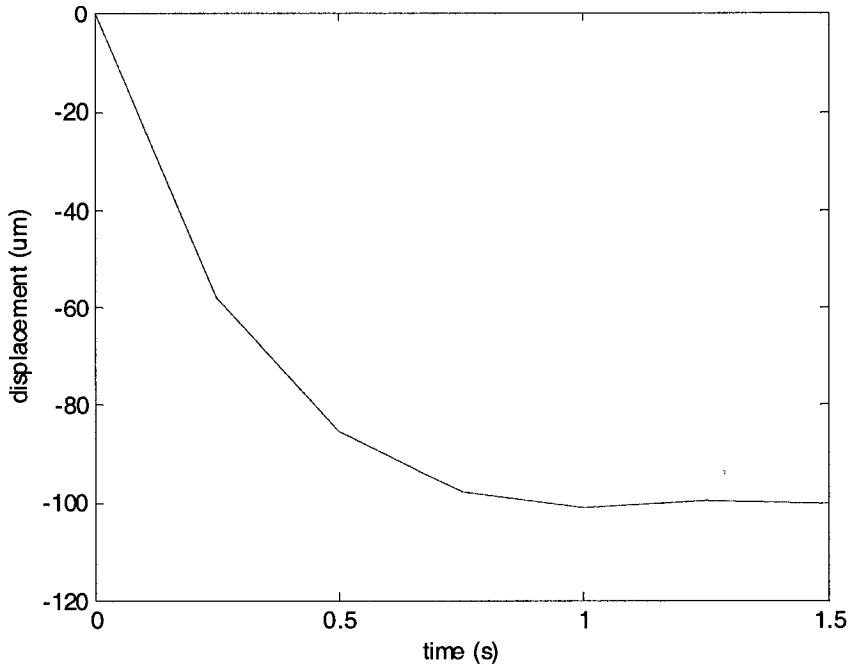

Figure 5-69 Adaptive impulse control simulation x_d=-100um

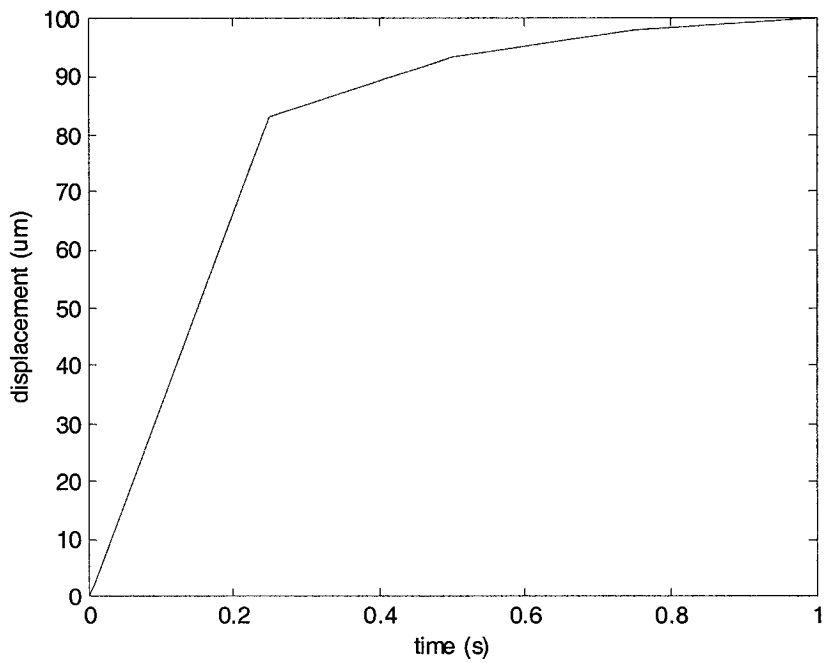

Figure 5-70 Adaptive impulse control experimental response x_d=100um

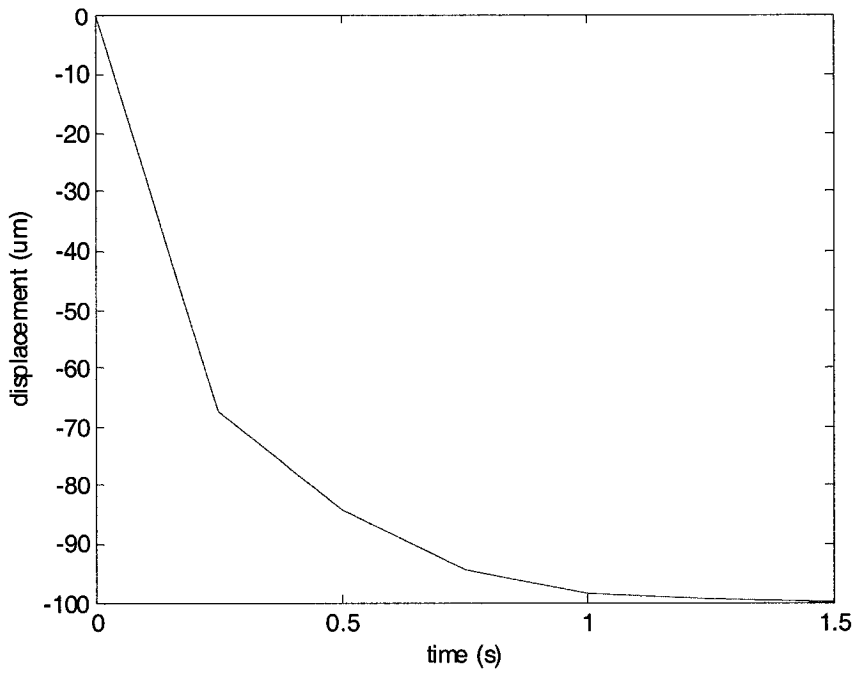

Figure 5-71 Adaptive impulse control experimental response x_d=-100um

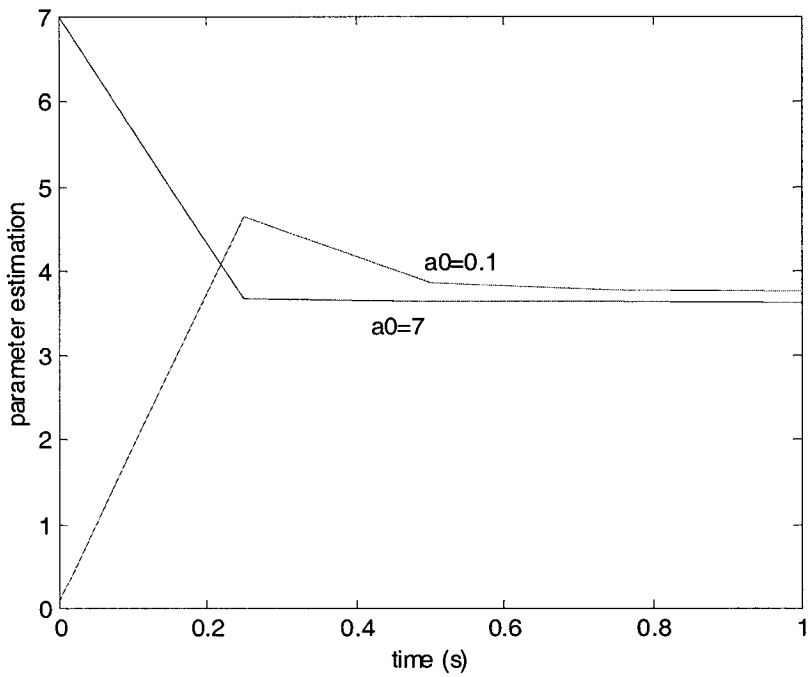

Figure 5-72 Parameter estimation performance

5.5.4 Friction variation

In this adaptive control, h_2 is just set to eliminate the dead zone. That is, h_2= 3.1278Vs in simulation and h_2=3.2Vs in experiment. If the load side friction varies, for example, if f_l increases from 0.0018Nm to 0.005Nm, we see a steady state error of 1um occurring as put forth in the simulation results shown in Figure 5-73,. This happens because when the load side friction increases, the dead zone appears again. The experiment shown in Figure 5-74 also verifies this result.

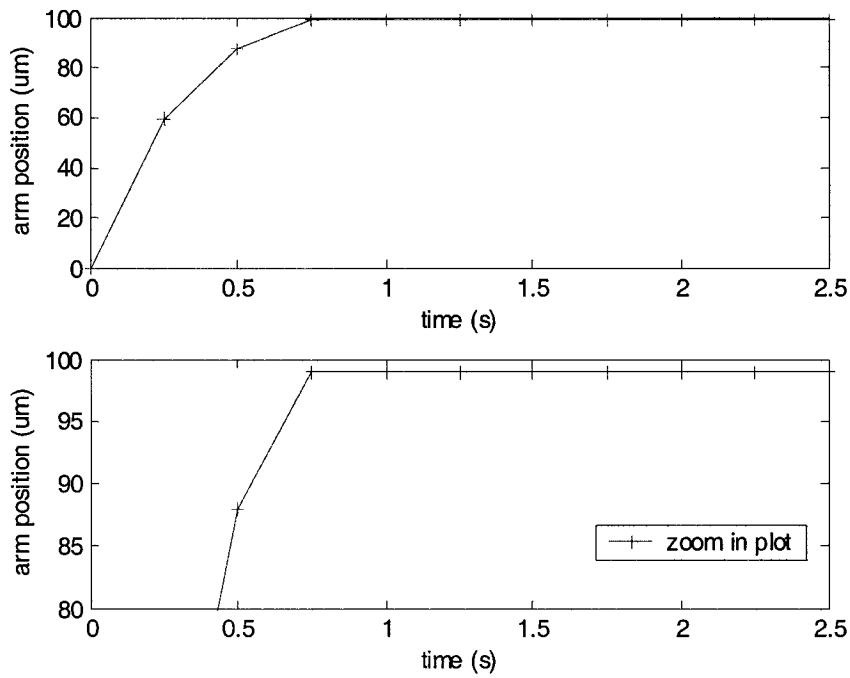

Figure 5-73 $h_2 = \pm 3.1278$Vs, f_l=0.005Nm, a steady state error of 1um(simulation)

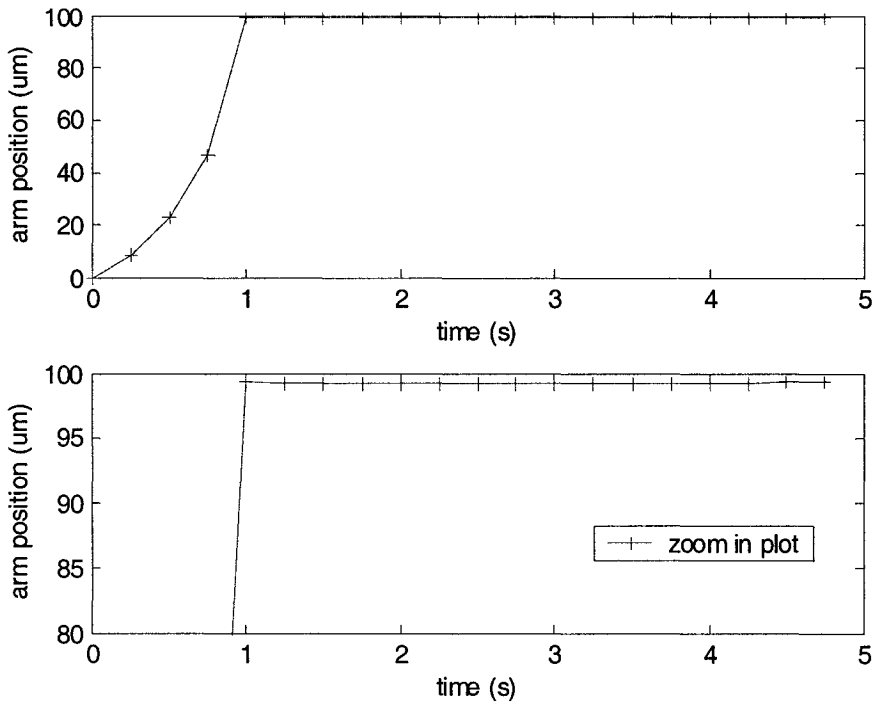

Figure 5-74 $h_2 = \pm 3.2$Vs, f_l =0.005Nm, a steady state error of 1um(experiment)

5.6 Robust adaptive impulse control

In the adaptive control presented in the previous section, h_2 is set to the value that just eliminates the dead zone. The controller is not robust to the friction variation. Is there any approach to make the controller more robust to the friction variation? This question can be solved with a large value of h_2.

5.6.1 Simulation and experimental response

When the load side friction is f_l =0.005Nm, h_2 =7.43Vs eliminates the dead zone.

Select a bigger h_2=10Vs to eliminate the dead zone completely even when h_1 is negative. The simulated response when h_2=10Vs is shown in Figure 5-75. It can be summarized by approximately two lines:

$$d = b_{simu1}(h_1/V_s + \eta_s) \qquad h_1/V_s \le -\eta_s \qquad (5\text{-}31)$$

$$d = b_{simu2}(h_1/V_s + \eta_s) \qquad h_1/V_s > -\eta_s \qquad (5\text{-}32)$$

where η_s=0.9. η_s does not vary much with friction level f_l^*.

The experimental response when h_2=10Vs is shown in Figure 5-76. It is can also be summarized by approximately two lines:

$$d = b_{expe1}(h_1/V_s + \eta_e) \qquad h_1/V_s \le -\eta_e \qquad (5\text{-}33)$$

$$d = b_{expe2}(h_1/V_s + \eta_e) \qquad h_1/V_s > -\eta_e \qquad (5\text{-}34)$$

where $\eta_e = 1.55$.

5.6.2 Simulation

When h_2=10Vs, f_l=0.0018, we use K_c=0.2, F=1.0e-6, and the simulation of the adaptive control result for x_d=100um is shown in Figure 5-77. The result of a friction increase to f_l=0.005Nm is shown in Figure 5-78. The control precision can reach 0.25um in both cases. The controller is robust to the friction variation.

5.6.3 Experiment

We use the same parameters used in simulation, and the result of the adaptive control

experiment for f_l=0.0018Nm, and x_d=100um are shown in Figure 5-79. In the experiment, since h_2 is big, the amplifier saturation condition must be checked for every pulse input. The experiment for f_l=0.005Nm, x_d=100um is shown in Figure 5-80. The results verify the simulation result. The settling time is less than 1s.

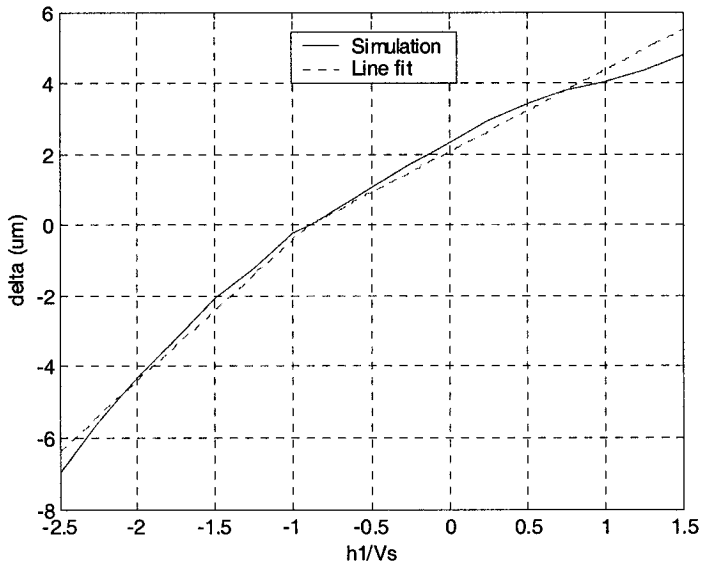

Figure 5-75 Simulation of arm increment to pulse for h_2=10Vs

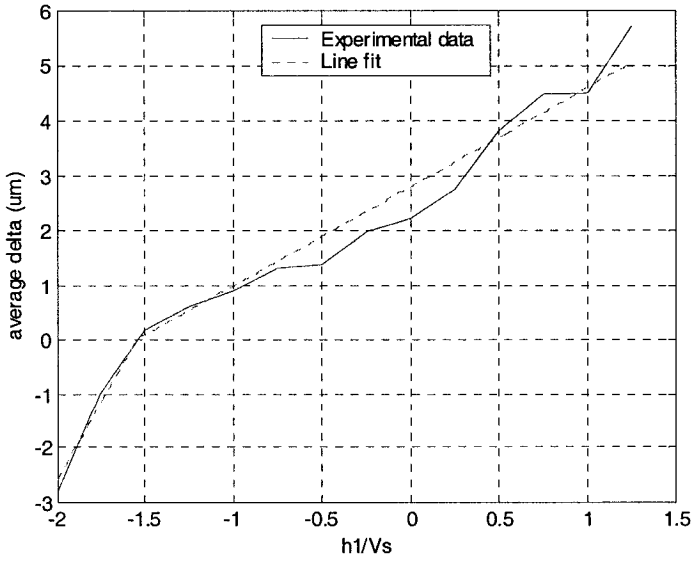

Figure 5-76 Experiment of arm increment to pulse for h_2=10Vs

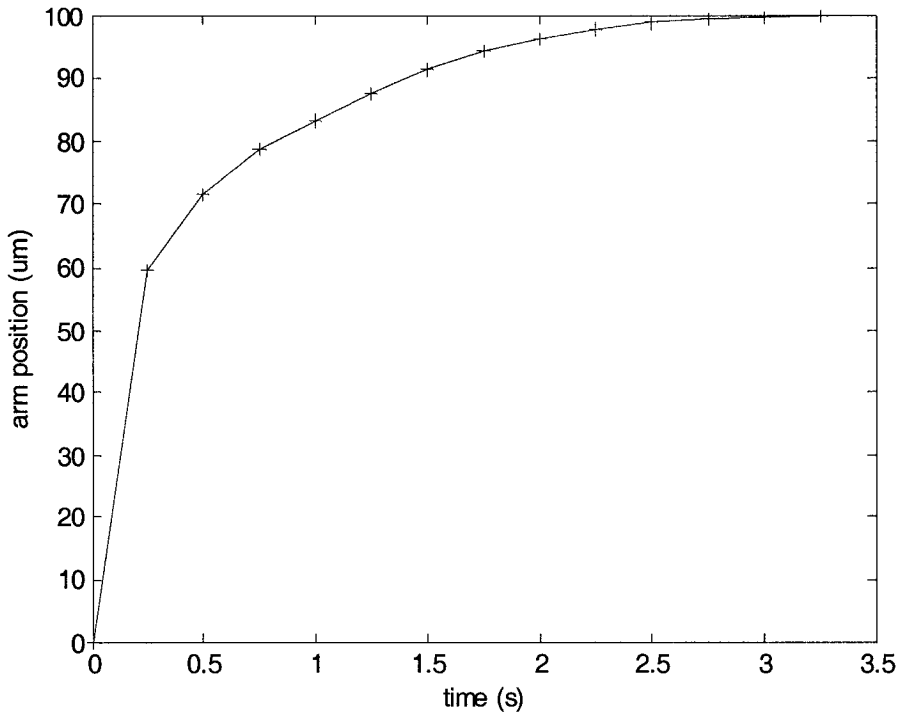

Figure 5-77 Simulation of adaptive impulse control f_l=0.0018Nm, x_d=100um

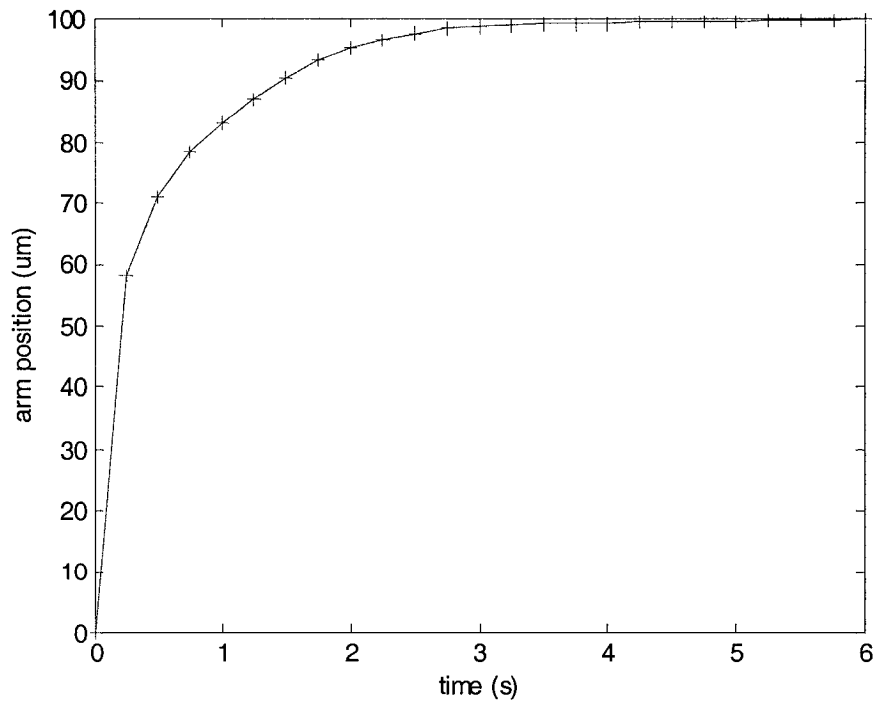

Figure 5-78 Simulation of adaptive impulse control f_l=0.005Nm, x_d=100um

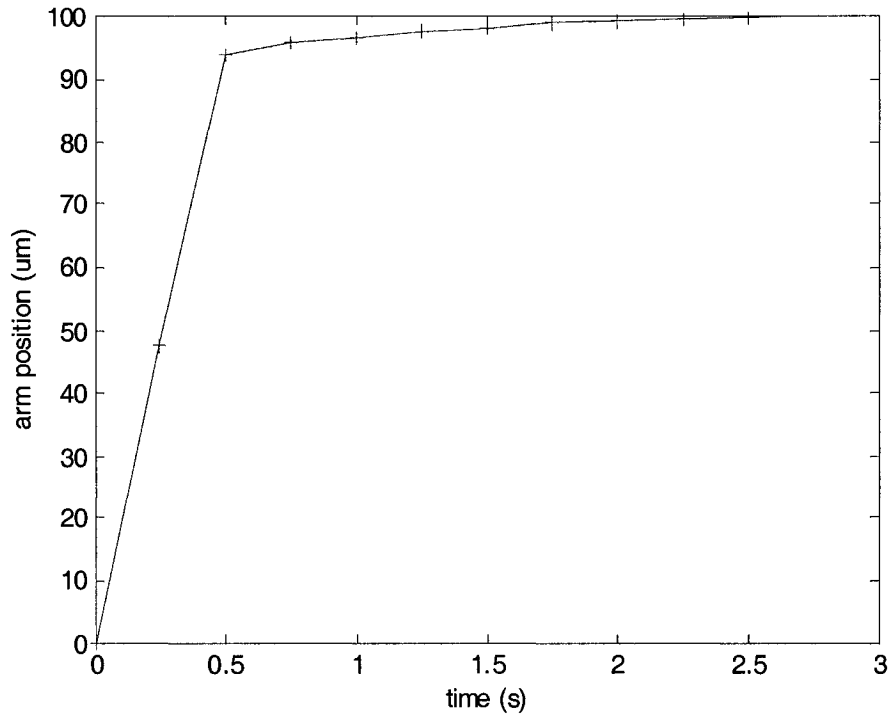

Figure 5-79 Experiment of adaptive impulse control f_l=0.0018Nm, x_d=100um

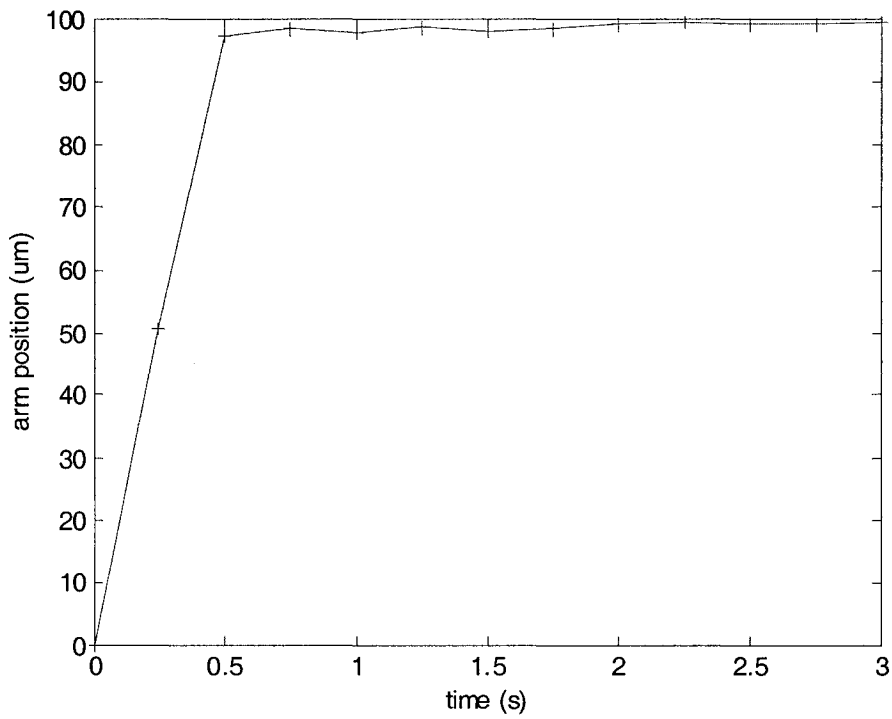

Figure 5-80 Experiment of adaptive impulse control f_l=0.005Nm, x_d=100um

5.6.4 Conclusion for impulse control

In impulse control, if the pulse rate is bigger than 250ms, the amount of time is too long time for the system to get stuck. If the pulse rate is less than 250ms, the system is still in motion and the pulse response is non-predictable. The optimal pulse rate is 250ms.

The pulse shape of the sum of the first and second harmonics can get good control effect in impulse control. The first harmonic supplies the main force to drive the system. The second harmonic can be used to eliminate the dead zone. The odd order harmonic pulses have similar effects as first harmonic pulses and the even order harmonic pulses have a similar effect to the second harmonic pulses. The higher order harmonic pulses are hard to keep the real pulse shape in experiment due to bandwidth limitations. So the optimal pulse shape is the sum of the first two harmonics.

The load side friction has a significant effect on impulse control. It can degrade the control resolution and enlarge the dead zone. The flexibility also has much effect on resolution and dead zone. It is important to decrease the friction and flexibility in the system.

By choosing a large amplitude h_2 for the second harmonic, we can make the impulse control system robust to the friction variation, as long as the system is not saturated.

Chapter 6 Conclusions and Future Work

6.1 Conclusions

A new approach for high-resolution control of harmonic drive motors using impulse control inputs is presented in this thesis. The main results and contributions are summarized as follows:

1) Dynamic model of harmonic drive motors

A dynamic model including the effects of friction and transmission flexibility is developed and identified experimentally. This model is shown to be capable of accurately predicting the impulse response of harmonic drive motors. Also demonstrated is the model's usefulness for the development of impulse control systems.

2) Effect of parameter variations on impulse response

The load side friction level has a significant effect on the resolution and dead zone in impulse control systems. The resolution gets worse and the dead zone increases proportionally as the load side friction level increases. It is therefore very important to account for load friction variations for impulse control to be effective.

3) Determination of optimal impulse waveform and pulse rate

The optimal impulse shape is the sum of the first two harmonics. This pulse shape

is relatively simple and it is shown that the second harmonic can be used to eliminate undesirable dead zone behaviour. Robustness of dead zone elimination to friction variation can be achieved by using a large second harmonic amplitude. Additionally, the pulse rate must be reduced to a sufficiently slow rate to achieve maximum resolution.

4) Adaptive impulse feedback control

It was determined that the impulse response curve varies depending on parameter variations such as load friction. To help compensate for this problem, a MRAC adaptive controller was successfully combined with the impulse control method. The reduction in dead zone behaviour using the second harmonic was shown to be highly effective in this approach.

5) Experimental testing and verification

A large amount of experimental testing and verification was performed in this thesis. Results show that the impulse feedback control and adaptive impulse control have a settling time of 1s, a steady state error of less than 0.3 um, and a resolution of 0.3 um. The resolution that could be obtained was ten times better than could be achieved using conventional linear control.

The results of this thesis represent the first known comprehensive study of applying impulse control to harmonic drive motors for high resolution positioning applications. This approach demonstrates that the resolution can be increased by more than an order of magnitude over conventional control methods. This will allow harmonic drives to be economically used in many new applications where high precision positioning capability is needed.

6.2 Future work

1. As an attempt to estimate system parameters more precisely, the use of tachometers to measure the motor and load side velocity is suggested, as well as adding the data to the online parameter estimator.

2. In impulse adaptive control, more parameters may be adapted to estimate the parameters precisely. This may reduce the system settling time.

3. Try to identify the effect of the combination of the friction and flexibility on the resolution and dead zone.

References

[1] Gordon, B.W., "Coordinated Control of Two Macro/Micro Manipulators for Fibre Pigtailing Automation", Master Thesis, Mechanical Engineering Department, Massachusetts Institute of Technology, 1995

[2] Gandhi, P.S., "Modelling and Control of Nonlinear Transmission Attributes in Harmonic Drive Systems", Ph.D. Thesis, Rice University, Houston, Texas, 2001

[3] Taghirad, H.D., "Robust Torque Control of Harmonic Drive Systems", Ph.D. Thesis, Department of Electrical Engineering, McGill University, Montreal, 1997

[4] Stefani, R.T., Shahian, B., Savant, C.J., Hostetter, G.H., "Design of Feedback Control Systems", Oxford University Press, 2002

[5] Slotine, J.E., & Li, W., " Applied Nonlinear Control", Prentice Hall, New Jersey, 1991

[6] Thomson, W.T., "Theory of Vibration with Applications", Fourth Edition Prentice Hall, New Jersey, 1993

[7] Slocum, A.H., "Precision Machine Design" Prentice Hall, New Jersey, 1992

[8] Taghirad, H.D., Belanger, P.R., "Modelling and Parameter Identification of Harmonic Drive Systems" J. of Dynamic Systems, Measurement, and Control, Dec.1998, Vol. 120,PP439-444

[9] Taghirad, H.D., Belanger, P.R., " H_∞ Robust Control of Harmonic Drive Systems" J. of Dynamic Systems, Measurement, and Control, Sept. 2001, Vol. 123, PP338-345

[10] Gandhi, P.S., Ghorbel, F.H., Dabney, J., " Modelling, Identification, and Compensation of Friction in Harmonic Drives", Proc. Of 41st IEEE Conf. On Decision

and Control. Dec. 2002, Las Vegas, PP160-166

[11] Ghorbel, F.H., Gandhi, P.S., Alpeter, F., " On the Kinamatic Error in Harmonic Drive Gears", J. of Mechanical Design, Mar. 2001, Vol. 123 PP90-97

[12] Gandhi, P.S., Ghorbel, F.H., " Closed-Loop Compensation of Kinamatic Error in Harmonic Drives for Precision Control Applications" IEEE Transaction on Control Systems technology, Vol. 10, No.6 Nov.2002, PP759-768

[13] Tuttle, T.D., Seering, W.P., " A Nonlinear Model of a Harmonic Drive Gear Transmission" IEEE Transaction on Robotics and Automation Vol.12, No. 3 June 1996, PP 368-374

[14] Seyfferth, W., Maghzal, J., Angeles, J., "Nonlinear Modelling and Parameter Identification of Harmonic Drive Robotic Transmissions" IEEE international Conf. On Robotics and Automation, 1995, PP3027-3032

[15] Moghaddam, M.M., Goldenberg, A.A., "Nonlinear Modelling and Robust H_∞ Based Control of Flexible Joint Robots with Harmonic Drives", Proc. IEEE Conf. Robotics and Automation. April 1997, pp 3130-3135

[16] Kazerooni, H., "Dynamics and Control of Instrumented Harmonic Drives" J. of Dynamic Systems, Measurement, and Control, Mar. 1995, Vol. 117, PP 15-19

[17] Kircanski, N.M., Goldenberg, A.A., "An Experimental Study of Nonlinear Stiffness, Hysteresis, and Friction Effects in Robot Joints with Harmonic drives and Torque Sensors", The international Journal of Robotic Research, Vol.16, No. 2,April 1997, pp. 214-239

[18] Popovic, M.R., Gorinevsky, D.M., Goldenberg, A.A., "High-Precision Positioning of a Mechanism with Nonlinear Friction Using a Fuzzy Logic Pulse Controller", IEEE

Trans. On Control System Technology, Vol. 8,No. 1, Jan. 2000, pp151-158

[19] Haessig, D.A., Friedland, B., "On the Modelling and Simulation of Friction" J. of Dynamic Systems, Measurement, and Control, Sept. 1991, Vol. 113, PP354-362

[20] Armstrong-Helouvry, B., Dupont, P., Carlos Canudas de Wit, "A Survey of Models, Analysis Tools and Compensation Methods for the Control of Machines with Friction" Automatica, July 1994, PP 1083-1138

[21] Carlos Canudas de wit, Olsson, H., Astrom, K.J., Lischinsky, P., "A New Model for Control of Systems with Friction", IEEE Transaction Automatic Control Vol. 40, No. 3, Mar. 1995 PP 419-425

[22] Swevers, J., Al-Bender, F., Gansemen, C.G., and Prajogo, T., "An Integrated Friction Model Structure with Improved Presliding Behaviour for Accurate Friction Compensation" IEEE Transaction Automatic Control Vol. 45, No. 4, Apr. 2000 PP 675-686

[23] Altpeter, F., Ghorbel, F.H., Longchamp, R., " Relationship Between Two Friction Models: A Singular Perturbation Approach", Proc. IEEE 37th Conf. Decision and Control, Dec. 1998, PP 1572-1574

[24] Kelly, R., Llamas, J., " Determination of Viscous and Coulomb Friction by Using Velocity Response to Torque Ramp Inputs", Proc. IEEE International Conf. Robotics and Automation May 1999, PP 1740-1745

[25] Tariku, F.A., Rogers, R.J., "Improved Dynamic Friction Models for Simulation of One-Dimensional and Two-Dimensional Stick-Slip Motion", Journal of Tribology Oct. 2001, Vol. 123 pp 661-669

[26] Wu, R.H., Tung, P.C., " Studies of Stick-Slip Friction, Presliding Displacement, and

Hunting. J. of Dynamic Systems, Measurement, and Control, Mar. 2002, Vol. 124, PP 111-117

[27] Carlos Canudas de Wit, and Lischinsky, P., " Adaptive Friction Compensation with Partially Known Dynamic Friction Model", International Journal of Adaptive Control and Signal Processing, Vol. 11, 1997, PP 65-80

[28] Dankowicz, H., " On the Modelling of Dynamic Friction Phenomena", ZAMM Z. Angew. Math. Mech. 79 (1999) 6, pp 399-409

[29] Huang, S.J., Yen, J.Y., and Lu, S., " Dual Mode Control of a System with Friction", IEEE Transaction On Control System Technology, Vol.7, No.3, 1999 PP 306-314

[30] Popovic, M.R., and Goldenberg, A.A., " Modelling of Friction Using Spectral Analysis", IEEE Transaction on Robotics and Automation, Vol.14, No.1, Feb.1998, PP 114-122

[31] Tan, K.K., Lee, T.H., Huang, S.N., and Jiang, X., "Friction Modelling and Adaptive Compensation Using a Relay Feedback Approach" IEEE Transaction on Industrial Electronics, Vol. 48 No. 1, Feb. 2001, PP 169-176

[32] Yang, S., and Tomizuka, M., "Adaptive Pulse Width Control for Precise Positioning under the Influence of Stiction and Coulomb Friction" J. of Dynamic Systems, Measurement, and Control, Sept. 1988, Vol. 110, PP 221-2227

[33] Orlov, Y.V., " Nonlinear Control Systems with Impulse Inputs" Proc. Conf. Decision and Control, Dec. 1997,PP 630-634

[34] Huang, W.H., and Mason, M.T., "Experiments in Impulsive Manipulation" Proc. IEEE International Conf. Robotics and Automation, May 1998, PP 1077-1082

[35] Awabdy, B.A., Shih, W.C., and Auslander, D.M., "Nanometer Positioning of a Linear

Motion Stage under Static Loads" IEEE/ ASME Transaction on Mechatronics Vol.3, No. 2 June 1998, PP 113-119

[36] Jeon, H.S., and Oh, S.H., " A Study on Stress and Vibration Analysis of a Steel and Hybrid Flexspline for Harmonic Drive" Composite Structure 47 (1999) PP 823-833

[37] Zhang, G., Furusho, J., and Sakaguchi, M., " Vibration Suppression Control of Robot Arms Using a Homogeneous-Type Electrorheological Fluid" IEEE/ASME Transaction on Mechatronics Vol. 5, No. 3, Sept. 2000, pp 302-309

[38] Singhose, W., Mills, B., and Seering, W., " Vibration Reduction with Specified-Swing Input Shapers" Proc. IEEE Conf. Control Application, Aug. 1999, PP 533-538

[39] Kapila, V., Tzes, A., and Yan, Q., "Closed-Loop Input Shaping for Flexible Structures Using Time-Delay Control" J. of Dynamic Systems, Measurement, and Control, Sept. 2000, Vol. 122, PP 454-460

Appendix A: Construction and Operation of Harmonic Drives

A typical harmonic drive is composed of the components identified in Figure A-1. The wave generator (A) is an elliptical cam enclosed in an antifriction ball bearing assembly. It normally functions as the rotating input element. When inserted into the bore of the flexspline, it imparts its elliptical shape to the flexspline, causing the external teeth of the flexspline to engage with the internal teeth of the circular spline at two equally spaced areas 180 degrees apart on their respective circumferences, thus forming a positive gear mesh at these points of engagement. The externally toothed flexspline(B) is a non-rigid or flexible, thin-walled, cylindrical cup which is smaller in circumference and has two less teeth than the circular spline. It is normally the rotating output element but can be utilized as the fixed, non-rotating member when output is through the circular spline. The circular spline(C) is a thick-walled, rigid ring with internal teeth. It normally functions as the fixed or non-rotating member but can, in certain applications, be utilized as a rotating output element as well.

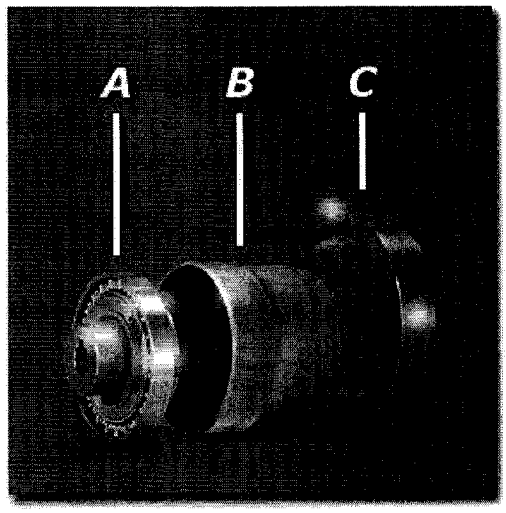

(a)

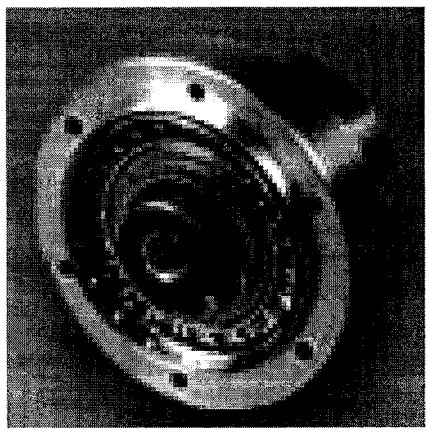

(b)

Figure A-1 (a) Harmonic drive gear components (b) Assembly

A fully assembled harmonic drive is shown in Figure A-1(b). In the most common speed reduction configuration, the wave generator is the input port, the flexspline is the output port, and the circular spline is immobile.

Figure A-2 illustrates the operation of the harmonic drive in the most common configuration. The teeth on the non-rigid flexspline and the rigid circular spline are in

continuous engagement. Since the flexspline has two teeth less than the circular spline, one revolution of the input causes relative motion between the flexspline and the circular spline equal to two teeth. With the circular spline rotationally fixed, the flexspline rotates in the opposite direction to the input.

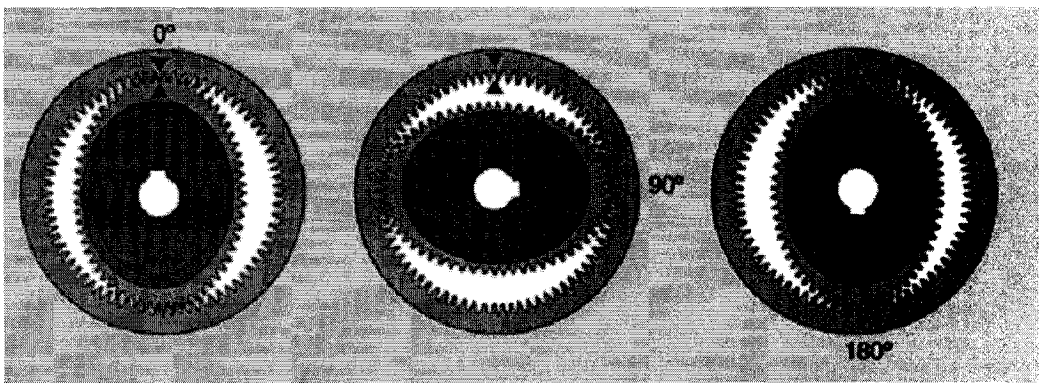

Figure A-2 Principle of operation of a harmonic drive

In general, the gear ratio formula for a harmonic drive gearing is

$$r = \frac{FS}{(CS - FS)}$$

with the tooth differential between the circular spline (CS) and the flexspline (FS) accounting for the gear ratio (r) achieved. For example, to satisfy the formula, an 80:1 ratio would have 160 teeth on the flexspline and 162 teeth on the circular spline. The two-tooth difference permits a two-tooth advance for every revolution of the elliptical generator, or one flexspline advance for every 80 revolutions of the wave generator in this particular example.

Appendix B: Advantages of Harmonic Drives

Because it consists of only three simple parts, harmonic drive gearing offers design engineers the freedom to integrate drive components directly into machines or equipment. Harmonic drive is a pure torque couple with all concentric elements and requires less bulky support structures than conventional gearing.

Harmonic drive gearing is in a class of its own when it comes to motion control and mechanical power transmission. With operating principles and construction that maximize output torque and minimize size and weight, harmonic drive gearing offers advantages such as high reduction ratios, zero backlash, and high precision that cannot be equalled by conventional gear trains. The typical advantages of harmonic drive are as follow:

Excellent positional accuracy and repeatability - Positional accuracy may be minimized within one arc minute and repeatability within a few seconds.

High torque capacity - Since power is transmitted through multiple tooth engagement, harmonic drive gearing offers high output torque capacity.

Single-stage high reduction ratio - With only three elements, the single-stage reduction ratios range from 50:1 to 320:1 with the same weight and mechanical dimensions.

Zero backlash - Cup-type harmonic drive gearing operates with zero backlash between mating teeth because of natural gear preload and radial tooth movement. The only shaft-to-shaft backlash that exists, originates in the input coupling and ranges from 2-36 arc-sec depending on unit size and reduction ratio. This coupling can be

eliminated if necessary, resulting in zero backlash for the entire drive.

In - line configuration - Harmonic drive gearing input and output shafts are concentric, allowing machine designers to dramatically reduce the required packaging space compared to other high ratio, high torque drives.

High torsional stiffness – The torsional stiffness of harmonic drive gearing allows greater precision and higher servo gains.

Efficiencies - Operating efficiencies of up to 90% can be obtained. Ratings are based on actual shaft-to-shaft tests.

Back driving - Harmonic drive units are reversible and can be back driven. If necessary, loads can be held in place by braking the wave generator when the servo system is not powered.

Because of these properties, harmonic drives are popular in many industrial and space applications.

Appendix C: Online Parameter Estimation

As an attempt to figure out the parameter's uncertainty in the system, online parameter estimation is studied here. The model of (2-8) and (2-9):

$$J_m\ddot{q}_m = F_m - \frac{K_m K_b}{R}\dot{q}_m - rK_s(rq_m - q_l) + \frac{K_m}{R}u(t) \tag{C-1}$$

$$J_l\ddot{q}_l = F_l + K_s(rq_m - q_l) \tag{C-2}$$

When $|\dot{q}_m|>0$, and $|\dot{q}_l|>0$, the friction can be written as:

$$F_m = -\mathrm{sgn}(\dot{q}_m)f_{cm} - b_m\dot{q}_m \tag{C-3}$$

$$F_l = -\mathrm{sgn}(\dot{q}_l)f_{cl} - b_l\dot{q}_l \tag{C-4}$$

Substitute (C-3), (C-4) into (C-1) and (C-2) yields:

$$\ddot{q}_m = -\frac{f_{cm}}{J_m}\mathrm{sgn}(\dot{q}_m) - (\frac{b_m}{J_m} + \frac{K_m K_b}{RJ_m})\dot{q}_m - \frac{rK_s}{J_m}(rq_m - q_l) + \frac{K_m}{RJ_m}u(t) \tag{C-5}$$

$$\ddot{q}_l = -\frac{f_{cl}}{J_l}\mathrm{sgn}(\dot{q}_l) - \frac{b_m}{J_m}\dot{q}_l + \frac{K_s}{J_l}(rq_m - q_l) \tag{C-6}$$

Case 1: $\ddot{q}_m$ and $\ddot{q}_l$ can be measured.

Let

$$g_1 = -\frac{f_{cm}}{J_m}$$

$$g_2 = -(\frac{b_m}{J_m} + \frac{K_m K_b}{RJ_m})$$

$$g_3 = -\frac{rK_s}{J_m}$$

$$g_4 = \frac{K_m}{RJ_m}$$

$$g_5 = -\frac{f_{cl}}{J_l}$$

$$g_6 = -\frac{b_l}{J_l}$$

$$g_7 = \frac{K_s}{J_l}$$

then

$$y = \begin{bmatrix} \ddot{q}_m \\ \ddot{q}_l \end{bmatrix} = [W] \begin{bmatrix} g_1 \\ g_2 \\ g_3 \\ g_4 \\ g_5 \\ g_6 \\ g_7 \end{bmatrix} \tag{C-7}$$

where

$$[W] = \begin{bmatrix} \text{sgn}(\dot{q}_m) & \dot{q}_m & (rq_m - q_l) & u & 0 & 0 & 0 \\ 0 & 0 & 0 & 0 & \text{sgn}(\dot{q}_l) & \dot{q}_l & (rq_m - q_l) \end{bmatrix}$$

Case 2: When $\ddot{q}_m$ and $\ddot{q}_l$ can not be measured.

Convolving both sides of (C-5) and (C-6) with $e^{-\lambda t}$ yields [5]

$$\dot{q}_m - \lambda \int_0^t e^{-\lambda(t-p)} \dot{q}_m(p)dp = -\frac{f_{cm}}{J_m} \int_0^t e^{-\lambda(t-p)} \text{sgn}(\dot{q}_m)dp - (\frac{b_m}{J_m} + \frac{K_m K_b}{RJ_m}) \int_0^t e^{-\lambda(t-p)} \dot{q}_m(p)dp +$$
$$\frac{K_m}{RJ_m} \int_0^t e^{-\lambda(t-p)} u(p)dp - \frac{rK_s}{J_m} (\int_0^t e^{-\lambda(t-p)} (rq_m(p) - q_l(p))dp)$$

(C-8)

$$\dot{q}_l - \lambda \int_0^t e^{-\lambda(t-p)} \dot{q}_l(p)dp = -\frac{f_{cl}}{J_l} \int_0^t e^{-\lambda(t-p)} \operatorname{sgn}(\dot{q}_l)dp - \frac{b_l}{J_l} \int_0^t e^{-\lambda(t-p)} \dot{q}_l(p)dp +$$

$$+ \frac{K_s}{J_l} \left(\int_0^t e^{-\lambda(t-p)} (rq_m(p) - q_l(p))dp \right)$$

(C-9)

They can be written as

$$\dot{q}_m = (\lambda - \frac{b_m}{J_m} - \frac{K_m K_b}{RJ_m}) \int_0^t e^{-\lambda(t-p)} \dot{q}_m(p)dp - \frac{f_{cm}}{j_m} \int_0^t e^{-\lambda(t-p)} \operatorname{sgn}(\dot{q}_m)dp$$

$$+ \frac{K_m}{RJ_m} \int_0^t e^{-\lambda(t-p)} u(p)dp - \frac{r}{J_m} K_s \left(\int_0^t e^{-\lambda(t-p)} (rq_m(p) - q_l(p))dp \right)$$

(C-10)

$$\dot{q}_l = (\lambda - \frac{b_l}{J_l}) \int_0^t e^{-\lambda(t-p)} \dot{q}_l(p)dp - \frac{f_{cl}}{J_l} \int_0^t e^{-\lambda(t-p)} \operatorname{sgn}(\dot{q}_l)dp + \frac{K_s}{J_l} \left(\int_0^t e^{-\lambda(t-p)} (rq_m(p) - q_l(p))dp \right)$$

(C-11)

let

$$g_1 = \lambda - \frac{b_m}{J_m} - \frac{K_m K_b}{RJ_m}$$

$$g_2 = -\frac{f_{cm}}{J_m}$$

$$g_3 = \frac{K_m}{RJ_m}$$

$$g_4 = -\frac{rK_s}{J_m}$$

$$g_5 = \lambda - \frac{b_l}{J_l}$$

$$g_6 = -\frac{f_{cl}}{J_l}$$

$$g_7 = \frac{K_s}{J_l}$$

$$w_1 = \int_0^t e^{-\lambda(t-p)} \dot{q}_m(p) dp$$

$$w_2 = \int_0^t e^{-\lambda(t-p)} \operatorname{sgn}(\dot{q}_m) dp$$

$$w_3 = \int_0^t e^{-\lambda(t-p)} u(p) dp$$

$$w_4 = \int_0^t e^{-\lambda(t-p)} (r q_m(p) - q_l(p)) dp$$

$$w_5 = \int_0^t e^{-\lambda(t-p)} \dot{q}_l(p) dp$$

$$w_6 = \int_0^t e^{-\lambda(t-p)} \operatorname{sgn}(\dot{q}_l) dp$$

then (C-10) and (C-11) can be written as

$$y = \begin{bmatrix} \dot{q}_m \\ \dot{q}_l \end{bmatrix} = [W] \begin{bmatrix} g_1 \\ g_2 \\ g_3 \\ g_4 \\ g_5 \\ g_6 \\ g_7 \end{bmatrix} \qquad \text{(C-12)}$$

where

$$[W] = \begin{bmatrix} w_1 & w_2 & w_3 & w_4 & 0 & 0 & 0 \\ 0 & 0 & 0 & 0 & w_5 & w_6 & w_4 \end{bmatrix}$$

Implement a parameter estimator using equation (C-12). Take measured data (t, u(t), q_m, q_l) from experiment. $\dot{q}_m$ and $\dot{q}_l$ can be calculated from q_m and q_l in different sampling time:

$$\dot{q}_m(k) = \frac{q_m(k+1) - q_m(k-1)}{2T} \qquad \text{(C-13)}$$

$$\dot{q}_l(k) = \frac{q_l(k+1) - q_l(k-1)}{2T} \qquad \text{(C-14)}$$

T is the sampling time. Because there are seven parameters to be estimated, use a sum of more than 8 sine waves with different frequency as a reference input. Put [$\dot{q}_m$ $\dot{q}_l$ q_m q_l u(t)] into a data file as the input of the estimator.

As the result, the estimated parameters do not converge. The reasons probably are:

1. The encoder resolution is not high enough. That makes the calculated velocity ($\dot{q}_m$ and $\dot{q}_l$) not consistent with the real velocity.
2. The parameter variations and uncertainties in the system make the estimator difficult to track the real parameters
3. There are some un-modelled attributes in the system

If tachometers are available in the future, the measured velocities can be used to estimate the parameters.